Technische Universität München

Fakultät für Chemie

# Cu-Oxo Cluster in Zeolites for the Selective Oxidation of Methane to Methanol

Insu Lee

Vollständiger Abdruck der von der Fakultät für Chemie der Technischen Universität München zur Erlangung des akademischen Grades eines

**Doktors der Naturwissenschaften (Dr. rer. nat.)**

genehmigten Dissertation.

| | |
|---|---|
| Vorsitzender: | Prof. Dr.-Ing. Kai-Olaf M. Hinrichsen |
| Prüfer der Dissertation: | 1. Prof. Dr. Johannes A. Lercher |
| | 2. Prof. Dr. Klaus Köhler |

Diese Dissertation wurde am 24.02.2022 bei der Technischen Universität München eingereicht und durch die Fakultät für Chemie am 12.05.2022 angenommen

*“There’s always a new challenge to keep you motivated”*

Sean Connery

# Acknowledgments

I would like to thank Prof. Dr. Johannes A. Lercher for giving me the opportunity to pursue my PhD thesis in his chair. Furthermore, you gave me the opportunity to go to PNNL, where I had the chance to expand my knowledge. I have learned to do rigorous science and to be critical of misleading scientific hypotheses. I appreciate the open discussions, where we always had something to learn and the chance improve our scientific work. You were always available and had an open ear for us. Thank you again for letting me be part of the TCII group.

I also thank Maricruz Sanchez-Sanchez for the immense help, guidance, inspiration, and scientific discussions throughout my PhD period. You have been always open to discussions and I highly appreciate your scientific input and kind advice. I hope you have a successful start at your new position in Vienna.

Special gratitude goes to Prof. Dr. Andreas Jentys, who offered his support on various occasions. Your experience and deep understanding of spectroscopy helped me a lot. Especially XAS and IR discussions with you were always interesting and fruitful. Beamline trips without you, would not have been entertaining and enjoyable.

I thank our collaborators, who worked with us on Cu-zeolites: Dr. Jian Zheng, Prof. Dr. Evgeny Pidko, Dr. Roger Rousseau, Dr. Mal-Soon Lee, Dr. Oliver Gutierrez, Dr. John Fulton, and Dr. Niri Govind. I especially thank again John and Niri for their guidance and scientific discussions. I am grateful that I was able to learn XAS and TDDFT from you. Without you, I would not have been able to complete my thesis. I truly enjoyed our sessions and I wished we could have continued working together on XFEL.

I am grateful to our administrative staff: Bettina Federmann (You are a very kind and important person to TCII), Stefanie Seibold, Ulrike Sanwald, Kateryna Kryvko for their support during my PhD period. I wish you all the best for the future. Working without our technical staff Franz-Xaver Hecht, Andreas Marx, Martin Neukamm, and Iqbal Muhammad would have been impossible. Thank you for your constant help and technical support in the lab.

Special thank goes to my friends and colleagues of the methane oxidation team Takaaki Ikuno, Lei Tao, and Matteo Ranieri. I learned a lot from you and appreciate the time we spent together. We had a lot of fun in the lab, beamline trips, and outside the lab. I would also like to thank former bachelor and master students who worked

with me. Especially Florian Zahn, Corbinian Grön, Alexander Engel, and Matias Wegner Tornel performed very well and helped me to push my scientific limits.

The former supervisor of my master thesis, Marco Peroni, deserves acknowledgment for introducing me to the world of catalysis. I appreciate the time with you, and I am happy that you gave me the opportunity to work with you.

Manish Shetty, Udishnu Sanyal, Katherine Koh, and Laura Meyer: Thanks for hanging out and taking me around in PNNL. Thank you for taking care and forcing me to go to the hospital.

My life in the lab and in munich has been nice and pleasant. I enjoyed the time I spent together with my colleagues and friends from TCII: Martina Aigner, Martin Baumgärtl, Madita Einemann, Phillipp Fischer, Fuli Deng, Rachit Khare, Simon Krebs, Laura Löbbert, Lingli Ni, Xi Chen, Jakub Pazdera, Guanhua Cheng, Yong Wang, Teresa Schatl, Daniel Melzer, Felix Kirchberger, Andreas Ehrmaier, Manuel Wagenhofer, Lara Milakovic, Yong Wang, Mirjam Wenig, Ruixue Zhao, Iris Yu. I especially enjoyed the activities, creative sessions and coffee breaks with Niklas Pfriem, Lennart Wahl Ferdinand Vogelgsang, Roland Weindl, Christian Weindl, Christoph Gross, Verena Höpfl, Iqbal Muhammad, Florian Zahn and Alexander Wellmann.

Life would have been boring without my friends: Robert, Plo, Kevin, Roman, Tobi, Gicht, Keks, Fipsi, Robi, Manu, Micky, Gerdi, Franzi, Julian, and Ruben. Thank you for distracting me from work. Also, to my crew from bachelor and master time: Marc, Bruno, Dave, Michi, Ryan, Inno, Jacob, and Jarek. It was a nice and funny time.

My mother, father, and family have been important figures throughout my whole life. Without you, I would not have been able to focus on my studies. Your support and cheering motivated me to pursue and continue with my work and studies. I am happy that I met my partner My (name), who always cheered me up, endured all my moods, and gave me unconditional support and love. Only words cannot express my gratitude to you all. Thank you for supporting me.

Insu Lee

Fenruary.2022

# Abbreviations

| | |
|---|---|
| AIMD | Ab Initio molecular dynamics |
| BAS | Brønsted acid site |
| CHA | Chabazite |
| $Cu_{eff}$ | Cu-efficiency |
| DFT | Density functional theory |
| DME | Dimethylether |
| DOE | Department of Energy |
| EFAl | Extra framework aluminum |
| EXAFS | Extended X-ray absorption fine structure |
| FCC | Fluid catalytic cracking |
| FER | Ferrierite |
| FT | Fourier-transformed |
| GGA | Generalized gradient approximation |
| GTH | Goedecker-Teter-Hutter |
| HERFD | High energy resolution fluorescence detected |
| IR | Infrared |
| LAS | Lewis acid site |
| LCF | Linear combination fitting |
| LMCT | Ligand to metal charge transfer |
| MCR | Multivariate curve resolution |
| MD | Molecular dynamics |
| MMO | Methane monooxygenase |
| MOR | Mordenite |
| MR | Membered ring |
| MTG | Methanol to gasoline |
| MTO | Methanol to olefins |
| NADH | Nicotinamide adenine dinucleotide + hydrogen |
| NERSC | National Energy Research Scientific Computing Center |
| NMR | Nuclear magnetic resonance |
| PBE | Perdew, Burke and Ernzerhoff |
| pMMO | Particulate methane monooxygenase |

| | |
|---|---|
| PNNL | Pacific Northwest National Laboratory |
| RIXS | Resonant inelastic X-ray scattering |
| sMMo | Soluble methane monooxygenase |
| SCR | Selective catalytic reduction |
| TDDFT | Time-dependent density functional theory |
| UV-Vis | Ultraviolet-visible |
| XAFS | X-ray absorption fine structure |
| XANES | X-ray near edge structure |
| XAS | X-ray absorption spectroscopy |
| XES | X-ray emission spectroscopy |
| XFEL | X-ray free electron laser |

## Abstract

Cu-oxo cluster stabilized in the constrained environment of zeolites are active for the selective oxidation of methane to methanol. Next to framework associated Al species in zeolites which are crucial for the efficient formation of homotopic Cu-oxo cluster, extraframework Al significantly enhances the activity towards methanol. The structure of Cu-Al-oxo nanocluster is determined by X-ray absorption spectroscopy.

## Zusammenfassung

Cu-oxo Cluster stabilisiert in der eingeschränkten Umgebung von Zeolithen, sind aktiv für die selektive Oxidation von Methan zu Methanol. Neben den Gerüst-assoziierten Al Spezies in Zeolithen, die für die effiziente Bildung homotoper Cu-oxo Cluster entscheidend sind, erhöht außerhalb des Gitters vorhandenes Al die Aktivität zur Umsetzung von Methan. Die Struktur der Cu-Al-oxo Nanocluster wird durch Röntgenabsorptionsspektroskopie bestimmt.

# Table of Contents


**1 General Introduction ..... 1**
1.1 Limitations of Methane Utilization ..... 1
1.2 Conventional Conversion of Methane ..... 2
1.3 Selective Oxidation of Methane to Methanol ..... 4
1.4 Zeolites ..... 8
1.5 Cu-Oxo Cluster in Zeolites ..... 11
1.5.1 Nuclearity of Cu-Clusters Hosted in Zeolites ..... 11
1.5.2 Methane Activation over Cu-Oxo Cluster ..... 13
1.6 X-Ray Absorption Spectroscopy ..... 15
1.6.1 Fundamentals of X-Ray Absorption Spectroscopy ..... 15
1.6.2 X-Ray Absorption Near Edge Structure ..... 18
1.6.3 Extended X-Ray Absorption Fine Structure ..... 22
1.7 Scope of this Thesis ..... 27
1.8 References ..... 28
**2 Critical Assessment of Oxidation States of Cu present in MOR ..... 40**
2.1 Abstract ..... 40
2.2 Introduction ..... 41
2.3 Experimental Methods ..... 42
2.3.1 Preparation of Cu-MOR Samples ..... 42
2.3.2 Testing of Activity for Selective Oxidation of Methane ..... 42
2.3.3 Cu K-edge HERFD XANES ..... 43
2.3.4 Conventional Cu K-edge XANES ..... 43
2.3.5 In Situ FT-IR Spectroscopy ..... 44
2.4 Results and Discussion ..... 45
2.4.1 Activity of Cu-MOR ..... 45
2.4.2 FT-IR of CO and NO Adsorption at Liquid Nitrogen Temperature ..... 46
2.4.3 Formation and Stability of Cu-Oxo Cluster Under X-Ray Exposure ..... 50
2.4.4 Reduction Behavior of $Cu^{2+}$-Species in MOR ..... 53
2.4.5 Enhancing the Spectroscopic Fingerprints by HERFD-XANES ..... 57
2.4.6 Activity of He-treated Cu-MOR ..... 59
2.5 Conclusion ..... 61
2.6 Acknowledgement ..... 62
2.7 Appendix ..... 63
2.8 References ..... 66

**3 Activity of Cu-Al-Oxo Extra-Framework Clusters for Selective Methane Oxidation on Cu-exchanged zeolites ..... 73**
3.1 Abstract ..... 73
3.2 Introduction ..... 74
3.3 Experimental Methods ..... 76
3.3.1 Preparation of Cu-MOR Samples ..... 76
3.3.2 Testing of Activity for Selective Oxidation of Methane ..... 76
3.3.3 In Situ IR Spectroscopy ..... 77
3.3.4 $^{27}$Al NMR Spectroscopy ..... 77
3.3.5 Al K-edge and Cu L-edge XAFS ..... 77
3.3.6 Cu K-edge HERFD-XANES ..... 78
3.3.7 Conventional Cu K-edge XANES ..... 79
3.3.8 Computational Models ..... 79
3.3.9 DFT Calculations ..... 80
3.3.10 AIMD Simulations ..... 80
3.3.11 EXAFS Simulations ..... 80
3.3.12 XANES Calculations with Time-Dependent DFT ..... 81
3.4 Results and Discussions ..... 82
3.4.1 Activity of Cu-MOR Catalysts Prepared Under Controlled Conditions ... 82
3.4.2 Characterization of Parent MOR-A and MOR-B samples ..... 83
3.4.3 Location of exchanged Cu Species in Standard and Highly active MOR 85
3.4.4 X-ray Absorption spectroscopic study of highly active Cu-MOR species 87
3.4.5 Structural Assignment of Cu Species using AIMD and Simulated K- and $L_3$-edge XANES and EXAFS spectra ..... 89
3.5 Conclusion ..... 92
3.6 Acknowledgement ..... 93
3.7 Appendix ..... 94
3.8 References ..... 112
**4 Role of Zeolite Topology for the Formation of Cu-Oxo Species for the Selective Oxidation of Methane to Methanol ..... 119**
4.1 Abstract ..... 119
4.2 Introduction ..... 120
4.3 Experimental Methods ..... 121
4.3.1 Preparation of Cu-zeolite samples ..... 121
4.3.2 Testing of Activity for Selective Oxidation of Methane ..... 121
4.3.3 In Situ Ultraviolet-Visible Spectroscopy on Cu-zeolites ..... 122
4.3.4 In Situ IR-Spectroscopy ..... 122
4.4 Results and Discussion ..... 123
4.4.1 Influence of Zeolite Framework on the Activity ..... 123

4.4.2 Investigation of Cu-siting in FER ..... 125
4.4.3 High Pressure Reaction on Cu-CHA ..... 126
4.5 Conclusions ..... 129
4.6 Acknowledgement ..... 130
4.7 Appendix ..... 131
4.8 References ..... 133
**5 Conclusion ..... 137**

**List of Publications ..... 139**

# 1 General Introduction

## 1.1 Limitations of Methane Utilization

Methane makes up to 90% of the composition of natural gas.[1, 2] Natural gas can be found in gas reservoirs, associated gas, shale gas, gas hydrates, etc..[2-4] Exploitation of shale gas deposits increased the availability of natural gas, helping to shift the power generation to lower carbon emission and higher energy efficiency.[2, 5] The use of associated natural gas, a byproduct from oil extraction, poses a challenge for the commercial availability. Governments and the oil industry have made substantial investments to utilize and conserve this associated gas.[3] However, the fast depletion rate of many oil wells makes the planning of infrastructure for the commercial consumption of gas, such as costly pipelines, difficult.[1] In addition to economic constraints, technical and local environmental restrictions lead to flaring, venting or re-injection of natural gas.[3, 4, 6, 7] Flaring is considered to be the better option, as methane has a 28-36 times stronger global warming potential than $CO_2$.[1, 3, 4, 8] Over the last decades approximately 140-170 billion cubic meters of natural gas were flared annually.[1, 4, 9-11] The value of flared natural gas in 2012 was estimated to be approximately $20 billion.[12]

Thus, the conversion of methane to methanol is a promising route to minimize or exterminate the current situation of unused methane with advantages for the environment and economics.[13] Methanol is easier to transport and it can be potentially utilized as a substitute to crude oil based fuels and offers an efficient way for energy storage.[13-15] In addition, Methanol is not limited as an energy carrier, but it finds its importance as a valuable $C_1$ feedstock for the production of chemicals such as acetic acid, formaldehyde, dimethylether.[16, 17]

## 1.2 Conventional Conversion of Methane

About 90% of worldwide methanol is produced from natural gas.[18] Currently, methanol is synthesized via two steps.[14, 19] The first step is the catalytic conversion of methane to syngas, where a mixture of $H_2$ and CO is formed by steam or dry reforming (eq. 1.1, 1.2). Dry reforming of methane leads to a higher CO:$H_2$ ratio,[20, 21] and is suitable for the synthesis of alcohols and higher hydrocarbons.[22, 23]

$$CH_4 + CO_2 \rightleftharpoons 2\,CO + 2\,H_2 \qquad \Delta H°_{298K} = 247\ kJ/mol \qquad 1.1)$$

$$CH_4 + H_2O \rightleftharpoons CO + 3H_2 \qquad \Delta H°_{298K} = 206\ kJ/mol \qquad 1.2)$$

Dry and steam reforming reactions are highly endothermic and require high temperatures. However, dry reforming must be performed at low pressures as the reverse water-gas shift reaction leads to the partial reaction of the produced $H_2$ with the $CO_2$ reactant to water. High yields of $H_2$ can be achieved by steam reforming as the produced reacts with water and produces additional $H_2$. Typical dry reforming catalysts are Ni or noble metal-based catalysts.[24-28] The reaction is thermodynamically favored at temperatures higher than 1000 K.[29-32] However, Ni catalysts suffer under deactivation due to coke deposition at high temperatures.[33-35] Although noble metal catalysts show high activity and resistance to coke deposition, their utilization is limited due to their costs and availability.[33]

The next step is the conversion of syngas to methanol over a Cu/ZnO/$Al_2O_3$ catalyst at typically 200-300 °C and 50-100 bar.[36] Approximately 60% of the worldwide methanol production is realized via the Johnson Matthey process, followed by the Lurgi process with 27%.[36]

$$CO + 2\,H_2 \rightleftharpoons CH_3OH \qquad \Delta H°_{298K} = -91\ kJ/mol \qquad 1.3)$$

$$CO + H_2O \rightleftharpoons CO_2 + H_2 \qquad \Delta H°_{298K} = -41\ kJ/mol \qquad 1.4)$$

$$CO_2 + 3\,H_2 \rightleftharpoons CH_3OH + H_2O \qquad \Delta H°_{298K} = -50\ kJ/mol \qquad 1.5)$$

The overall reaction of syngas is including reaction equilibria between the hydrogenation of CO (eq. 1.3), water-gas shift reaction (eq 1.4), and $CO_2$ hydrogenation (eq. 1.5).[37] Mechanistic insights by radiolabeling proved that methanol is formed via $CO_2$ hydrogenation.[38]

$$S = \frac{\text{moles } H_2 - \text{moles } CO_2}{\text{moles } CO_2 + \text{moles CO}} \qquad 1.6)$$

For the ideal conversion of CO and $CO_2$, the given stoichiometric number *S* should be two. Most known processes are operated with an excess of $H_2$ at values from *S* = 2.8 – 3 (eq. 1.6).[36, 38]

## 1.3 Selective Oxidation of Methane to Methanol

The selective conversion of methane to methanol remains a pivotal challenge in catalysis research. One of the main challenges of the selective oxidation of methane to methanol is the activation of the C-H bond. The dissociation energy for the C-H bond of methane is 440 kJ/mol and requires harsh conditions, such as high temperatures or highly reactive agents for the activation. Due to its highly symmetric tetrahedral structure, the methane molecule has no induced dipole moment. The low polarization of the molecule in combination with its structure makes methane sterically hindered to nucleophilic attacks.[39] In addition, its low proton affinity and extremely high p$K_a$ value of approximately 40 pose a hurdle for the methane activation by acid/base catalysis.

Another reason for the difficulty is the C-H bond dissociation energy of methanol, which is only 47 kJ/mol lower than methane, and therefore undergoes overoxidation to carbon dioxide. Catalytic systems for methane oxidation have to efficiently activate the molecule and protect the formed intermediates from overoxidation.[12] Ideally, the utilization of molecular oxygen is preferred for the selective/direct oxidation of methane to methanol. Molecular oxygen in its ground state is a diradical and hence in a triplet state.[40] On the other hand the ground state of hydrocarbons is considered to be a closed shell with a singlet state. According to Wigner's spin selection rule, chemical reactions involving only singlet and triplet states are forbidden.[40] A catalyst is necessary with the ability to induce a spin inversion for the generation of active oxygen species.[41] Another difficulty is that the oxidation of methane to methanol only requires the insertion of one oxygen atom of the oxygen molecule. Therefore, a suitable catalyst has to not only dissociate an oxygen molecule but also needs to stabilize the second oxygen atom.[41]

Strategies for the selective oxidation of methane to methanol can be found in different research disciplines. Activation of the C-H bond of methane can be achieved by homogeneous organometallic catalysts via electrophilic substitution in polar media. Shilov et al. reported the first functionalization of the C-H bond of methane, where $K_2PtCl_4$ was able to convert methane to $CH_3OH$ and $CH_3Cl$.[42] Following Shilovs work, Periana et al. have reported the direct oxidation of methane over a Pt(II)-bipyrimidine complex in highly concentrated $H_2SO_4$.[43]

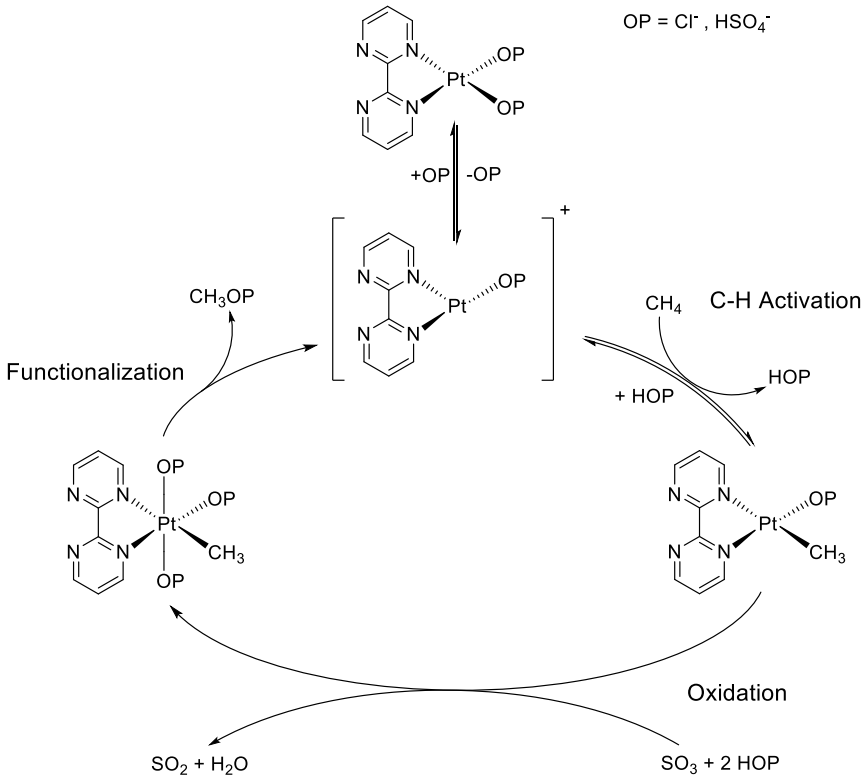


**Figure 1** Reaction mechanism for Periana systems.

Bipyrimidine as ligands helped to stabilize the noble metal and maintained the solubility of Pt(II). Methane reacted first to methyl bisulfate and subsequently hydrolyzed to methanol. The catalytic cycle consists of the C-H bond activation, oxidation and functionalization step, with the oxidation step as the rate limiting step (Figure 1).[44] High yields were possible to achieve as the electron-withdrawing nature of the sulfate group protected the formed methyl bisulfate against further oxidation.[43, 44] However the utilization of concentrated $H_2SO_4$ faces challenges such as separation of produced methanol, corrosion resistant materials, and the repeated regeneration of $H_2SO_4$.[45]

In nature, enzymatic system can convert methane at ambient conditions and high selectivity towards methanol. Methanotrophic bacteria with particulate methane monooxygenase (pMMO) or soluble methane monooxygenase (sMMO) are known to form methanol from methane with oxygen.[46-49] Active sites for sMMO have been reported to be diiron site [46, 50] and for pMMO membrane bound Cu sites[46, 48, 49]. The sMMO consists of α, β, and γ subunits, where the active diiron site resides within a four-helix of the α-subunit (Figure 2A).[46, 50] pMMO is built up by pmoB (α), pmoA (β) and pmoC (γ) subunits with the active copper sites located in the pmoB subunit

(Figure 2B).[46, 48] Although biocatalysts offer a promising route for the selective oxidation of methane to methanol, challenges remain for the industrial applications.

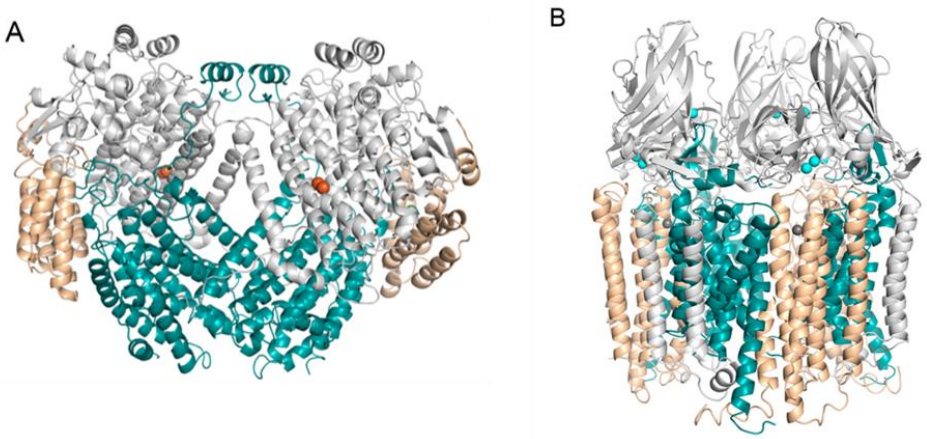


**Figure 2** Overall architecture of MMOs. (A) The sMMO hydroxylase (MMOH, PDB accession code 1MTY) with α subunits shown in gray,β subunits shown in teal, and γ subunits shown in wheat. Each α2 β2 γ2 dimer contains two diiron active sites (orange spheres). (B) The pMMO trimer (PDB accession code 3RGB) with pmoB subunits shown in gray, pmoA subunits shown in teal, and pmoC subunits shown in wheat. Copper ions are shown as cyan spheres and zinc ions are shown as gray spheres. (Reprinted with permission from ref 46)

The regeneration after one catalytic cycle through nicotinamide adenine dinucleotide (NADH) for the efficient utilization of oxygen is a huge barrier to the commercialization of MMOs.[51] Furthermore, the slow growth rates, enzyme density, deactivation through product inhibition (methanol accumulation) and mass diffusion limitations of methane and oxygen are remaining challenges for higher productivity.[51-53] Cost factors and lifetime of enzymes have not been considered since biocatalysts are considered to be active for a long period.[53] However, lifetime of these enzymes is still unknown.

The activity and high selectivity of Fe and Cu metalloenzymes towards methanol motivated scientists to study Fe and Cu hosted in the confined environment of zeolites for the selective oxidation of methane to methanol. The first direct conversion methane to methanol over zeolites was performed over Fe-exchanged ZSM-5 materials.[54, 55] Main drawback of Fe containing zeolite is the restriction to $N_2O$ and $H_2O_2$ oxidants.[56-58] Activation and conversion of methane to methanol with molecular oxygen over Cu-exchanged zeolites was first demonstrated by Groothaert et al..[59] A Cu-ZSM-5 was

first activated in oxygen at 450 °C, followed by methane reaction at 200 °C. This led to further improvements and the widely used stepwise reaction procedure consisting of 1) high temperature activation in oxygen, 2) methane reaction and 3) steam assisted methanol desorption.[12, 60, 61] The stripping of methanol with steam from the catalyst leads to the deactivation of the active Cu-species in Cu-zeolites and the catalyst has to be regenerated before entering another cycle. The current low active site density and reaction limitation portrays a major challenge for the utilization of Cu-zeolites. Despite major hurdles, Cu-zeolites are still attractive and promising candidates for industrial processes. Rapid methanol yield improvement via optimization of preparation methods and reaction conditions together with high availability and cost-efficiency have shown the high potential of Cu-zeolites.

## 1.4 Zeolites

Zeolites are microporous crystalline aluminosilicates with ordered channels of molecular dimensions. Historically, zeolites were first mentioned in 1758 by the Swedish mineralogist Axel Fredrik Cronstedt, the discoverer of Nickel.[62] After the discovery, zeolites were mostly ignored by chemists for the next 200 years. Gradually, dehydration-hydration cycles,[63] ion-exchange properties,[64] absorption of organic liquids[65], and commercial uses of natural zeolites were observed in the 20$^{th}$ century [66]. Inspired by the good separation and adsorption properties of natural chabazite (CHA) and mordenite (MOR), Barrer synthesized CHA as the first zeolite structure.[67] Due to their catalytic activity, zeolites are commercially utilized in petrochemistry for fluid catalytic cracking (FCC), separation, hydrocracking, isomerization, dewaxing, etc..[62, 68] Application of zeolites in other fields can be found for water treatment, waste treatment, construction, conversion of biomass feedstock, biotechnology, $NH_3$-SCR, etc..[68-71] To date, 255 different zeolite types are known[72] with a rapid growth rate.[73]

The zeolite structure is composed of tetrahedral $TO_4$, building blocks, where T stands for Si or Al. Those primary building blocks are linked by a corner-sharing network through bridging oxygen atoms, which can be arranged into different secondary building blocks (Figure 3).[74] According to Löwenstein's rule, the $n_{Si}/n_{Al}$ ratio (Si/Al) is limited to Si/Al ≥ 1 and hence forbids the linkage of two Al tetrahedra Al-O-Al.[75] A zeolite framework type is described by its size of pore openings and the dimensionality of the channel system (Figure 3).[76] The pore openings are defined by the number of T-atoms of the rings. 8 membered rings (MR) are considered as small, 10 MR as a medium, and 12 MR as large pore opening. The sizes are approximately in 4.1, 5.5, and 7.4 Å, respectively.[76] Internal zeolite network comprises interconnected cages and channels, creating a dimensionality of one to three. Movements of ions or molecules are restricted in smaller cages or rings in the size of 6 MR. But ions and molecules can enter the intracrystalline system of zeolites with larger rings.

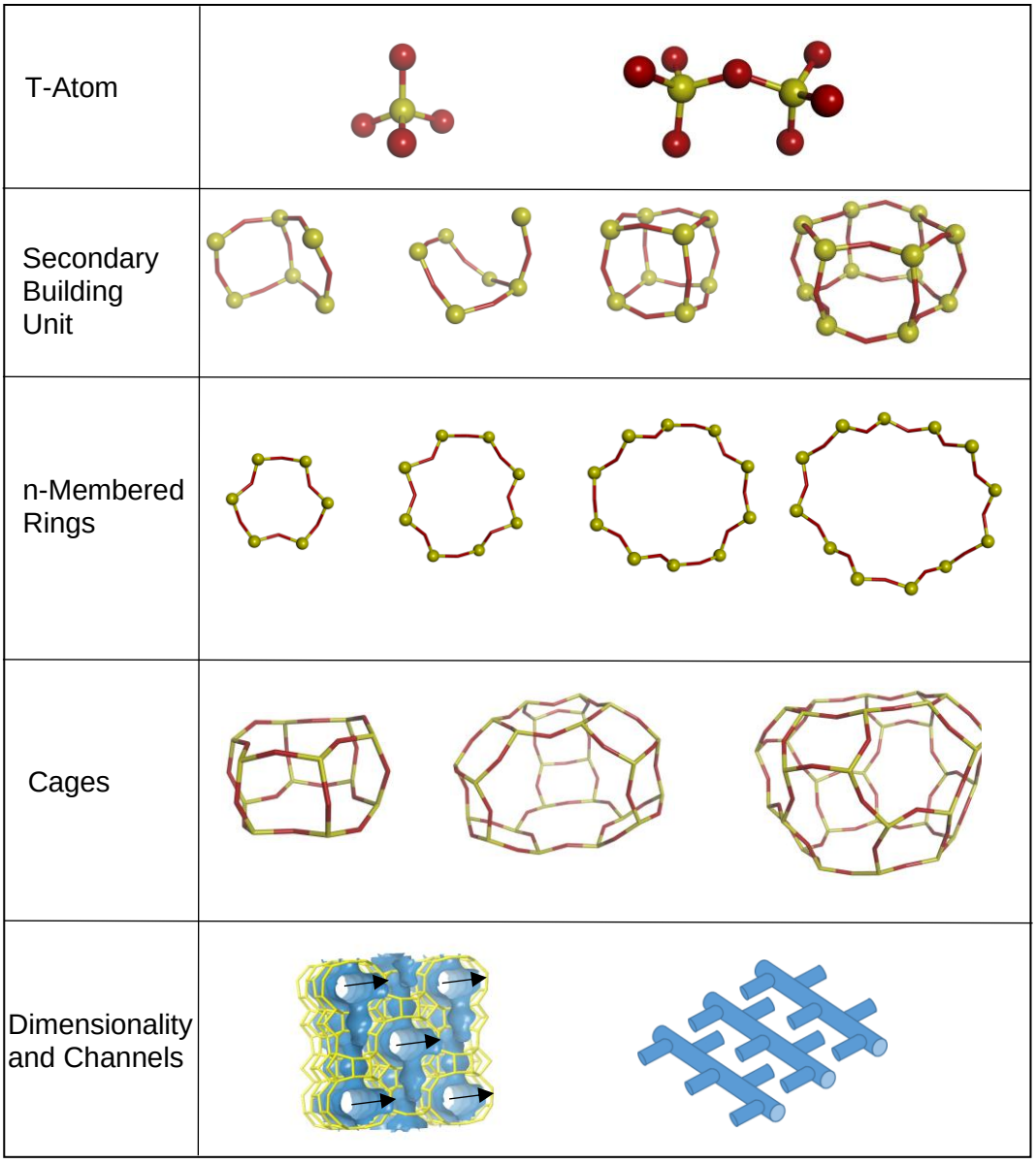


**Figure 3** Structural features of Zeolites

The main building units of zeolites are $SiO_4$ tetrahedra, with the $Si^{4+}$ ions partially replaced by $Al^{3+}$. The introduction of a trivalent Al atom into the zeolite framework creates a negative charge that gets balanced by an $H^+$, $Na^+$, $NH_4^+$, etc. Compensating protons $H^+$, or the bridging OH group between the Si-(OH)-Al, act as Brønsted acid site (BAS) in zeolites (Figure 4).[77] BAS are responsible for the high ion exchange capacity of zeolite and the amount of BAS can be changed by variation of Si/Al ratios.[78, 79] In addition, BAS in zeolites are responsible for acid based catalytic applications in the petrochemical industry for FCC, methanol to olefins (MTO), methanol to gasoline (MTG) and hydroisomerization of hydrocarbons.[77] Next to framework bound Al, extra framework Al (EFAl) species are also present. EFAl is considered as Lewis acid sites

(LAS). In contrast to framework bound Al species, EFAl species are not as well defined.[77] EFAl is created at severe high temperatures, steaming, acid and base leaching.[74, 77] Overall, the degree of framework dealumination and thus the formation of EFAl is influenced by Si/Al ratios, method of dealumination, nature of co-cations and specific T-sites of the zeolites.[77]

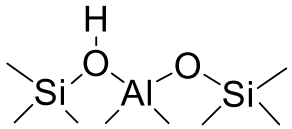


**Figure 4** Scheme of a BAS in a zeolite.

The strength of the BAS in zeolites in combination with the occurring spatial constraints of the zeolite framework influences the adsorption of small molecules, ions, and the formation of metal-oxo clusters. Formation and incorporation of metal (M) M-O-M structure, similar to the enzymatic active sites, are supported by the zeolite environment and BAS. Spatial confinement allows the free diffusion of Cu species within the zeolite framework and hinders the formation of Cu aggregations. Furthermore, the electronic confinement (BAS) allows the partial reduction of $Cu^{2+}$ to $Cu^{+}$ and impedes further reduction to metallic Cu.[80]

## 1.5 Cu-Oxo Cluster in Zeolites

### *1.5.1 Nuclearity of Cu-Clusters Hosted in Zeolites*

The catalytic property of Cu in zeolites for the selective oxidation of methane to methanol is based on the exceptional characteristics of the constrained environment of zeolites. The electrostatic attraction by the negative charge, created by an Al substitution, is the main driving force for the incorporation of cationic Cu species in zeolites.[60] Several Cu-oxo clusters in different zeolite frameworks have been reported for the selective oxidation of methane to methanol.[12, 60, 61] Direct comparisons of reported Cu-zeolites are sometimes limited due to the different preparation methods.[60, 81]

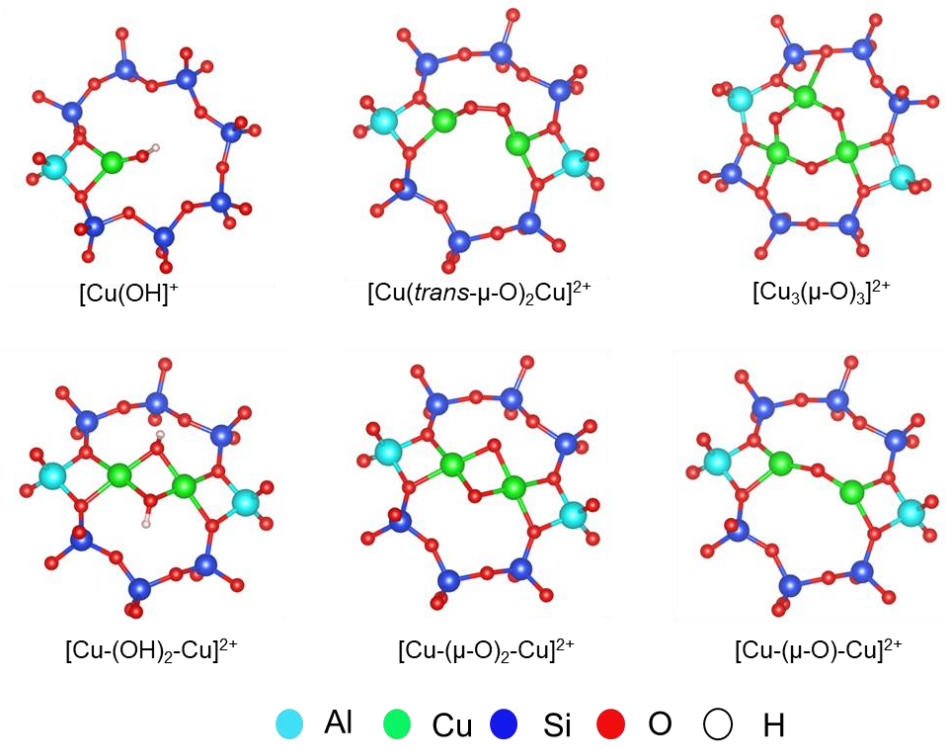


**Figure 5** Proposed Cu-oxo clusters, active for the selective oxidation of methane to methanol. Al atoms are indicated in blue, Cu in green, Si in blue, Oxygen in red and Hydrogen atoms in white. All represented structures are located in an 8 MR.

In general, the aqueous ion-exchange is the most prominent method for the introduction of Cu-species into the zeolite framework.[59, 81-97] Efficient formation of Cu-

zeolites has been reported by using the H-form for the Cu-exchange of the respective zeolites. The presence of co-cations such as $Na^+$ is known to significantly influence the formation of Cu-oxo sites and lead to an activity drop.[87, 90] In addition Grundner et al. showed the importance of pH controlled aqueous ion exchange to prevent Cu-agglomeration, resulting in inactive Cu-spectators.[88] Furthermore, the presence of co-cations leads to heterogeneous Cu-speciation in the zeolites. Investigation on Cu-zeolites has been performed by an extensive combination of infrared (IR) spectroscopy, ultraviolet-visible (UV-Vis) spectroscopy, X-ray absorption fine structure (XAFS), and density functional theory (DFT) studies, showing the complexity of the identification of Cu-oxo cluster in zeolites.[60, 61]

Grootheart et al. were the first to report the activity of a bis($\mu$-oxo)dicopper [Cu($\mu$-O)$_2$-Cu]$^{2+}$ in Cu-ZSM-5 as the active site for the selective oxidation of methane to methanol in a stepwise reaction.[82] The methane reaction was further observed by an intense UV-Vis band at 22700 cm$^{-1}$, which was formed and consumed during the reaction. In 2009, Woertink et al. proposed a mono($\mu$-oxo)dicopper [Cu-($\mu$-O)-Cu]$^{2+}$ species responsible for the selective oxidation of methane to methanol.[98] These results were obtained in combination with $^{18}O$ labeling experiments[99, 100], and DFT studies. The focus shifted on Cu-MOR, which gave a significant raise in methanol yield.[60, 61] First reports on Cu-MOR reported [Cu-($\mu$-O)-Cu]$^{2+}$ and [Cu-($\mu$-O)$_2$-Cu]$^{2+}$ as possible active sites.[86, 101-103] The structures were investigated by UV-Vis and XAFS. Differentiation between [Cu-($\mu$-O)-Cu]$^{2+}$ and [Cu-($\mu$-O)$_2$-Cu]$^{2+}$ through EXAFS were not possible to achieve due structural similarity of both clusters and limited accuracy of conventional EXAFS fitting procedure.[86] Grundner et al. investigated a Cu-MOR with high homogeneity of trimeric Cu-oxo cluster [Cu$_3$($\mu$-O)$_3$]$^{2+}$.[88] With the help of DFT assisted EXAFS analysis and IR spectroscopy, the [Cu$_3$($\mu$-O)$_3$]$^{2+}$ cluster was proposed to be located at the pore mouth of 8 MR-side pockets, stabilized by two framework Al. The MOR used for this study were all in H-form without the negative influence of co-cations. Monomeric species in Cu-zeolites were also proposed to be active for the selective oxidation of methane.[104-106] Next to monomeric species, a pair of monomeric [Cu(OH)]$^{2+}$ species, which formed a [Cu-(OH)$_2$-Cu]$^{2+}$-like structure, in Cu-MAZ, was also reported to selectively convert methane to methanol.[107]

The emerging research on small pore zeolites for $NH_3$-Selective catalytic reduction (SCR), led to the investigation of Cu-CHA, and the attribution of peroxo-dicopper [Cu-

(*trans*-$\mu$-O)$_2$-Cu]$^{2+}$ cluster by XAFS studies.[95] This led to the conclusion that dicopper species are responsible for the selective oxidation of methane to methanol. In addition to active sites, a significant amount of Cu-spectators are reported to be present in 6 MR of Cu-CHA. Similar results were observed by Brezicki et al. where the active site in Cu-MOR has been attributed to a [Cu-($\mu$-O)-Cu]$^{2+}$.[81] Also larger clusters such as tetrameric and pentameric Cu-oxo cluster have been reported to be active for the oxidation of methane to methanol.[108] Although a variety of Cu-oxo clusters hosted in zeolites have been reported, constant development and optimization have led to a successful increase of methanol yield and shedding light on the efficient formation of Cu-oxo cluster in zeolites.

### *1.5.2 Methane Activation over Cu-Oxo Cluster*

Computational studies showed that despite their different intrinsic activity, Cu-oxo and Cu-OH clusters with different nuclearities hosted in zeolites can selectively activate methane.[109] DFT-calculations revealed that the spin-densities on the bridging Cu-O-Cu oxygen atom is an important factor for the C-H bond activation of methane.[98, 109, 110] The reactive bridging oxygen has a radical nature and promotes a homolytic cleavage of the C-H cleavage, resulting in a $CH_3$-radical. Pidko et al. concluded that both [Cu-($\mu$-O)$_2$-Cu]$^{2+}$ and [Cu$_3$($\mu$-O)$_3$]$^{2+}$ can activate the C-H bond, but only the trimeric cluster was able to provide a favorable reaction pathway towards methanol.[110] Similar to these results Kulkarni et al. predicted the [Cu$_3$($\mu$-O)$_3$]$^{2+}$ cluster to be more active and comparison between different transition metals revealed the following activity towards C-H activation in decreasing order: Cu > Ni > Co> Fe.[111] Experimental data and theoretical calculation presented by Zheng et al., provide evidence on the utilization of the second bridging oxygen of the trimeric cluster upon the increase of methane pressure.[112] Another study by Zhao et al. compared [Cu-($\mu$-O)-Cu]$^{2+}$ and [Cu-(*trans*-$\mu$-O)$_2$-Cu]$^{2+}$ as active sites, concluding that the methane activation is only feasible for [Cu-($\mu$-O)-Cu]$^{2+}$.[104] Additional investigation on the activation process revealed the preferred formation of [Cu-($\mu$-O)-Cu]$^{2+}$ after oxygen activation.

Next to the importance of the radical character of the bridging oxygen atom, the influence of the zeolite confinement and resulting geometries and flexibility of the Cu-oxo structure have been determined as a crucial factor for the C-H bond activation of

methane.[109] Raman measurement in combination with DFT calculation revealed that more active [Cu-($\mu$-O)-Cu]$^{2+}$ cores can be found in the constrained region regions of a zeolite.[102, 113] Vanelderen et al. identified similar [Cu-($\mu$-O)-Cu]$^{2+}$ structures in MOR and ZSM-5 with different kinetic behavior for the selective oxidation of methane.[102] The more constrained MOR, with its 8 MR side pockets, analogous to the confinements of a metalloenzyme, contribute to the different activity. An investigation on the activity of [Cu-($\mu$-O)-Cu]$^{2+}$ in different zeolite topologies such as AEI, CHA, AFX, and MFI by Mahyuddin et al. points out to a decreased activity due to a decreasing Cu-O-Cu angle.[114] DFT simulation on the reactivity of mono copper-oxo sites in Cu-CHA, proposed a complementary route of methane activation in zeolites.[105] However, spectroscopic studies found such monomeric Cu-species to be inactive.[95, 115]

## 1.6 X-Ray Absorption Spectroscopy

### *1.6.1 Fundamentals of XAS*

An important tool for the investigation of Cu-oxo clusters is the utilization of X-ray absorption spectroscopy (XAS). The utilization of Cu K-edge XAS, or in detail XAFS, helped to address element specific oxidations states, local geometries, and the chemical environment under in situ conditions. XAFS offers various opportunities and is successfully applied in different scientific fields ranging from physics, chemistry, medicine, and biology.[116] Most of the experiments are performed at synchrotrons, which provide the most intense X-ray source[117] with electrons in the storage rings reaching energies more than 1 GeV.

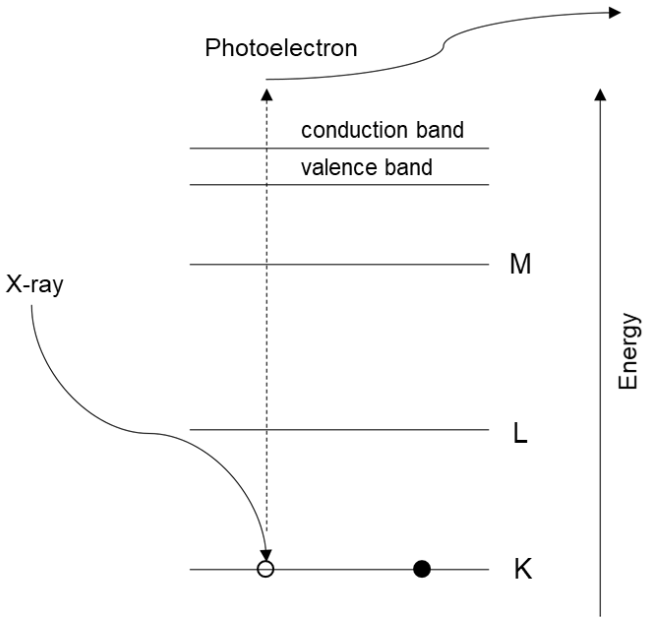


**Figure 6** Absorption of an X-ray by an atom, where a core-electron is excited, and a photoelectron is emitted and leaving a core-hole.

X-rays can be divided into different energy regions: soft X-rays with less than 2 keV, tender X-rays between 2 to 6 keV, and hard X-rays with energies higher than 6 keV.[118] The continuous development of synchrotrons and detection devices enabled access to increased intensity across a broad energy range, high brilliance, and tunability, which are some of the important synchrotron light properties.[119]

XAFS is based on chemical and physical states of the absorbing atom and recorded spectra are therefore giving sensitive information on the oxidation state, coordination, distances, and species of surrounding atoms of the selected element.[120] Basic principle on a XAFS measurement is the modulation of X-ray absorption probability at energies close and above the binding energy of a core-level electron (Figure 6).[120] X-ray lights are absorbed by matter through the photoelectric effect, where a X-ray photon is absorbed by a core electron. Incident X-ray with less energy than the binding energy of the core level hits an atom. With further increase of the incident X-ray energy, in respect to the binding-energy, the core-electron gets ejected into continuum. The Lambert-Beer law describes the attenuation and therefore the absorption of X-rays, when interacting with matter (Figure 7).

$$I = I_0 e^{-\mu t} \qquad 1.7)$$

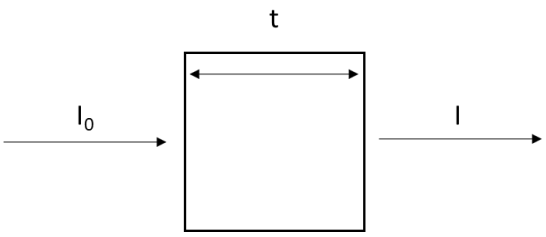


**Figure 7** X-ray absorption of a sample according to the Lambeer law $I = I_0 e^{-\mu t}$.

$I_0$ is the incident X-ray on the sample, μ is the absorption coefficient (describing the probability of the absorption of X-rays), t is the thickness of the sample, and I is the transmitted intensity. μ is further described as:

$$\mu = \rho Z^4 / A E^3 \qquad 1.8)$$

ρ is the sample density, Z the atomic number, A the atomic mass, E the X-ray energy. Every atom of the respective element has well defined core-level electrons with absorption edges and an XAFS measurement is the energy dependency between the absorption coefficient μ and the binding energy of a known core level of the atomic

species.[120] The absorption of X-ray by an atom leads to the excitation of a core-level electron and leaves a core-hole together with a photoelectron. The created core-hole quickly decays and is filled by a higher energy core-level electron. The emitted fluorescence gives raise to element specific fluorescence lines such as $K_\alpha$, in case of an electron drop from L to K. Another process can take place due to the Auger effect, where an electron drop from a higher level occurs and a second electron is ejected into continuum. Therefore, XAFS measurement can be performed via transmission

$$\mu(E) = \ln (I_0/I_t) \qquad 1.9)$$

or fluorescence detection

$$\mu(E) = I_f/I_0 \qquad 2.0)$$

where $I_f$ is the intensity of the fluorescence signal. A typical XAFS measurement can be seen in Figure 8.

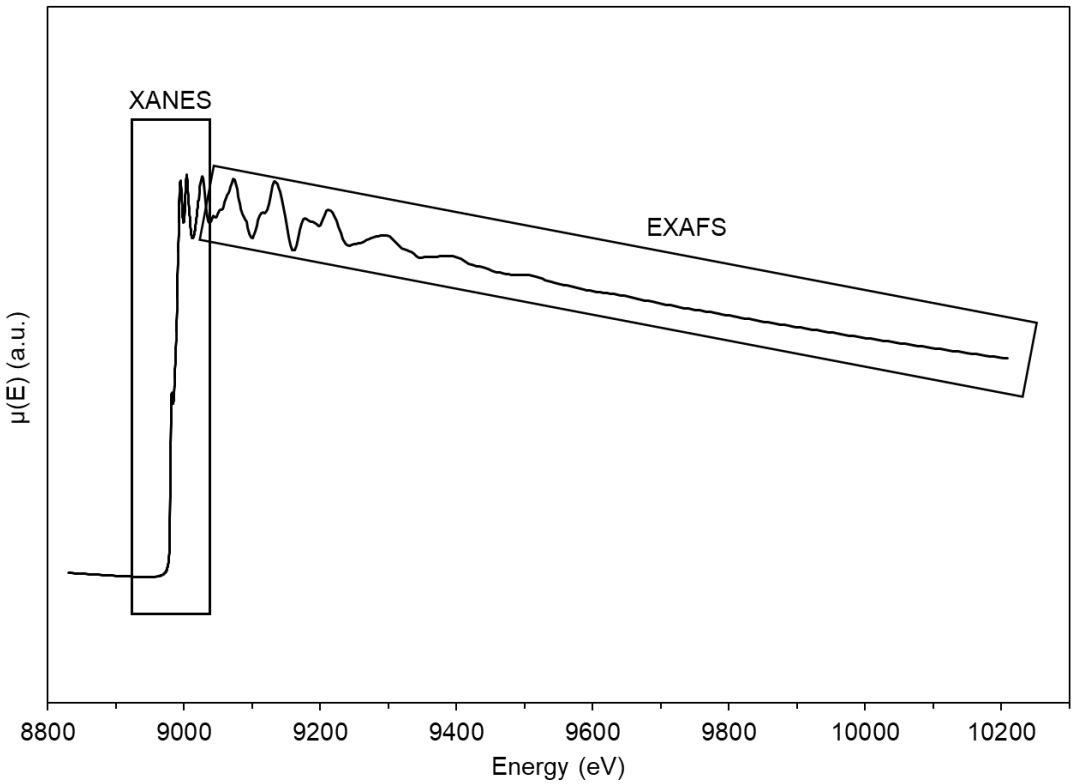


**Figure 8** XAFS spectrum of a Cu-foil divided into XANES and EXAFS.

The XAFS spectrum is divided into X-ray near edge structure (XANES) and extended X-ray absorption fine structure (EXAFS). The region at low energies at the ionization threshold is referred to as XANES, which is typically limited to 30 eV above the main edge.[121, 122] Above 30 eV of the main edge electron, mainly electron scattering processes are described by the EXAFS region. The transition range between XANES and EXAFS is rather smooth and cannot be separated.

### *1.6.2 X-Ray Absorption Near Edge Structure*

Spectral features seen in XANES are much more intense than EXAFS oscillations and decent information can be already obtained at much lower concentrations of the analyzed element.[117] The physical principles for XANES and EXAFS region are the same, however, XANES is governed by multiple diffusion and multi electronic interactions. The analysis of XANES spectra is much more complicated than EXAFS. At lower kinetic energy the mean free path of the photoelectron drastically increases.[123, 124] In addition, the XANES region is very sensitive to a wide range of absorber-scatterer distances., enabling the extraction of three-dimensional structure information. Complications on XANES simulations arise due to the number of interactions and multiple scattering pathways.[124]

XANES spectra are utilized for the determination of the oxidation state, three-dimensional structure (local geometry), and as a probe of the electronic structure.[123] A typical XANES spectra can be seen in Figure 9. 3d transition metals are usually evaluated by the K-edge, which is located in the hard X-ray regime.[125] Characteristic features are the main edge, corresponding to 1s to 4p states, and the pre-edge peak, which involves the transition of 1s to 3d.

The main absorption edge is also referred to as a white line since XAS spectra were recorded on films in the past and an intense transition would absorb all of the incident X-rays.[123] Usually, the edge position is chosen as the energy of the inflection point, the energy at 50% of the maximum intensity, or the average of the energies at 20% and 80%.[125] Basic information on the oxidation state can be retrieved on the relative edge positions. Metal oxides of an element with higher oxidation states shift to higher energies, which can be explained by the electrostatic charge as it takes more energy to excite an inner electron on a positively charged metal ion.[124]

However, this phenomenon does not correlate directly with ionization.[82] Another parameter such as the bond length to the nearest neighbour also influences the edge position. As the absorber-scatterer distance increases, the higher the energy of continuum state gets as $1/R^2$.[123]

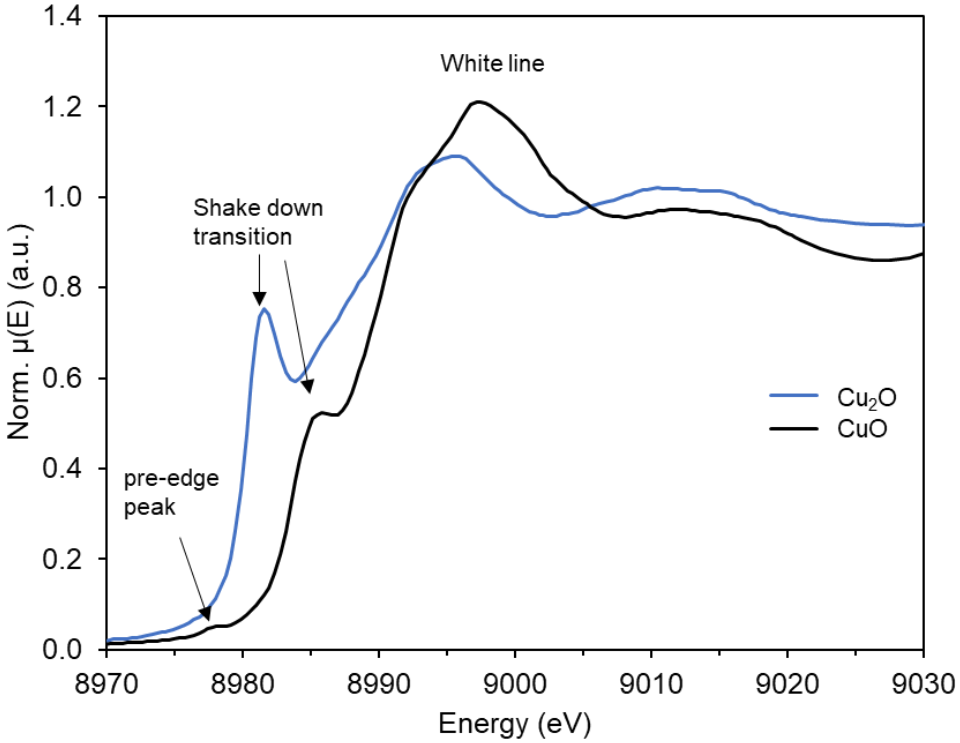


**Figure 9** Normalized XANES spectra of a $Cu^{2+}$ reference (black, CuO) and a $Cu^{+}$ reference (blue, $Cu_2O$).

The pre-edge feature of the K-edge corresponds to the dipole forbidden 1s to 3d transitions. CuO shows a small pre-edge feature, whereas $Cu_2O$ has no pre-edge feature (Figure 9). The difference arises because $Cu^{2+}$ has a $d^9$ configuration and $Cu^{+}$ a $d^{10}$. Transition to occupied states is forbidden according to the Pauli exclusion principle. Pre-edge features, as in the case of $Cu^{2+}$, can be seen due to 3d+4p mixing and direct quadrupolar coupling.[123] As a consequence, the intensity of the pre-edge feature gives information on the geometry of the probed atom. Change of inversion symmetry from octahedral to tetrahedral configuration leads to mixing of p-orbitals of the outer valence with the d-orbitals of the lower valence shell, resulting in increased p-character of the metal d-orbitals.[126] The intensity of the pre-edge increases in the following order: octahedral < square-pyramidal < tetrahedral.[123]

XANES spectra of CuO and $Cu_2O$ show a shake down transition before the main edge. The shake down transition feature finds its origin due to the electric dipole allowed 1s to 4p transition.[123, 127] $Cu^+$ complexes with two coordinated ligands have the most intense peak due to repulsive interactions of $4p_z$ orbital, which results in the intense 1s to $4p_{x,y}$ transition. [127] The degeneracy of $4p_x$ and $4p_y$ is split in energy via the addition of a third ligand. In $Cu^{2+}$ complexes, the shake-down transitions occur due to the large covalency.[123]

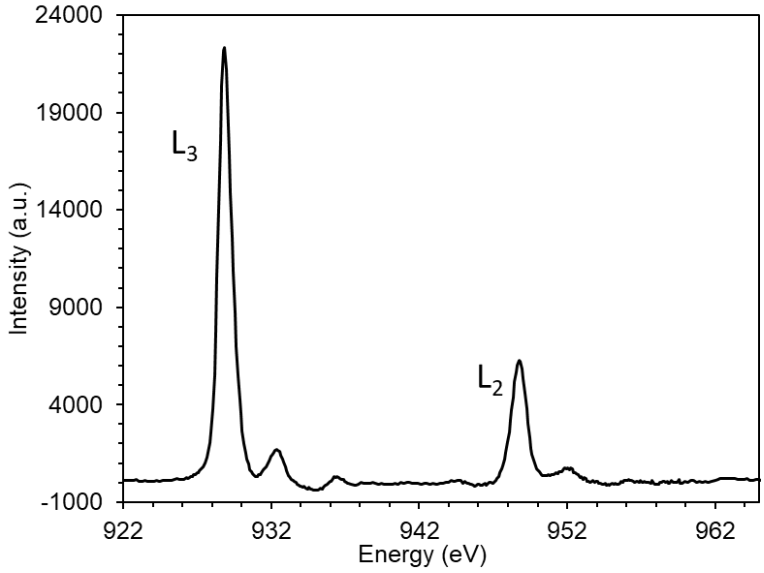


**Figure 10** Cu $L_{3,2}$-edge measurement of $O_2$ activated (at 500°C) Cu-MOR (adapted with permission from ref[91])*.

XAS is not limited to the K-edge, but also other edges such as the L-edge can be probed. The $L_{3,2}$-edges show the intense electric dipole $2p^63d^n$ to $2p^53d^{n+1}$ transition. The $2p^5$ configuration with an angular momentum of l = 1 and couples with the spin angular momentum s=1/2, giving rise to the total angular momentum J = (s+1) =3/2 and 1/2. The main intensity for Cu $L_3$-edge corresponds to the transition from $2p_{3/2}$ to $3d_{5/2}$ and $L_2$-edge the transition of $2p_{1/2}$ to $3d_{3/2}$. Compared to the K-edge, the L-edge has a higher energy resolution due to the longer core-hole lifetime of the 2p (Figure 10b). This results in a 3-4 times smaller broadening than in for K-level transition.[128]

*This figure is adapted with permission from: I. Lee, M. Lee, L. Tao, T. Ikuno, R. Khare, A. Jentys T. Huthwelker, C. N. Borca, A. Kalinko, O. Y. Gutierrez, N. Govind, J. L. Fulton, J. Z. Hu, V. Glezakou, R. Rousseau, M. Sanchez-Sanchez, J. A. Lercher, Activity of Cu-Al-oxo extra-framework clusters for selective methane oxidation on Cu exchanged zeolite, *JACS Au* **2021**, *1*, 9, 1412-1421. Copyright [2021], I. Lee, M. Lee, L. Tao, T. Ikuno, R. Khare, A. Jentys T. Huthwelker, C. N. Borca, A. Kalinko, O. Y. Gutierrez, N. Govind, J. L. Fulton, J. Z. Hu, V. Glezakou, R. Rousseau, M. Sanchez-Sanchez, J. A. Lercher, published by American Chemical Society.

In addition, instrument monochromator resolution is higher at lower energies.[129] The electric dipole transitions from p to d, making it possible to screen the covalency of the metal-ligand interactions.[129]

Cu $L_3$ and $L_2$-edge transition are split by ca 20 eV and the broadening for the $L_2$-edge is higher due to the additional Coster-Kronig Auger decay process.[129] Ratio of the main intensity $L_3$ and $L_2$-edge XANES is 2:1, since there are four $p_{3/2}$ and two $p_{1/2}$ states. However, multiplet effects redistribute the intensity ratio between the $L_3$ and $L_2$. The observed intensity ratio between $L_3$ and $L_2$ for a Cu-MOR sample is approximately 3:1 (Figure 10b). Another important feature of L-edge spectroscopy is the specific satellite features, after the intense main peak. These features are sensitive to the ligand environment and correspond to transitions of different sets of orbitals in the d-manifold.[130]

Recent progress in computational chemistry enabled the qualitative calculation of XANES spectra through time-dependent density functional theory (TDDFT).[131] The utilization of TDDFT calculations allows the prediction of spectral XANES features through the excitations of core electrons to targeted unoccupied states.[91, 132, 133] Studies of direct comparison between experimental and theoretical XANES spectra allowed identification and explanation of spectral XANES features of complicated systems.[91, 132, 133] The application of TDDFT is not limited to excited state calculations but can be also used for X-ray emission spectroscopy (XES).[134, 135]

### *1.6.3 Extended X-Ray Absorption Fine Structure*

With increasing incident X-ray energy, the photoelectron of an atom is ejected and further excited into continuum, causing scattering processes with neighbouring atoms. The propagation of the photoelectron is described as a de Broglie wave.[123]

The outgoing and backscattered photoelectron are interacting and cause constructive and destructive interferences (Figure 11), which are responsible for the oscillation. The kinetic energy of the photoelectron increases with increasing incident X-ray energy, therefore the wave vector of a photoelectron can be described as:

$$k = (2_e(E-E_0)/\hbar^2)^{1/2} \qquad 2.1)$$

where $m_e$ is the mass of an electron, $E_0$ the threshold/binding energy of a photoelectron and ħ the Planck constant.[124]

EXAFS is commonly described as χ(k), defined as the fractional modulation in the X-ray absorption coefficient and can be further described as:

$$\chi(k) = \frac{\mu(k) - \mu_0(k)}{\mu_0(k)} \qquad 2.2)$$

with μ(k) as the observed absorption coefficient and $\mu_0(k)$ as the free-atom absorption coefficient.[123]

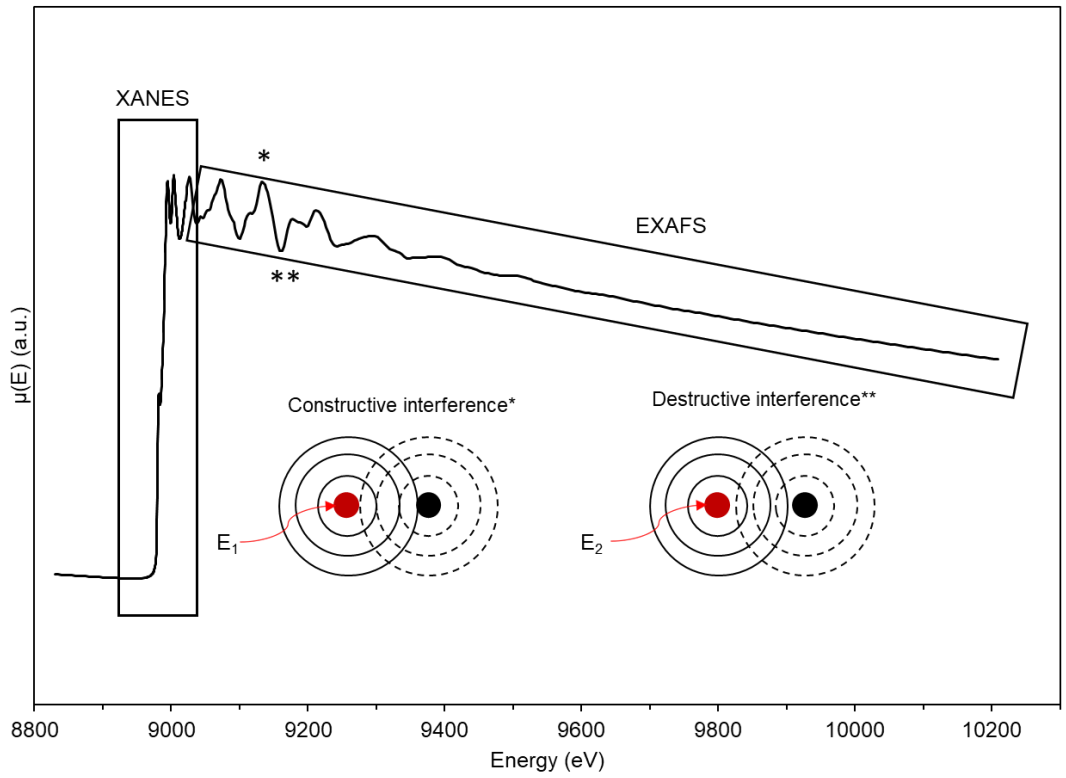


**Figure 11** XAFS spectrum of Cu foil divided into XANES and EXAFS region with a schematic of constructive interference (*) and destructive interference (**) of an outgoing and backscattered photoelectron. The absorber atom is indicated in red and the scatterer atom in black.

Figure 11 shows the case where for a given energy $E_1$ the outgoing and backscattered are in phase and the constructive interference gives rise to the probability of X-ray absorption.[124] In contrast, destructive interference can be observed for a different energy $E_2$, where outgoing and backscattered interference are out of phase. The observed EXAFS oscillation can be further described as:

$$\chi(k) = \sum_s \frac{N_s A_s(k) S_0^2}{k R_{as}^2} \exp(-2R_{as}/\lambda(k) \exp(-2k^2 \sigma_{as}^2) \sin(2k R_{as}+\Phi_{as}(k)) \qquad 2.3)$$

representing the summation of all scattering atoms near the absorber.[123] The most important parameters from eq. 2.3 for EXAFS analysis are summarized in Table 1.

**Table 1** Important fitting parameters for the EXAFS analysis.

| Parameter | Explanation |
|---|---|
| $S_0^2$ | Amplitude reduction factor |
| $N_s$ | Number of scattering/neighboring atoms |
| $R_{as}$ | Distance of the absorber and scatterer |
| $\sigma_{as}$ | Debye-Waller factor, |

The amplitude reduction factor $S_0^2$ is accounting the inelastic losses, which is usually a constant value.[123] $S_0^2$ factor is assessed by fitting of a known standard, e.g. metal foil (which was measured at the same beamline), and is applied on the samples with the same element.

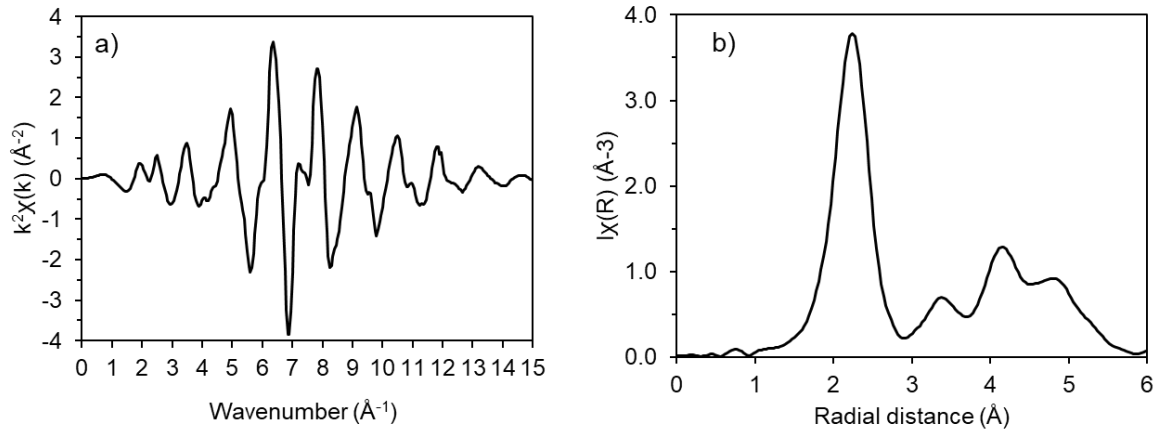


**Figure 12** Cu-foil represented as a) $k^2$-weighted EXAFS χ(k) and b) FT transformed EXAFS spectrum χ(R).

$N_s$ gives information about the number of nearest scattering neighbours and $R_{as}$ the corresponding distance between scatterer and absorber atom. The Debye-Waller factor $\sigma_{as}$ is important, as a single EXAFS measurement cannot distinguish between thermal disorders and atomic vibrations from static disorder, resulting in a deviation in absorber and scatterer distance.[123] Another factor is the mean free path of a photoelectron λ(k), which defines how fast a photoelectron can travel before scattering occurs or the core-hole is filled. $S_0^2$, λ(k), and $\sigma_{as}$ are important dampening factors, as the EXAFS amplitude decays as $1/R^2$.[123] The dampening of EXAFS limits the information of surrounding atoms to 10 Å. $A_s(k)$ and $\Phi_{as}(k)$ describe the electron dependency and the phase shift, which occurs when a photoelectron passes the potential of absorbing and scattering atoms.[123]

Conventionally the EXAFS oscillation is Fourier-transformed (FT), which gives a pseudo radial distribution function, caused by $A_s(k)$ and $\Phi_{as}(k)$. This results in a phase-shift of -0.5 Å (Figure 12).[136] Curve fitting of the processed EXAFS spectra are performed with programs such as FEFF (implemented in Artemis), where a cluster of atoms e.g. metal, metal oxide, etc. is taken and the scattering processes of a photoelectron are simulated.[136, 137]

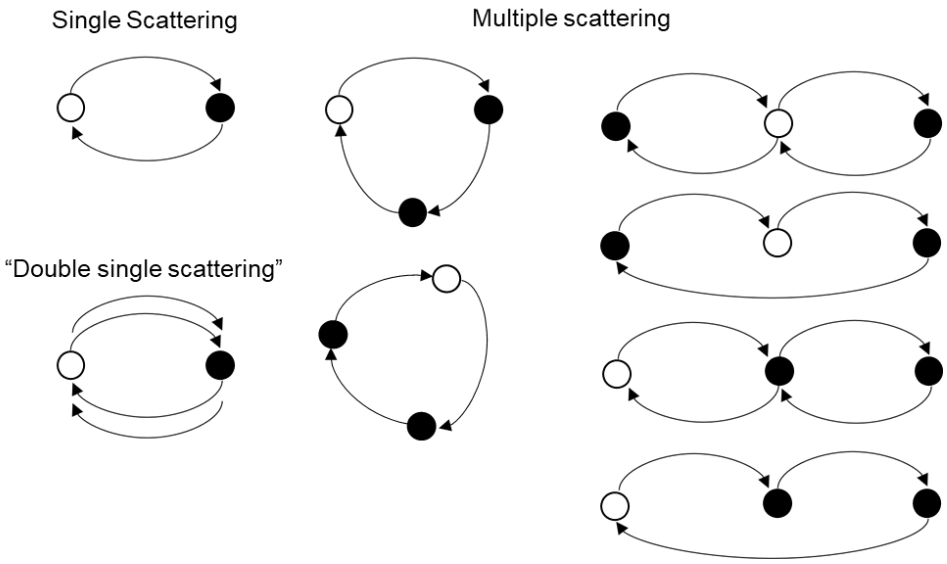


**Figure 13** Common scattering pathways of photoelectron probed during EXAFS. The hollow circles indicate the absorbing atom, where a photoelectron is ejected, and full circles indicate the scattering atoms.

Scattering processes of EXAFS involve single scattering and multiple scattering paths (Figure 13). In general, single scattering processes or pathways dominate EXAFS spectra.[120] However, crystalline materials with a well ordered structure can give rise to important multiple scattering processes.

The development of DFT enabled the simulation of EXAFS spectra in combination with molecular dynamics (MD) calculation.[138-140] Fundamental basis of XAFS and MD is the molecular structure. Structural information and atomic position relative to the absorbing atom are probed by XAFS measurements, which are similarly represented in molecular dynamics by the radial pair distribution function g(r).[141]

Compared to the conventional EXAFS analysis approach, MD-EXAFS has the advantage that even complicated scattering paths are exactly represented until outer shells. Common EXAFS fitting procedures are suitable for well-defined crystalline

materials. However, EXAFS spectra of structurally unidentified samples with convoluted scattering pattern and atoms of different elements at the same distances, are difficult to resolve by the conventional procedure. The equilibration of the molecular systems accesses several geometries (frames) by taking snapshots along the equilibration.[141] Critical fitting parameters such as the Debye-Waller factor are well resolved through DFT.[142] Similar to the EXAFS equation, MD-EXAFS are processed by utilization of:

$$\chi(k) = \frac{1}{\text{frames}} \sum_{i}^{\text{frames}} \sum_{j}^{\text{paths}} \frac{F_{ij}(k)\, S_0^2}{k\, R_{ij}^2} \exp(-2R_{as}/\lambda(k)) \sin(2k\, R_{ij} + \Phi_{ij}(k)) \qquad 6)$$

where $F_{ij}$ is the scattering amplitude, $\Phi_{ij}(k)$ is the phase shift, and $\lambda(k)$ is the mean free path of the photoelectron.[141] XAFS spectra are obtained by processing up to 1000 the frames, obtained by the snapshots,[143] via ab initio codes such as FEFF.[141, 144] The final MD-EXAFS spectrum is obtained by an ensemble average spectrum of each snapshot with up to 1000 scattering paths per snapshot.[141, 145] In order to achieve a direct comparison between experimentally obtained EXAFS and simulated MD-EXAFS, the $E_0$ has to be adjusted.[146] For the simulation of a heterogeneous environment of the absorber atom, ab initio molecular dynamics (AIMD) assisted EXAFS simulations have been proven advantageous.[147]

## 1.7 Scope of this Thesis

In the past decade, several Cu-based zeolites have been reported to be active for the selective oxidation of methane to methanol. In these materials, Cu-oxo cluster hosted in the constrained microenvironment of the zeolite are responsible for the efficient C-H bond activation and high yields of methanol. Intensive research of multiple groups contributed to important insights on the formation and activity of Cu-oxo species, leading to a rapid improvement of the performance of Cu-zeolites. However, a contradiction within the existing literature still governs the research field of Cu-zeolites for the selective oxidation of methane.

Investigation on the oxidation state of Cu during and after oxidative, autoreducing, and methane reaction conditions is subject to the first chapter. Oxidation and reduction of Cu-oxo cluster in Cu-MOR are assessed by IR spectroscopy, where the interaction of $Cu^{2+}$ and $Cu^{+}$ species can be probed by CO and NO. Particular focus is on the evaluation of oxidation states determined by XAS. X-ray induced effects on Cu-MOR at various conditions is carefully analyzed and critically compared to existing literature.

As a next step, a Cu-MOR series with an unusual high a $Cu_{eff}$ is investigated. A thorough investigation of the parent H-MOR is employed and compared to an H-MOR, which homogeneously forms Cu-oxo trimers. Framework bound Al is known to be the anchoring position for Cu-oxo species. However, little is known on the effect of EFAl on the formation and activity of Cu-oxo cluster in zeolites. Studies on the parent materials concentrate on the Al species and involve the utilization of $^{27}$Al NMR, IR-spectroscopy with *n*-hexane and pyridine, and Al K-edge XANES. Another focus of this chapter is the multi-edge analysis of Cu K and L-edge XAS in combination with theoretical tools such as AIMD-EXAFS and TDDFT-XANES for the identification of the active Cu-species.

In the last chapter, the activity of different Cu-zeolites is discussed. A Cu-MOR series with trimeric Cu-oxo clusters is compared to Cu-FER, Cu-MFI, and Cu-CHA materials. The influence of different pore and channel structures is known to influence the formation and hence the activity of Cu-oxo clusters. IR-spectroscopy for the evaluation of BAS, UV-VIS spectroscopy, and high pressure reactions are performed to evaluate the siting, nuclearity, and nature of the Cu-species, which are active for the selective oxidation of methane to methanol.

## 1.8 References


1. E. C. D. Tan, D. Schuetzle, Y. Zhang, O. Hanbury, R. Schuetzle, Reduction of greenhouse gas and criteria pollutant emissions by direct conversion of associated flare gas to synthetic fuels at oil wellheads. *Int. J. Energy Environ.,* (2018), **9**, 305-321.

2. S. Faramawy, T. Zaki, A. A. E. Sakr, Natural gas origin, composition, and processing: A review. *J. Nat. Gas Sci. Eng.,* (2016), **34**, 34-54.

3. C. D. Elvidge *et al.*, The potential role of natural gas flaring in meeting greenhouse gas mitigation targets. *Energy Strategy Rev.,* (2018), **20**, 156-162.

4. R. Calel, P. Mahdavi, Opinion: The unintended consequences of antiflaring policies—and measures for mitigation. *Proc. Natl. Acad. Sci.,* (2020), **117**, 12503.

5. D. Malakoff, The gas surge. *Science,* (2014), **344**, 1464.

6. T. A. Brzustowski, Flaring in the energy industry. *Prog. Energy Combust. Sci.,* (1976), **2**, 129-141.

7. M. R. Johnson, A. R. Coderre, An Analysis of Flaring and Venting Activity in the Alberta Upstream Oil and Gas Industry. *J. Air Waste Manag. Assoc.,* (2011), **61**, 190-200.

8. M. R. Johnson, A. R. Coderre, Opportunities for CO2 equivalent emissions reductions via flare and vent mitigation: A case study for Alberta, Canada. *Int. J. Greenh. Gas Control.,* (2012), **8**, 121-131.

9. W. Lu *et al.*, Global proliferation of offshore gas flaring areas. *J. Maps,* (2020), **16**, 396-404.

10. C. D. Elvidge, M. Zhizhin, K. Baugh, F.-C. Hsu, T. Ghosh, Methods for Global Survey of Natural Gas Flaring from Visible Infrared Imaging Radiometer Suite Data. *Energies,* (2016), **9**.

11. C. D. Elvidge *et al.*, A Fifteen Year Record of Global Natural Gas Flaring Derived from Satellite Data. *Energies,* (2009), **2**, 595-622.

12. M. Ravi, M. Ranocchiari, J. A. van Bokhoven, The Direct Catalytic Oxidation of Methane to Methanol—A Critical Assessment. *Angew. Chem., Int. Ed.,* (2017), **56**, 16464-16483.

13. G. A. Olah, Beyond Oil and Gas: The Methanol Economy. *Angew. Chem., Int. Ed.,* (2005), **44**, 2636-2639.

14. F. Dalena *et al.*, in *Methanol,* A. Basile, F. Dalena, Eds. (Elsevier, 2018), pp. 3-28.

15. K. Räuchle, L. Plass, H.-J. Wernicke, M. Bertau, Methanol for Renewable Energy Storage and Utilization. *Energy Technol.,* (2016), **4**, 193-200.

16. B. Balopi, P. Agachi, Danha, Methanol Synthesis Chemistry and Process Engineering Aspects- A Review with Consequence to Botswana Chemical Industries. *Procedia Manuf.,* (2019), **35**, 367-376.

17. G. Iaquaniello, G. Centi, A. Salladini, E. Palo, in *Methanol,* A. Basile, F. Dalena, Eds. (Elsevier, 2018), pp. 595-612.

18. M. Blug, J. Leker, L. Plass, A. Günther, in *Methanol: The Basic Chemical and Energy Feedstock of the Future: Asinger's Vision Today,* M. Bertau, H. Offermanns, L. Plass, F. Schmidt, H.-J. Wernicke, Eds. (Springer Berlin Heidelberg, Berlin, Heidelberg, 2014), pp. 603-618.

19. P. J. A. Tijm, F. J. Waller, D. M. Brown, Methanol technology developments for the new millennium. *Appl. Catal. A,* (2001), **221**, 275-282.

20. C. Buelens Lukas, V. Galvita Vladimir, H. Poelman, C. Detavernier, B. Marin Guy, Super-dry reforming of methane intensifies CO2 utilization via Le Chatelier's principle. *Science,* (2016), **354**, 449-452.

21. S. T. Oyama, P. Hacarlioglu, Y. Gu, D. Lee, Dry reforming of methane has no future for hydrogen production: Comparison with steam reforming at high pressure in standard and membrane reactors. *Int. J. Hydrog. Energy,* (2012), **37**, 10444-10450.

22. J. H. Bitter, K. Seshan, J. A. Lercher, The State of Zirconia Supported Platinum Catalysts for CO2/CH4Reforming. *J. Catal.,* (1997), **171**, 279-286.

23. O. Muraza, A. Galadima, A review on coke management during dry reforming of methane. *Int. J. Energy Res.,* (2015), **39**, 1196-1216.

24. B. Fidalgo, A. Arenillas, J. A. Menéndez, Mixtures of carbon and Ni/Al2O3 as catalysts for the microwave-assisted CO2 reforming of CH4. *Fuel Process. Technol.,* (2011), **92**, 1531-1536.

25. A. E. Castro Luna, M. E. Iriarte, Carbon dioxide reforming of methane over a metal modified Ni-Al2O3 catalyst. *Appl. Catal. A,* (2008), **343**, 10-15.

26. S. Therdthianwong, C. Siangchin, A. Therdthianwong, Improvement of coke resistance of Ni/Al2O3 catalyst in CH4/CO2 reforming by ZrO2 addition. *Fuel Process. Technol.,* (2008), **89**, 160-168.

27. C. Shi, P. Zhang, Effect of a second metal (Y, K, Ca, Mn or Cu) addition on the carbon dioxide reforming of methane over nanostructured palladium catalysts. *Appl. Catal. B,* (2012), **115-116**, 190-200.

28. P. Ferreira-Aparicio *et al.*, A Transient Kinetic Study of the Carbon Dioxide Reforming of Methane over Supported Ru Catalysts. *J. Catal.,* (1999), **184**, 202-212.

29. M. K. Nikoo, N. A. S. Amin, Thermodynamic analysis of carbon dioxide reforming of methane in view of solid carbon formation. *Fuel Process. Technol.,* (2011), **92**, 678-691.

30. S. Wang, G. Q. Lu, G. J. Millar, Carbon Dioxide Reforming of Methane To Produce Synthesis Gas over Metal-Supported Catalysts: State of the Art. *Energy Fuels,* (1996), **10**, 896-904.

31. Istadi, N. A. S. Amin, Co-generation of synthesis gas and C2+ hydrocarbons from methane and carbon dioxide in a hybrid catalytic-plasma reactor: A review. *Fuel,* (2006), **85**, 577-592.

32. M. C. J. Bradford, M. A. Vannice, CO2 Reforming of CH4. *Catal Rev.,* (1999), **41**, 1-42.

33. N. A. K. Aramouni, J. G. Touma, B. A. Tarboush, J. Zeaiter, M. N. Ahmad, Catalyst design for dry reforming of methane: Analysis review. *Renew. Sust. Energ. Rev.,* (2018), **82**, 2570-2585.

34. A. Tarasov *et al.*, Investigation of Coking During Dry Reforming of Methane by Means of Thermogravimetry. *Chem. Ing. Tech.,* (2014), **86**, 1916-1924.

35. C. Wang *et al.*, Coking and deactivation of a mesoporous Ni–CaO–ZrO2 catalyst in dry reforming of methane: A study under different feeding compositions. *Fuel,* (2015), **143**, 527-535.

36. G. Bozzano, F. Manenti, Efficient methanol synthesis: Perspectives, technologies and optimization strategies. *Prog. Energy Combust. Sci.,* (2016), **56**, 71-105.

37. J. Skrzypek, M. Lachowska, M. Grzesik, J. Słoczyński, P. Nowak, Thermodynamics and kinetics of low pressure methanol synthesis. *Chem. Eng. J. Biochem.,* (1995), **58**, 101-108.

38. F. Nestler *et al.*, Methanol Synthesis – Industrial Challenges within a Changing Raw Material Landscape. *Chem. Ing. Tech.,* (2018), **90**, 1409-1418.

39. R. Horn, R. Schlögl, Methane Activation by Heterogeneous Catalysis. *Catal. Lett.,* (2015), **145**, 23-39.

40. X. Liu, Y. Ryabenkova, M. Conte, Catalytic oxygen activation versus autoxidation for industrial applications: a physicochemical approach. *Phys. Chem. Chem. Phys.,* (2015), **17**, 715-731.

41. M. Sanchez-Sanchez, J. A. Lercher, in *Alkane Functionalization*. (2019), pp. 141-157.

42. A. E. Shilov, A. A. Shteinman, Activation of saturated hydrocarbons by metal complexes in solution. *Coord. Chem. Rev.,* (1977), **24**, 97-143.

43. A. Periana Roy *et al.*, Platinum Catalysts for the High-Yield Oxidation of Methane to a Methanol Derivative. *Science,* (1998), **280**, 560-564.

44. B. L. Conley *et al.*, Design and study of homogeneous catalysts for the selective, low temperature oxidation of hydrocarbons. *J. Mol. Catal. A Chem.,* (2006), **251**, 8-23.

45. M. C. Alvarez-Galvan *et al.*, Direct methane conversion routes to chemicals and fuels. *Catal. Today,* (2011), **171**, 15-23.

46. S. Sirajuddin, A. C. Rosenzweig, Enzymatic Oxidation of Methane. *Biochemistry,* (2015), **54**, 2283-2294.

47. H. J. Kim *et al.*, Biological conversion of methane to methanol through genetic reassembly of native catalytic domains. *Nat. Catal.,* (2019), **2**, 342-353.

48. M. A. Culpepper, G. E. Cutsail Iii, W. A. Gunderson, B. M. Hoffman, A. C. Rosenzweig, Identification of the Valence and Coordination Environment of the Particulate Methane Monooxygenase Copper Centers by Advanced EPR Characterization. *J. Am. Chem. Soc.,* (2014), **136**, 11767-11775.

49. S. I. Chan, K. H. C. Chen, S. S. F. Yu, C.-L. Chen, S. S. J. Kuo, Toward Delineating the Structure and Function of the Particulate Methane Monooxygenase from Methanotrophic Bacteria. *Biochemistry,* (2004), **43**, 4421-4430.

50. C. E. Tinberg, S. J. Lippard, Dioxygen Activation in Soluble Methane Monooxygenase. *Accounts of Chemical Research,* (2011), **44**, 280-288.

51. H. In Yeub *et al.*, Biocatalytic Conversion of Methane to Methanol as a Key Step for Development of Methane-Based Biorefineries. *J. Microbiol. Biotechnol.,* (2014), **24**, 1597-1605.

52. R. K. Srivastava, P. K. Sarangi, L. Bhatia, A. K. Singh, K. P. Shadangi, Conversion of methane to methanol: technologies and future challenges. *Biomass Convers. Biorefin.,* (2021).

53. T. J. Lawton, A. C. Rosenzweig, Methane-Oxidizing Enzymes: An Upstream Problem in Biological Gas-to-Liquids Conversion. *J. Am. Chem. Soc.,* (2016), **138**, 9327-9340.

54. V. I. Sobolev, K. A. Dubkov, O. V. Panna, G. I. Panov, Selective oxidation of methane to methanol on a FeZSM-5 surface. *Catal. Today,* (1995), **24**, 251-252.

55. K. A. Dubkov, N. S. Ovanesyan, A. A. Shteinman, E. V. Starokon, G. I. Panov, Evolution of Iron States and Formation of α-Sites upon Activation of FeZSM-5 Zeolites. *J. Catal.,* (2002), **207**, 341-352.

56. Y. K. Chow *et al.*, Investigating the influence of acid sites in continuous methane oxidation with N2O over Fe/MFI zeolites. *Catal. Sci. Technol.,* (2018), **8**, 154-163.

57. T. Yu *et al.*, Identifying key mononuclear Fe species for low-temperature methane oxidation. *Chem. Sci.,* (2021), **12**, 3152-3160.

58. B. E. R. Snyder *et al.*, The active site of low-temperature methane hydroxylation in iron-containing zeolites. *Nature,* (2016), **536**, 317-321.

59. M. H. Groothaert, J. A. van Bokhoven, A. A. Battiston, B. M. Weckhuysen, R. A. Schoonheydt, Bis(μ-oxo)dicopper in Cu-ZSM-5 and Its Role in the Decomposition of NO: A Combined in Situ XAFS, UV−Vis−Near-IR, and Kinetic Study. *J. Am. Chem. Soc.,* (2003), **125**, 7629-7640.

60. L. Tao, I. Lee, M. Sanchez-Sanchez, Cu oxo nanoclusters for direct oxidation of methane to methanol: formation, structure and catalytic performance. *Catal. Sci. Technol.,* (2020), **10**, 7124-7141.

61. M. A. Newton, A. J. Knorpp, V. L. Sushkevich, D. Palagin, J. A. van Bokhoven, Active sites and mechanisms in the direct conversion of methane to methanol using Cu in zeolitic hosts: a critical examination. *Chem. Soc. Rev,* (2020), **49**, 1449-1486.

62. A. F. Masters, T. Maschmeyer, Zeolites – From curiosity to cornerstone. *Microporous Mesoporous mater.,* (2011), **142**, 423-438.

63. A. D'amour, *Ann. Mines,* (1840), 191.

64. H. Eichhorn, *Ann. Phys. Chem.,* (1858), 126.

65. G. Friedel, *Bull. Soc. Fr. Mineral. Crystallogr. ,* (1896), 94.

66. R. Gans, *Jahrb. Preuß. geol. Landesanstalt 26,* (1905), 179.

67. R. M. Barrer, 33. Synthesis of a zeolitic mineral with chabazite-like sorptive properties. *Journal of the Chemical Society (Resumed),* (1948), 127-132.

68. Y. Li, J. Yu, Emerging applications of zeolites in catalysis, separation and host–guest assembly. *Nat. Rev. Mater.,* (2021), **6**, 1156-1174.

69. Y. Li, L. Li, J. Yu, Applications of Zeolites in Sustainable Chemistry. *Chem,* (2017), **3**, 928-949.

70. S. Wang, Y. Peng, Natural zeolites as effective adsorbents in water and wastewater treatment. *Chem. Eng. J.,* (2010), **156**, 11-24.

71. L. Bacakova, M. Vandrovcova, I. Kopova, I. Jirka, Applications of zeolites in biotechnology and medicine – a review. *Biomater. Sci.,* (2018), **6**, 974-989.

72. C. Baerlocher, L. B. McCusker, *Database of Zeolite Structures:* http://www.iza-structure.org/databases/.

73. J. Li, A. Corma, J. Yu, Synthesis of new zeolite structures. *Chem. Soc. Rev,* (2015), **44**, 7112-7127.

74. J. Weitkamp, Zeolites and catalysis. *Solid State Ion.,* (2000), **131**, 175-188.

75. W. Loewenstein, The distribution of aluminum in the tetrahedra of silicates and aluminates. *Am. Mineral.,* (1954), **39**, 92-96.

76. L. B. McCusker, C. Baerlocher, in *Studies in Surface Science and Catalysis,* H. van Bekkum, E. M. Flanigen, P. A. Jacobs, J. C. Jansen, Eds. (Elsevier, 2001), vol. 137, pp. 37-67.

77. M. Ravi, V. L. Sushkevich, J. A. van Bokhoven, Towards a better understanding of Lewis acidic aluminium in zeolites. *Nat. Mater.,* (2020), **19**, 1047-1056.

78. J. Dedecek, D. Kaucky, B. Wichterlova, O. Gonsiorova, Co2+ ions as probes of Al distribution in the framework of zeolites. ZSM-5 study. *Phys. Chem. Chem. Phys.,* (2002), **4**, 5406-5413.

79. B. Wichterlová, J. Dědeček, Z. Sobalík, A. Vondrová, K. Klier, On the Cu Site in ZSM-5 Active in Decomposition of NO: Luminescence, FTIR Study, and Redox Properties. *J. Catal.,* (1997), **169**, 194-202.

80. Y. Chai, W. Dai, G. Wu, N. Guan, L. Li, Confinement in a Zeolite and Zeolite Catalysis. *Accounts of Chemical Research,* (2021), **54**, 2894-2904.

81. G. Brezicki, J. D. Kammert, T. B. Gunnoe, C. Paolucci, R. J. Davis, Insights into the Speciation of Cu in the Cu-H-Mordenite Catalyst for the Oxidation of Methane to Methanol. *ACS Catal.,* (2019), **9**, 5308-5319.

82. M. H. Groothaert, P. J. Smeets, B. F. Sels, P. A. Jacobs, R. A. Schoonheydt, Selective Oxidation of Methane by the Bis(μ-oxo)dicopper Core Stabilized on ZSM-5 and Mordenite Zeolites. *J. Am. Chem. Soc.,* (2005), **127**, 1394-1395.

83. E. M. C. Alayon, M. Nachtegaal, A. Bodi, J. A. van Bokhoven, Reaction conditions of methane-to-methanol conversion affect the structure of active copper sites. *ACS Catal.,* (2014), **4**, 16-22.

84. E. M. C. Alayon, M. Nachtegaal, E. Kleymenov, J. A. van Bokhoven, Determination of the electronic and geometric structure of Cu sites during methane conversion over Cu-MOR with X-ray absorption spectroscopy. *Microporous Mesoporous mater.,* (2013), **166**, 131-136.

85. E. M. Alayon, M. Nachtegaal, M. Ranocchiari, J. A. van Bokhoven, Catalytic conversion of methane to methanol over Cu–mordenite. *ChemComm,* (2012), **48**, 404-406.

86. E. M. C. Alayon, M. Nachtegaal, A. Bodi, M. Ranocchiari, J. A. van Bokhoven, Bis(μ-oxo) versus mono(μ-oxo)dicopper cores in a zeolite for converting methane to methanol: an in situ XAS and DFT investigation. *Phys. Chem. Chem. Phys.,* (2015), **17**, 7681-7693.

87. S. Grundner, W. Luo, M. Sanchez-Sanchez, J. A. Lercher, Synthesis of single-site copper catalysts for methane partial oxidation. *ChemComm,* (2016), **52**, 2553-2556.

88. S. Grundner *et al.*, Single-site trinuclear copper oxygen clusters in mordenite for selective conversion of methane to methanol. *Nat. Comm.,* (2015), **6**, 7546.

89. T. Ikuno *et al.*, Formation of Active Cu-oxo Clusters for Methane Oxidation in Cu-Exchanged Mordenite. *J. Phys. Chem. C,* (2019), **123**, 8759-8769.

90. G. Brezicki, J. Zheng, C. Paolucci, R. Schlögl, R. J. Davis, Effect of the Co-cation on Cu Speciation in Cu-Exchanged Mordenite and ZSM-5 Catalysts for the Oxidation of Methane to Methanol. *ACS Catal.,* (2021), **11**, 4973-4987.

91. I. Lee *et al.*, Activity of Cu–Al–Oxo Extra-Framework Clusters for Selective Methane Oxidation on Cu-Exchanged Zeolites. *JACS Au,* (2021), **1**, 1412-1421.

92. D. K. Pappas *et al.*, Understanding and Optimizing the Performance of Cu-FER for The Direct CH4 to CH3OH Conversion. *ChemCatChem,* (2019), **11**, 621-627.

93. M. Dyballa *et al.*, On How Copper Mordenite Properties Govern the Framework Stability and Activity in the Methane-to-Methanol Conversion. *ACS Catal.,* (2019), **9**, 365-375.

94. D. K. Pappas *et al.*, The Nuclearity of the Active Site for Methane to Methanol Conversion in Cu-Mordenite: A Quantitative Assessment. *J. Am. Chem. Soc.,* (2018), **140**, 15270-15278.

95. D. K. Pappas *et al.*, Methane to Methanol: Structure–Activity Relationships for Cu-CHA. *J. Am. Chem. Soc.,* (2017), **139**, 14961-14975.

96. D. K. Pappas *et al.*, Influence of Cu-speciation in mordenite on direct methane to methanol conversion: Multi-Technique characterization and comparison with NH3 selective catalytic reduction of NOx. *Catal. Today,* (2021), **369**, 105-111.

97. E. Borfecchia *et al.*, Evolution of active sites during selective oxidation of methane to methanol over Cu-CHA and Cu-MOR zeolites as monitored by operando XAS. *Catal. Today,* (2019), **333**, 17-27.

98. J. S. Woertink *et al.*, A [Cu2O]2+ core in Cu-ZSM-5, the active site in the oxidation of methane to methanol. *Proc. Natl. Acad. Sci.,* (2009), **106**, 18908.

99. V. L. Sushkevich, D. Palagin, J. A. van Bokhoven, The Effect of the Active-Site Structure on the Activity of Copper Mordenite in the Aerobic and Anaerobic Conversion of Methane into Methanol. *Angew. Chem., Int. Ed.,* (2018), **57**, 8906-8910.

100. A. J. Knorpp, A. B. Pinar, M. A. Newton, V. L. Sushkevich, J. A. van Bokhoven, Copper-Exchanged Omega (MAZ) Zeolite: Copper-concentration Dependent Active Sites and its Unprecedented Methane to Methanol Conversion. *ChemCatChem,* (2018), **10**, 5593-5596.

101. P. J. Smeets, M. H. Groothaert, R. A. Schoonheydt, Cu based zeolites: A UV–vis study of the active site in the selective methane oxidation at low temperatures. *Catal. Today,* (2005), **110**, 303-309.

102. P. Vanelderen *et al.*, Spectroscopic Definition of the Copper Active Sites in Mordenite: Selective Methane Oxidation. *J. Am. Chem. Soc.,* (2015), **137**, 6383-6392.

103. P. Vanelderen *et al.*, Spectroscopy and Redox Chemistry of Copper in Mordenite. *ChemPhysChem,* (2014), **15**, 91-99.

104. Z.-J. Zhao, A. Kulkarni, L. Vilella, J. K. Nørskov, F. Studt, Theoretical Insights into the Selective Oxidation of Methane to Methanol in Copper-Exchanged Mordenite. *ACS Catal.,* (2016), **6**, 3760-3766.

105. A. R. Kulkarni, Z.-J. Zhao, S. Siahrostami, J. K. Nørskov, F. Studt, Monocopper Active Site for Partial Methane Oxidation in Cu-Exchanged 8MR Zeolites. *ACS Catal.,* (2016), **6**, 6531-6536.

106. V. L. Sushkevich, M. Artsiusheuski, D. Klose, G. Jeschke, J. A. van Bokhoven, Identification of Kinetic and Spectroscopic Signatures of Copper Sites for Direct Oxidation of Methane to Methanol. *Angew. Chem., Int. Ed.,* (2021), **60**, 15944-15953.

107. A. J. Knorpp *et al.*, Paired Copper Monomers in Zeolite Omega: The Active Site for Methane-to-Methanol Conversion. *Angew. Chem., Int. Ed.,* (2021), **60**, 5854-5858.

108. D. Palagin, A. J. Knorpp, A. B. Pinar, M. Ranocchiari, J. A. van Bokhoven, Assessing the relative stability of copper oxide clusters as active sites of a CuMOR zeolite for methane to methanol conversion: size matters? *Nanoscale,* (2017), **9**, 1144-1153.

109. G. Li, E. A. Pidko, The Nature and Catalytic Function of Cation Sites in Zeolites: a Computational Perspective. *ChemCatChem,* (2019), **11**, 134-156.

110. G. Li *et al.*, Stability and reactivity of copper oxo-clusters in ZSM-5 zeolite for selective methane oxidation to methanol. *J. Catal.,* (2016), **338**, 305-312.

111. A. R. Kulkarni, Z.-J. Zhao, S. Siahrostami, J. K. Nørskov, F. Studt, Cation-exchanged zeolites for the selective oxidation of methane to methanol. *Catal. Sci. Technol.,* (2018), **8**, 114-123.

112. J. Zheng *et al.*, Importance of Methane Chemical Potential for Its Conversion to Methanol on Cu-Exchanged Mordenite. *Chem. Eur. J.,* (2020), **26**, 7563-7567.

113. B. E. R. Snyder, P. Vanelderen, R. A. Schoonheydt, B. F. Sels, E. I. Solomon, Second-Sphere Effects on Methane Hydroxylation in Cu-Zeolites. *J. Am. Chem. Soc.,* (2018), **140**, 9236-9243.

114. M. H. Mahyuddin, A. Staykov, Y. Shiota, M. Miyanishi, K. Yoshizawa, Roles of Zeolite Confinement and Cu–O–Cu Angle on the Direct Conversion of Methane to Methanol by [Cu2(μ-O)]2+-Exchanged AEI, CHA, AFX, and MFI Zeolites. *ACS Catal.,* (2017), **7**, 3741-3751.

115. B. Ipek *et al.*, Formation of [Cu2O2]2+ and [Cu2O]2+ toward C–H Bond Activation in Cu-SSZ-13 and Cu-SSZ-39. *ACS Catal.,* (2017), **7**, 4291-4303.

116. W. Malzer, C. Schlesiger, B. Kanngießer, A century of laboratory X-ray absorption spectroscopy – A review and an optimistic outlook. *Spectrochim. Acta B,* (2021), **177**, 106101.

117. A. Gaur, B. D. Shrivastava, Speciation using X-ray absorption fine structure (XAFS). *Rev. J. Chem.,* (2015), **5**, 361-398.

118. A. Takahara, Y. Higaki, T. Hirai, R. Ishige, Application of Synchrotron Radiation X-ray Scattering and Spectroscopy to Soft Matter. *Polymers,* (2020), **12**.

119. P. Zimmermann *et al.*, Modern X-ray spectroscopy: XAS and XES in the laboratory. *Coord. Chem. Rev.,* (2020), **423**, 213466.

120. M. Newville, Fundamentals of XAFS. *Rev. Mineral. Geochem.,* (2014), **78**, 33-74.

121. J. J. Rehr, A. L. Ankudinov, Progress in the theory and interpretation of XANES. *Coord. Chem. Rev.,* (2005), **249**, 131-140.

122. J. G. Mesu, A. M. Beale, F. M. F. de Groot, B. M. Weckhuysen, Probing the Influence of X-rays on Aqueous Copper Solutions Using Time-Resolved in Situ Combined Video/X-ray Absorption Near-Edge/Ultraviolet−Visible Spectroscopy. *J. Phys. Chem. B,* (2006), **110**, 17671-17677.

123. J. E. Penner-Hahn, X-ray absorption spectroscopy in coordination chemistry. *Coord. Chem. Rev.,* (1999), **190-192**, 1101-1123.

124. J. Yano, V. K. Yachandra, X-ray absorption spectroscopy. *Photosynth. Res.,* (2009), **102**, 241.

125. C. H. M. van Oversteeg, H. Q. Doan, F. M. F. de Groot, T. Cuk, In situ X-ray absorption spectroscopy of transition metal based water oxidation catalysts. *Chem. Soc. Rev,* (2017), **46**, 102-125.

126. G. S. Henderson, F. M. F. de Groot, B. J. A. Moulton, X-ray Absorption Near-Edge Structure (XANES) Spectroscopy. *Rev. Mineral. Geochem.,* (2014), **78**, 75-138.

127. R. K. Hocking, E. I. Solomon, in *Molecular Electronic Structures of Transition Metal Complexes I,* D. M. P. Mingos, P. Day, J. P. Dahl, Eds. (Springer Berlin Heidelberg, Berlin, Heidelberg, 2012), pp. 155-184.

128. G. Cressey, C. M. B. Henderson, G. van der Laan, Use of L-edge X-ray absorption spectroscopy to characterize multiple valence states of 3d transition metals; a new probe for mineralogical and geochemical research. *Phys. Chem. Miner.,* (1993), **20**, 111-119.

129. M. L. Baker *et al.*, K- and L-edge X-ray absorption spectroscopy (XAS) and resonant inelastic X-ray scattering (RIXS) determination of differential orbital covalency (DOC) of transition metal sites. *Coord. Chem. Rev.,* (2017), **345**, 182-208.

130. J. M. Kasper, T. F. Stetina, A. J. Jenkins, X. Li, Ab initio methods for L-edge x-ray absorption spectroscopy. *Chem. Phys. Rev.,* (2020), **1**, 011304.

131. E. Aprà *et al.*, NWChem: Past, present, and future. *J. Chem. Phys.,* (2020), **152**, 184102.

132. A. Vjunov *et al.*, Tracking the Chemical Transformations at the Brønsted Acid Site upon Water-Induced Deprotonation in a Zeolite Pore. *Chem. Mater.,* (2017), **29**, 9030-9042.

133. A. Vjunov *et al.*, Quantitatively Probing the Al Distribution in Zeolites. *J. Am. Chem. Soc.,* (2014), **136**, 8296-8306.

134. Y. Zhang, S. Mukamel, M. Khalil, N. Govind, Simulating Valence-to-Core X-ray Emission Spectroscopy of Transition Metal Complexes with Time-Dependent Density Functional Theory. *J. Chem. Theory Comput.,* (2015), **11**, 5804-5809.

135. Y. Zhang, U. Bergmann, R. Schoenlein, M. Khalil, N. Govind, Double core hole valence-to-core x-ray emission spectroscopy: A theoretical exploration using time-dependent density functional theory. *J. Chem. Phys.,* (2019), **151**, 144114.

136. M. Newville, EXAFS analysis using FEFF and FEFFIT. *J. Synchroton Radiat.,* (2001), **8**, 96-100.

137. B. Ravel, M. Newville, ATHENA, ARTEMIS, HEPHAESTUS: data analysis for X-ray absorption spectroscopy using IFEFFIT. *J. Synchroton Radiat.,* (2005), **12**, 537-541.

138. J. L. Fulton, S. M. Kathmann, G. K. Schenter, M. Balasubramanian, Hydrated Structure of Ag(I) Ion from Symmetry-Dependent, K- and L-Edge XAFS Multiple Scattering and Molecular Dynamics Simulations. *J. Phys. Chem. A,* (2009), **113**, 13976-13984.

139. R. Atta-Fynn, E. J. Bylaska, G. K. Schenter, W. A. de Jong, Hydration Shell Structure and Dynamics of Curium(III) in Aqueous Solution: First Principles and Empirical Studies. *J. Phys. Chem. A,* (2011), **115**, 4665-4677.

140. S. Bogatko *et al.*, The Aqueous Ca2+ System, in Comparison with Zn2+, Fe3 +, and Al3 +: An Ab Initio Molecular Dynamics Study. *Chem. Eur. J.,* (2013), **19**, 3047-3060.

141. G. K. Schenter, J. L. Fulton, in *XAFS Techniques for Catalysts, Nanomaterials, and Surfaces,* Y. Iwasawa, K. Asakura, M. Tada, Eds. (Springer International Publishing, Cham, 2017), pp. 251-270.

142. L. X. Dang, G. K. Schenter, V.-A. Glezakou, J. L. Fulton, Molecular Simulation Analysis and X-ray Absorption Measurement of Ca2+, K+ and Cl- Ions in Solution. *J. Phys. Chem. B,* (2006), **110**, 23644-23654.

143. S. Pérez-Conesa, J. M. Martínez, R. R. Pappalardo, E. S. Marcos, Combining EXAFS and Computer Simulations to Refine the Structural Description of Actinyls in Water. *Molecules,* (2020), **25**, 5250.

144. J. J. Rehr, R. C. Albers, Theoretical approaches to x-ray absorption fine structure. *Rev. Mod. Phys,* (2000), **72**, 621-654.

145. B. J. Palmer, D. M. Pfund, J. L. Fulton, Direct Modeling of EXAFS Spectra from Molecular Dynamics Simulations. *J. Phys. Chem.,* (1996), **100**, 13393-13398.

146. A. Kuzmin, J. Timoshenko, A. Kalinko, I. Jonane, A. Anspoks, Treatment of disorder effects in X-ray absorption spectra beyond the conventional approach. *Radiat. Phys. Chem.,* (2020), **175**.

147. J. Timoshenko, Z. Duan, G. Henkelman, R. M. Crooks, A. I. Frenkel, Solving the Structure and Dynamics of Metal Nanoparticles by Combining X-Ray Absorption Fine Structure Spectroscopy and Atomistic Structure Simulations. *Annu. Rev. Anal. Chem.,* (2019), **12**, 501-522.

# 2 Critical Assessment of Oxidation States of Cu present in MOR

## 2.1 Abstract

Cu-oxo clusters hosted in zeolites are able to selectively oxidize $CH_4$ to $CH_3OH$ via a three-step process. The analysis of oxidations states of Cu-species present in Cu-MOR after oxygen treatment and autoreduction by FT-IR with CO and NO probe molecules show that a significant amount of $Cu^{2+}$ is present after autoreduction. Application of high-brilliance XAS for the on Cu-MOR demonstrate undesired X-ray induced reduction of $Cu^{2+}$ in MOR. Intense X-ray doses during He-treatment can trigger the reduction of hydrated $Cu^{2+}$species through radiolysis at low temperatures. Analysis of oxygen activated Cu-MOR also revealed the reducing effect of X-rays on Cu-oxo species in non-reducing conditions. Enhanced kinetic of $Cu^{2+}$ reduction of Cu-oxo species during $CH_4$ reaction is also observed to take place upon X-ray exposure. Careful consideration such as short beam exposure and change of beam spots helps to avoid and detect X-ray induced damage on the samples.

## 2.2 Introduction

Since the first report by Groothaert et al. of selective oxidation of methane to methanol, extensive studies have been employed to elucidate the active sites of Cu-oxo clusters hosted in Cu-zeolites.[1] The stoichiometric three-step process of the conversion of methane to methanol allows us to thoroughly analyze the Cu-MOR during $O_2$ activated, $CH_4$ reacted, or steam treatment.[1-19] Characterization techniques such as FT-IR with probe molecules such as CO,[20-23] NO[17, 24-27], and Cu K-edge XAS[2-11, 15, 16, 28] have become established tools for the analysis of Cu-exchanged zeolitic materials.[8, 14, 17, 29-35] CO is known to interact with $Cu^+$ cations in zeolites and can form $Cu(CO)^+$, $Cu(CO)^{2+}$ and $Cu(CO)_3^+$.[8, 21-23, 29, 31-33, 36] In contrast to CO, a NO molecule has an additional electron, which occupies the π*-orbital, allowing us to probe the $Cu^{2+}$ and $Cu^+$ states with higher sensitivity.[37, 38]

In situ XANES measurements is an established method to probe the oxidation state of Cu during activation and help to understand the oxygen activation procedure where Cu-oxo cluster with $Cu^{2+}$ character are formed.[2, 4-11, 15] Furthermore, it shed light on the reduction of Cu-oxo cluster from $Cu^{2+}$ to $Cu^+$ upon methane reaction. The constant development of synchrotron generated X-rays has brought great opportunities for the investigation of electronic properties and geometries of nanocrystalline materials and other research fields such as biology, biomedical applications, homogeneous catalysis, electrocatalysis, etc..[18, 39-46] However, the high X-ray doses employed during XANES measurements might cause beam induced damage on the Cu-zeolites and highly influence structure related quantitative and kinetic behavior of such materials.[18] Through comparison of FT-IR and Cu K-edge XANES analysis we will crosscheck the oxidation states of Cu-species in Cu-MOR.

## 2.3 Experimental Methods

### *2.3.1 Preparation of Cu-MOR Samples*

Commercial $NH_4$-MOR (Si/Al = 10 and 11) was purchased from Clariant, and the corresponding H-form was obtained after calcination in synthetic air (100 mL/min) at 550°C (10K/min) for 6 h.

Cu-MOR samples were prepared by aqueous ion exchange of H-MOR with $Cu^{2+}$ under controlled conditions to avoid precipitation of unwanted CuO and $Cu(OH)_2$ nanoparticles. $Cu^{2+}$-exchange was carried out at ambient temperature with 5 g zeolites in 300 mL of a 0.001-0.01 M aqueous solution of $Cu(CH_3COO)_2$ (Sigma Aldrich, 99,99%) for 20 h. The pH of the solution was kept to 5.5-6.0 during the Cu-exchange. The sample was separated from the mother liquor by centrifugation and rinsed four times with double deionized water with an intervening centrifugation step between each rinse cycle. Obtained samples were dried at 110 °C for 24 h. Cu-zeolite samples were all calcined in synthetic air at 550 °C for 2 h before IR and XAS measurement. Si, Al, Na, and Cu contents were measured by atomic absorption spectroscopy (AAS) on a UNICAM 939 AA spectrometer after dissolution in boiling hydrofluoric acid.

### *2.3.2 Testing of Activity for Selective Oxidation of Methane*

The activity of the Cu-MOR samples for the selective $CH_4$ oxidation to methanol was tested under atmospheric pressure in a stainless-steel plug flow reactor with a 4 mm inner diameter. In a typical reaction, 50 mg of Cu-MOR (250-400 µm) was first activated for 1 h in $O_2$ at 500 °C, cooled down to 200 °C, and then flushed with He. In the next step, 90% $CH_4$ in He was flown over the sample for 4 h. The samples were then cooled to 135 °C in He and steam-assisted product desorption was performed with 50 % $H_2O$ in He. Reaction products were identified and quantified with online mass spectroscopy by monitoring the m/z signals of 31, 44, and 46 for $CH_3OH$, $CO_2$, and $(CH_3)_2O$ respectively. $(CH_3)_2O$ was considered as a condensation of two $CH_3OH$ molecules and therefore considered as two $CH_3OH$ equivalents. The sum of all detected products was considered as the total yield.

### *2.3.3 Cu K-edge HERFD XANES*

HERFD XANES measurements were carried on beamline P64 at PETRA III of DESY (Hamburg, Germany). Approximately 10 mg of the sample was in a quartz capillary reactor with an outer diameter of 1 mm and 0.02 mm wall thickness. The packed sample was then mounted on top of a gas blower for controlled heating and the sample was thermally activated in 10% $O_2$ in He at 450 °C for 1 h with a heating rate of 10 K/min and subsequently cooled down to r.t.. Measurements were performed before and after activation. $CH_4$-reaction measurements were performed at 200°C with 10% $CH_4$ in He. The beam spot was constantly changed to avoid extensive radiation damage. The incident photon energy was controlled by a double-crystal Si(111) monochromator and a von Hamos-type X-ray emission spectrometer with eight Si(444) mirrors were used to record the spectra. Energy calibration was performed by recording the elastic scattering at 8015 eV, 8027 eV, 8047 eV, and 8060 eV. The gas flow over the samples was introduced by Bronkhorst mass-flow controllers and the gases were further dried by using Supelco 5A Moisture trap.

### *2.3.4 Conventional Cu K-edge XANES*

Cu K-edge XANES measurements were carried out on beamline P65 at PETRA III of DESY in Hamburg, Germany. Approximately 10 mg of the sample was in a quartz capillary reactor with an outer diameter of. 1 mm and 0.02 mm wall thickness. The packed sample was then mounted on top of a gas blower for controlled heating and the sample was thermally activated in 10% $O_2$ in He at 500 °C or in pure He for 1 h with a heating rate of 10 K/min and subsequently cooled down to r.t.. Methane reactions were performed at 200 °C with 10% $CH_4$ in He. The beam spot was constantly changed to avoid extensive radiation damage. A double-crystal Si(111) monochromator was used to control the incident photon energy, and the spectra were recorded with ionization chamber detectors in the transmission mode. The gas flow over the samples was introduced by Bronkhorst mass-flow controllers and the gases were further dried by using Supelco 5A Moisture trap. ATHENA software was used during the background processing. XANES normalization follows the standard protocol used within the Athena software.[47]

### *2.3.5 In Situ FT-IR Spectroscopy*

The samples for IR spectroscopy were pressed as self-supporting wafers with a density of ca. 10 mg/cm$^2$ and activated in vacuum (1.0 x 10$^{-7}$ mbar) at 450 °C with a heating rate of 10 K/min for 1 h. After that, 200 mbar of synthetic air was introduced and kept in the IR cell for another 1 h for oxidative treatment of the samples. Then, the samples were allowed to cool down naturally to 40 °C before the synthetic air was evacuated again for measurement. For the measurements of CO and NO adsorption, the samples were fully cooled down with liquid nitrogen and the IR spectra were recorded after the dosage of NO and CO. The measurements were recorded on a Vertex 70 spectrometer (Bruker Optics) with a resolution of 4 cm$^{-1}$.

## 2.4 Results and Discussion

### *2.4.1 Activity of Cu-MOR*

The activity of the Cu-MOR series has been measured with the usual three-stage reaction consisting of a high temperature activation at 500 °C in oxygen for 1h, $CH_4$ reaction at 200 °C for 4h, and steam treatment for product desorption at 135 °C with 50 % $H_2O$ in He.[1, 2, 7-11, 15, 16, 19, 28, 48-50] As a mean of comparison for different Cu-loadings we define the Cu efficiency ($Cu_{eff}$) as the ratio of activated $CH_4$ over the total number of Cu present in the MOR. The origin of the unusually high activity of this Cu-MOR series, which has a $Cu_{eff}$ = 0.58, will be discussed in the next chapter.

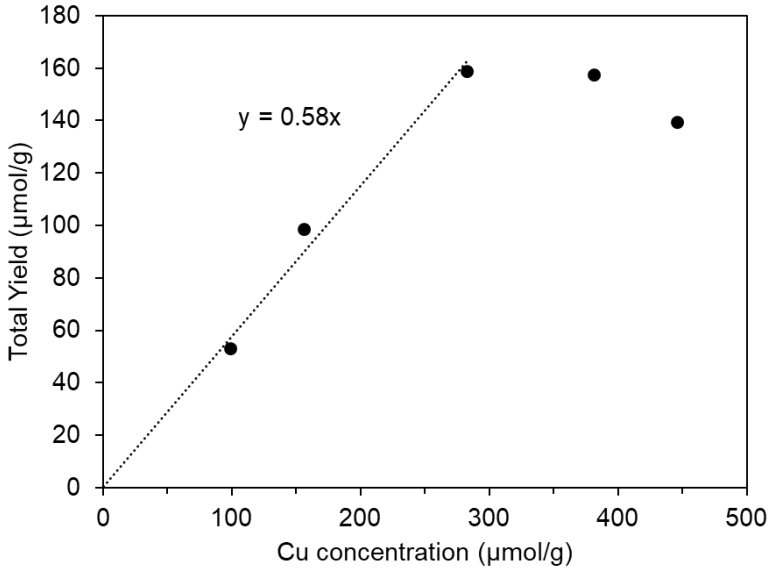


**Figure 1** Yield of $CH_4$ oxidation on the Cu-MOR catalyst. $Cu_{eff}$ as y = $Cu_{eff}$ x. The activity tests were repeated 3 times on each Cu-loading and averaged values are reported.

### *2.4.2 FT-IR of CO and NO Adsorption at Liquid Nitrogen Temperature*

In order, to probe $Cu^+$ species in Cu-MOR with CO or NO molecules, the samples are reduced by autoreduction under dynamic vacuum. This process occurs in inert conditions such as vacuum, He-atmosphere, and high temperatures.[9-11, 13-15, 32, 34, 51-56] Temperature plays a major role in the adsorption of CO and NO on Cu hosted in zeolites. In order to observe the formation of $Cu(CO)_3^+$ complex[22, 33, 36, 57] and to avoid NO decomposition,[38, 57] the measurements have to be performed at liquid-nitrogen temperatures. Figure 1 shows at 1 x $10^{-1}$ mbar a characteristic IR-band at 2158 $cm^{-1}$, corresponding to monocarbonylic C-O stretching vibration adsorbed on $Cu^+$ of an autoreduced Cu-MOR.[8, 29]

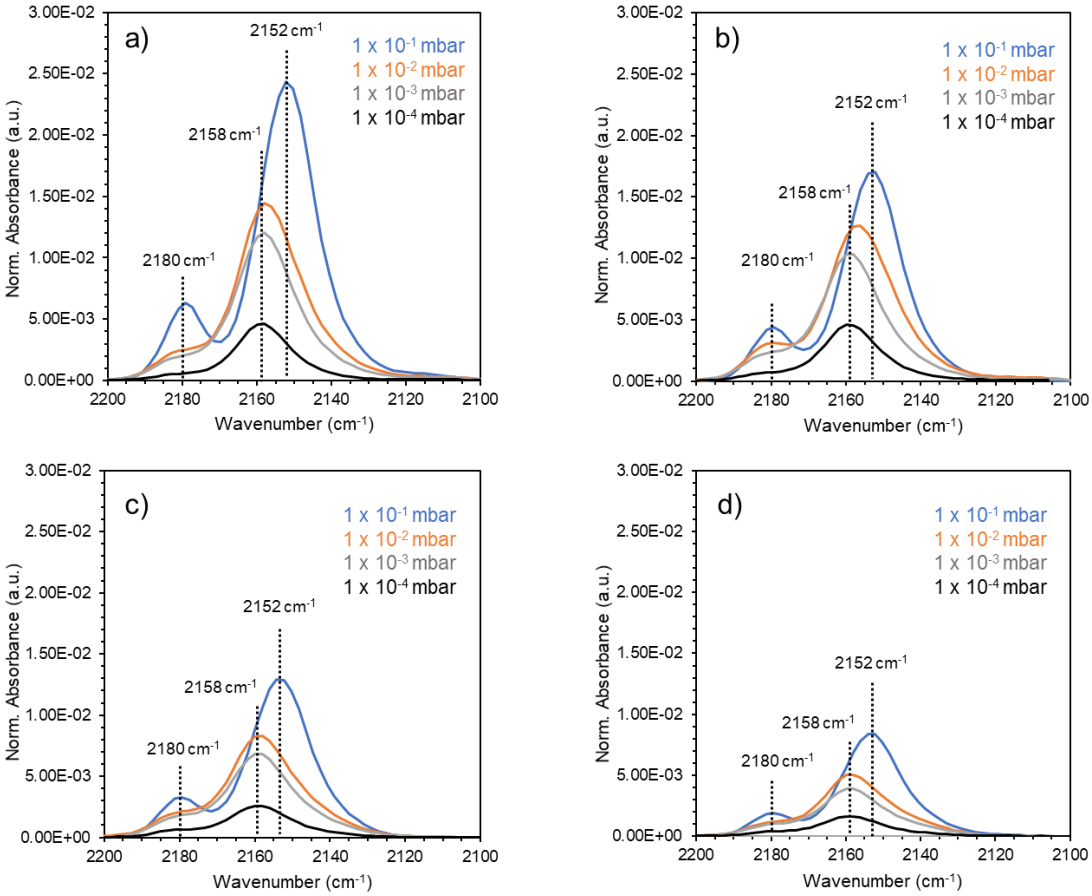


**Figure 1**. FT-IR of CO adsorption of autoreduced Cu-MOR series ($p_{CO}$ = 1 x $10^{-4}$ – $10^{-1}$ mbar) at liquid nitrogen temperature with a) c(Cu) = 434 µmol/g, b) c(Cu) = 283 µmol/g, c) c(Cu) = 156 µmol/g and d) c(Cu) = 99 µmol/g. The samples were autoreduced at 450 °C for 1 h in vacuum before CO adsorption.

With increasing $p_{CO}$, the main intensity of 2158 $cm^{-1}$ shifts gradually to 2152 $cm^{-1}$. This behavior is attributed to the formation of monocarbonilic $Cu(CO)^{+}$ complex to a dicarbonilic $Cu(CO)^{2+}$, resulting in symmetric and asymmetric stretching modes at 2180 and 2150 $cm^{-1}$.[8, 29] However, a weak shoulder at ca. 2180 $cm^{-1}$ is also visible at low $p_{CO}$, indicating that a small fraction of dicarbonilic species is formed simultaneously with monocarbonilic $Cu^{+}$ species at $p_{CO}$ = 1 x $10^{-}$4 mbar. The Cu-MOR sample with 434 µmol/g shows the most intense peaks, whereas the sample with 99 µmol/g has less intensities in the C-O stretching region. Overall, the Intensities of C-O stretching vibration correlate with the amount of CO that can interact with $Cu^{+}$ and therefore give information on the relative amount of $Cu^{+}$ species (Figure 1). $Cu(CO)_3^{+}$ species in MOR, which show characteristic vibrations at 2190, 2165 and 2145 $cm^{-1}$ are not visible.[29] This indicates that the probed $Cu^{+}$-species are all in the confined environment of the 8 MR side pockets of MOR. Only $Cu^{+}$ species located in the 12 MR main channel of MOR can form $Cu(CO)_3^{+}$ species.[29] $Cu^{+}$ species are known to be very mobile at temperature temperatures above 400 °C, which is a crucial part for the redistribution and formation of active Cu-oxo cluster preferably located in the 8 MR side pockets of MOR.[2, 15, 28]

To access potential residues of $Cu^{2+}$, we employ the use of NO molecules to probe $Cu^{2+}$ and $Cu^{+}$ species in $O_2$ activated and autoreduced samples. Figure 2 represents the spectra of NO adsorbed at p = 0.01mbar at liquid nitrogen temperature. The characteristic vibrations of a NO adsorbed on $Cu^{2+}$ can be observed in the region from 1900 ~ 2000 $cm^{-1}$, while the vibration corresponding to $Cu^{+}$-NO are well separated in the range 1700-1850 $cm^{-1}$ (Figure 2, Figure S1). [14, 24-27, 30, 31, 37] Oxygen-activated Cu-MOR series shows several show a very prominent band corresponding to $Cu^{2+}$-NO vibration at ca. 1907 $cm^{-1}$ and smaller bands at 1955 $cm^{-1}$ and 1974 $cm^{-1}$. Overall, the intensities of $Cu^{2+}$-NO bands correlate with increasing Cu-concentration. Interestingly, Cu-MOR with 380 µmol/g does not show an increase of the main peak at 1907 $cm^{-1}$, but rather an increase of the bands at 1955 and 1974 $cm^{-1}$. Sushkevich et al. was reporting that the vibrations of NO interacting with $Cu^{2+}$ are giving information on the nuclearity of Cu-oxo cluster, where bands at around ~ 1900 $cm^{-1}$ are corresponding to monomeric $[Cu(OH)]^{+}$ species, active for the selective oxidation of methane, and bands at higher wavenumber ~ 1953 and 1998 $cm^{-1}$ are corresponding to Cu-oxo species with higher nuclearity.[14, 30, 37, 58]

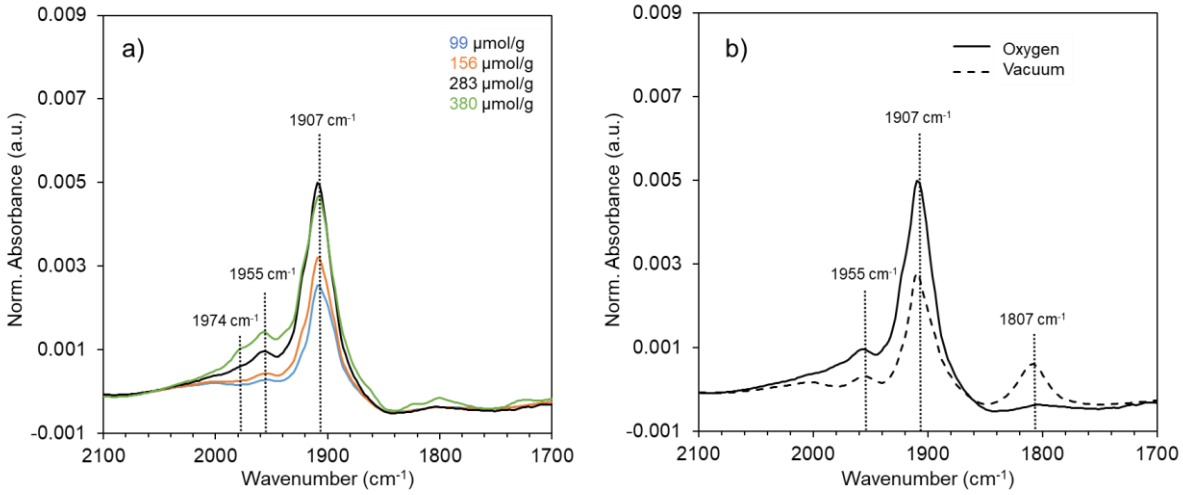


**Figure 2** FT-IR spectra of adsorbed NO ($p_{NO}$ = 0.01 mbar) at liquid nitrogen temperature on a) oxygen-activated Cu-MOR series with 99,156, 283, and 380 µmol/g. b) shows the comparison of oxygen and vacuum- activate Cu-MOR with 283 µmol/g.

But the analyzed samples, in the mentioned study, show signs of $Cu^+$ after oxygen treatment, which occur since the oxidized samples are treated in vacuum at 400 °C for 1 h after the oxidation procedure and therefore are partially autoreduced.

The attribution of monomeric $[Cu(OH)]^+$ species as the active site for the selective oxidation is in contradiction with earlier reports, where the active site in Cu-MOR has been solely attributed to a dicopper active site.[3, 6] The formation of $[Cu(OH)]^+$ species[14, 30, 37, 58] or in case of Cu-MAZ a pair of $[Cu(OH)]^+$ species,[59] should lead according to the condensation mechanism at high temperature to a $[Cu\text{-}(\mu\text{-}O)\text{-}Cu]^{2+}$ rather than a $[Cu\text{-}(OH)_2\text{-}Cu]^{2+}$ cluster.[10, 12, 15] Remarkably, all reports on the synthesis of the analyzed Cu-zeolites by this group are not prepared by pH-controlled aqueous Cu ion exchange, which should lead to inactive nano-sized agglomeration of CuO [3-6, 14, 17, 30, 35, 58, 59] and are partially overexchanged with CuO agglomerations on the zeolite after oxygen activation[60]. The mentioned conditions add unwanted heterogeneity to the Cu-speciation and inactive species to the prepared and analyzed Cu-zeolite samples. Grundner et al. showed the importance of pH controlled aqueous ion exchange, to avoid the formation of undesirable CuO nano-sized particles.[48] Optimized aqueous Cu-exchange conditions with pH control on zeolites are also followed up by other groups.[8, 10-13, 50]

Hadjiianov et al. assigned the presence of the higher frequency bands to an increase of the oxidation state of Cu whereupon adsorption of a NO molecule on $[Cu\text{-}O\text{-}Cu]^{2+}$, a disproportion from formally two $Cu^{2+}$ to a $Cu^{3+}$ and $Cu^{+}$ occurs.[25] This would mean that $O_2$-activated Cu-MOR with a $[Cu\text{-}O\text{-}Cu]^{2+}$ show the interaction of NO with $Cu^{2+}$ and $Cu^{+}$. However, the interaction of $Cu^{+}$ with NO can only be seen at ca 1807 $cm^{-1}$ in vacuum Cu-MOR samples (Figure 2a, Figure S1). A full reduction of $Cu^{2+}$ present in Cu-MOR is not achievable through autoreduction in vacuum. Vacuum treatment of Cu-MOR does not lead to full autoreduction of $Cu^{2+}$ species, therefore making the quantification of $Cu^{2+}/Cu^{+}$ species and assessment on the nuclearity of Cu oxo-cluster difficult by IR spectroscopy through NO probe molecules. In general, we attribute the vibration in general to NO interacting with $Cu^{2+}$ without attribution to nuclearities of Cu-oxo species in Cu-MOR. These results are in opposition to autoreduction processes of thermal He treatment observed by Cu K-edge XANES, where a reduction of the majority of $Cu^{2+}$ to $Cu^{+}$ takes place.[10, 12, 14] The question on the nuclearity of Cu-oxo species of the Cu-MOR series will be discussed in chapter 3.

### *2.4.3 Formation and Stability of Cu-Oxo Cluster Under X-Ray exposure*

In situ Cu K-edge XAS is an important technique for the determination of oxidation states and nuclearity of Cu-oxo clusters in Cu-zeolites.[2, 3, 9, 10, 12, 15, 49] High temperature oxygen treatment of Cu-MOR, observed in XANES, leads to a decrease of the White line due to dehydration of the material and indicating the gradual formation of Cu-oxo cluster (Figure 3).[3, 5, 6, 8, 10, 12, 15]

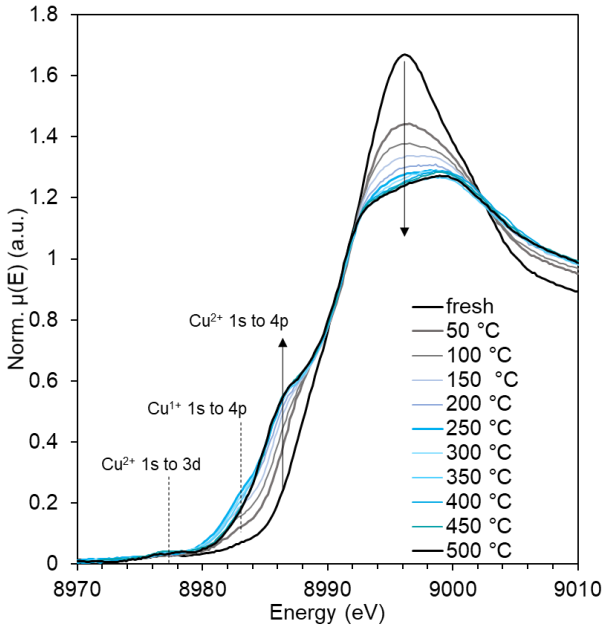


**Figure 3** *In situ* Cu K-edge XANES of Cu-MOR with 283 µmol/g during $O_2$ activation.

The small pre-edge feature at ca. 8977 eV corresponds to the weak dipole forbidden 1s to 3d transition of $Cu^{2+}$, confirming the $Cu^{2+}$character of the Cu-MOR during the oxygen activation (Figure 3). In addition, the formation of the Cu-oxo cluster can be observed upon the increase of the shoulder at ca 8986 eV, associated with the dipole allowed shake down transition 1s to 4p of $Cu^{2+}$.

During oxygen treatment, the reduction of $Cu^{2+}$ to $Cu^{+}$ occurs parallel to the formation of Cu-oxo cluster. In the temperature range of 50 °C < $T_{Cu(II)\text{-reduction}}$ < 250 °C, the transition of $Cu^{+}$ 1s to 4p at ca. 8983 eV is showing up and gradually decreases upon further temperature increase (Figure 3). Ikuno et al. demonstrated that a He pretreatment with subsequent oxygen treatment leads to the same Cu-speciation and same product yield as indirect oxygen treatment.[15]

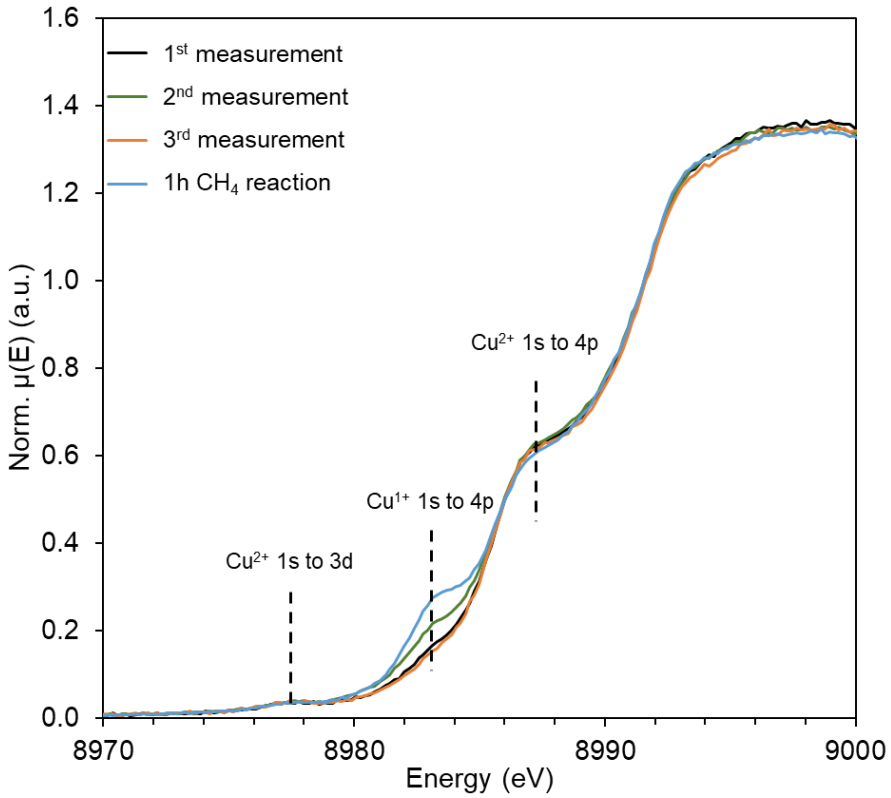


**Figure 4** Cu K-edge in situ measurements of $O_2$-activated (at 500 °C) and consecutively $CH_4$-reacted Cu-MOR with 283 µmol/g. The first two measurements were performed at the same spot of the analyzed sample and the 3rd measurement was performed 2 mm away from the initial spot. The three consecutive measurements were performed in oxygen. After 1 h of $CH_4$ reaction at 200 °C, the beam spot was further moved 2mm away. All three measurements were performed at r.t..

Showing that the formation of a Cu-oxo cluster is a combination of thermal activation of the cationic Cu species followed by an oxidation step. The formation of $Cu^+$ species and reoxidation to $Cu^{2+}$ in Cu-zeolites have been reported to occur also during the heating ramp of the oxygen treatment.[7] The dynamic nature of the *in situ* characterization of oxygen activation or He-treatment does not allow us to distinguish between beam-induced and thermally-induced autoreduction. Bokhoven et al. recently reported the influence of X-ray doses on the $Cu^+$ quantification of Cu-MOR, where the $Cu^{2+}$ reduction to $Cu^+$-species is occurring upon X-ray exposure.[18] X-ray beam induced damage on Cu-materials is not only limited to Cu-zeolites, but is also a well-known issue in different disciplines.[61-65] Therefore, we exposed an oxygen activated Cu-MOR to X-rays. Figure 4 clearly shows the extent of X-ray exposure over time on an oxygen activated Cu-MOR sample in $O_2$-atmosphere. The consecutive first two XANES

measurements, which were performed on the same beam spot, show a transformation of $Cu^{2+}$ species of Cu-oxo species to $Cu^{+}$.

After moving the beam spot 2 mm away from the initial spot for a 3rd measurement, the initial state of the oxidized Cu-MOR sample can be seen. Although the Cu-MOR sample is not exposed to any reducing condition e.g. in an inert atmosphere in combination with high temperature or $CH_4$-reaction conditions, Cu-MOR shows a significant increase of $Cu^{+}$ species. As a comparison, the degree of beam induced autoreduction upon X-ray exposure on the same beam spot reaches almost half the amount of $Cu^{+}$ resulting from a 1 h $CH_4$ -reaction (Figure 4).

Radiation damage can occur through primary and secondary types.[63] Primary beam induced damage is triggered by the direct interaction of ionizing radiation with the electrons via photoelectric, Auger, or Compton effects, damaging the chemical bonds of the investigated material.[63] Secondary processes involve energetic electrons, which are generating reactive species such as free radicals and change the chemical state of the material.[63] Primary damage depends on the incident X-rays and photon flux, secondary damage depends on the properties of the material.[63] Therefore, we conclude that the sensitive and highly reactive $Cu^{2+}$ species of oxygen activated Cu-MOR can be solely reduced upon X-ray exposure. In addition, parallel autoreduction of $Cu^{2+}$ species during the heating ramp of the oxygen treatment might occur through X-ray induced reduction and not only by thermally driven autoreduction.

### *2.4.4 Reduction Behavior of $Cu^{2+}$-Species in MOR*

High temperature He-treatment of Cu-MOR leads to the transformation of $Cu^{2+}$ to $Cu^{+}$ via autoreduction, which is a popular tool to access the reduction potential of Cu-species in Cu-oxo cluster present in Cu-zeolites.[3, 8-10, 12, 14, 53] Figure 5 shows the thermal autoreduction process in He on a Cu-MOR leads to complete autoreduction of $Cu^{2+}$-species. Upon temperature increase the white line decreases due to dehydration and $Cu^{2+}$ is gradually reduced to $Cu^{+}$, which can be seen on the increasing $Cu^{+}$ 1s to 4p transition.[3, 7-10, 12, 14, 15, 53]

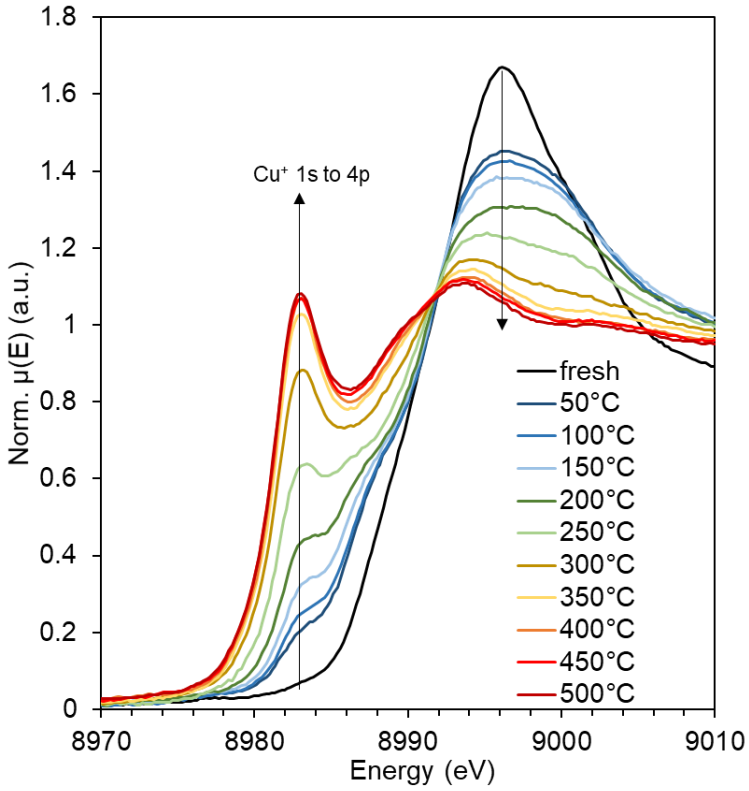


**Figure 5** In situ Cu K-edge XANES of Cu-MOR with 283 µmol/g during He activation.

Paolucci et al. proposed the mechanism of autoreduction in Cu-CHA to happen by the thermally induced reduction of initially present $[Cu(OH)]^{+}$.[66] In addition, Martini et al. showed that nearly all of the $Cu^{2+}$ species present as $[Cu(OH)]^{+}$, in a Cu-CHA with optimized Si/Al and Cu/Al, are autoreduced at 673 K.[52] Furthermore, Ikuno et al. showed that $Cu^{2+}$ species are exchanged at as $[Cu(H_2O)_5OH]^{+}$,[ref] and further dehydrate to $[Cu(OH]^{+}$ attached to the framework Al upon heating.[15] The formation of $Cu^{+}$ is hypothesized to happen over the thermally driven emission of the Cu-O-Cu

oxygen, formed by the condensation of two $[Cu(OH)]^+$, or/and by the generation of OH radicals from $[Cu(OH)]^+$.[15]

Sushkevich et al. recently reported the reduction of $Cu^{2+}$ by carbon residue in Cu-MOR samples, originating from Cu-precursor such as $Cu(OAc)_2$.[67] Removal of such carbon residues by thermal treatment have shown to be an effective way to avoid such effects. As all our Cu-MOR samples are treated in synthetic air at high temperatures (500 °C) separately before XAS-measurements, we do not expect any carbon residues that could cause a reduction of $Cu^{2+}$-species during thermal treatment.

Brezicki et al. analyzed the autoreduction mechanism by XANES-Linear Combination Fitting (LCF) analysis of the collected spectra during He-treatment.[12] The standards for the LCF analysis were a fresh Cu-MOR as hydrated $Cu^{2+}$ standard, the dehydrated/oxygen-activated Cu-MOR as dehydrated $Cu^{2+}$ standard, and the He-treated Cu-MOR as $Cu^+$ standard. The authors, however, assume that Cu-oxo species and $[Cu(OH)]^{2+}$ species are both represented in the Cu K-edge XANES measurement of oxygen activated Cu-MOR state.

Applying the same approach on the XANES spectra collected during He-treatment of Cu-MOR reveals that approximately 52% of the Cu is either $[Cu(OH)]^+$ or Cu-oxo until 200°C, whereas hydrated $Cu^{2+}$-species gradually decrease and $Cu^+$ gradually increases (Figure S2). This assumption might suggest that hydrated $Cu^{2+}$ dehydrate and are forming $[Cu(OH)]^+$ species, which in the course get reduced via the condensation mechanism. However, it is impossible to distinguish between $[Cu(OH)]^{2+}$ species and Cu-oxo species through this approach and to keep track of the autoreduction via condensation mechanism.

As seen in Figure 5, reduction of hydrated $Cu^{2+}$species in MOR already occurs at 50°°C. Other publications do not discuss this phenomenon, however, it is evident that $Cu^+$ formation is observable at such low temperatures. [3, 10, 12, 53] The reason for this phenomenon can be explained by the radiolysis of hydrated $Cu^{2+}$ species. Radiolysis studies of aqueous $Cu^{2+}$ solutions have shown the reduction $Cu^{2+}$ upon X-ray exposure.[63, 64] In addition, blank experiments on demineralized water, which was exposed to the X-ray beam, have been shown to lead to gas bubble formation.[63] The speed of the gas bubble formation is correlating with the flux of incoming X-rays. The radiolysis of water is caused by fragmentation of water, where both radical and ionic

species are formed.[64, 68] The fragmentation phenomenon is a primary and secondary type as the high energy beam produces a free electron, which further undergoes reaction with water (eq. 1).[63, 68-70]

$$H_2O + h\nu_{X\text{-}ray} \longrightarrow H_2O^+ + e^-_{dry} \xrightarrow{+H_2O} H_3O^+ + HO^{\cdot} + e^-_{dry} \quad (1)$$

Most of the formed species recombine to water, but some of the radiolysis products may recombine to new species such as $H_2$ and $H_2O_2$. [63, 71] Recent X-ray free electron laser (XFEL) studies on $H_2O$ showed the ionization and fragmentation of a water within femtoseconds molecule after absorption of a few photons.[72]

When comparing the Cu K-edge XANES, hydrated Cu-MOR is almost identical to $Cu^{2+}$ in an aqueous solution (Figure S4). $Cu^{2+}$ species in fresh/hydrated Cu-MOR are likely in an octahedral configuration like in a hexaaqua complex. The surrounding water ligands might undergo radiolysis upon X-ray exposure and the “free hydrated electron” cause the reduction of $Cu^{2+}$ at low temperature. Therefore, the transformation of $Cu^{2+}$ to $Cu^+$ at lower temperatures under continuous X-ray exposure of hydrated Cu-MOR species is induced by water radiolysis rather than the autoreduction mechanism.

In addition, reduction processes by radiolysis are much likely faster than the rate of heating.[63] The influence of X-rays on the reduction behavior of $Cu^{2+}$ species further raises the question if the observed parallel formation of $Cu^+$ during oxygen treatment,[53] is driven by thermal treatment. Despite the possible impact of X-ray on $Cu^{2+}$-species in zeolites, the formation of $Cu^+$-precursor is a crucial part for the formation of active Cu-oxo cluster.[15]

The influence of X-rays can be especially observed on *in situ* measurements of oxygen activated Cu-MOR reacting with $CH_4$. In order to investigate the effect of X-ray exposure during $CH_4$-reaction two separate experiments with constant and short beam exposure were performed on the same material (Figure 6). The $CH_4$ reaction experiment with constant X-ray exposure shows higher amounts of $Cu^+$. On the contrary, the Cu-MOR reacting with $CH_4$, which got exposed to X-rays after 60 min shows a lower amount of $Cu^+$ formation, indicating the severe impact on the total amount of $Cu^{2+}$ reduction during $CH_4$ reaction. As already mentioned, carbon residues during thermal treatment of Cu-zeolites can lead to $Cu^{2+}$-reduction.[67] Therefore, we

cannot exclude similar reduction effects on a Cu-MOR reacting with methane, where methoxy intermediates are decomposed under X-rays, further leading to reduction of $Cu^{2+}$ species.

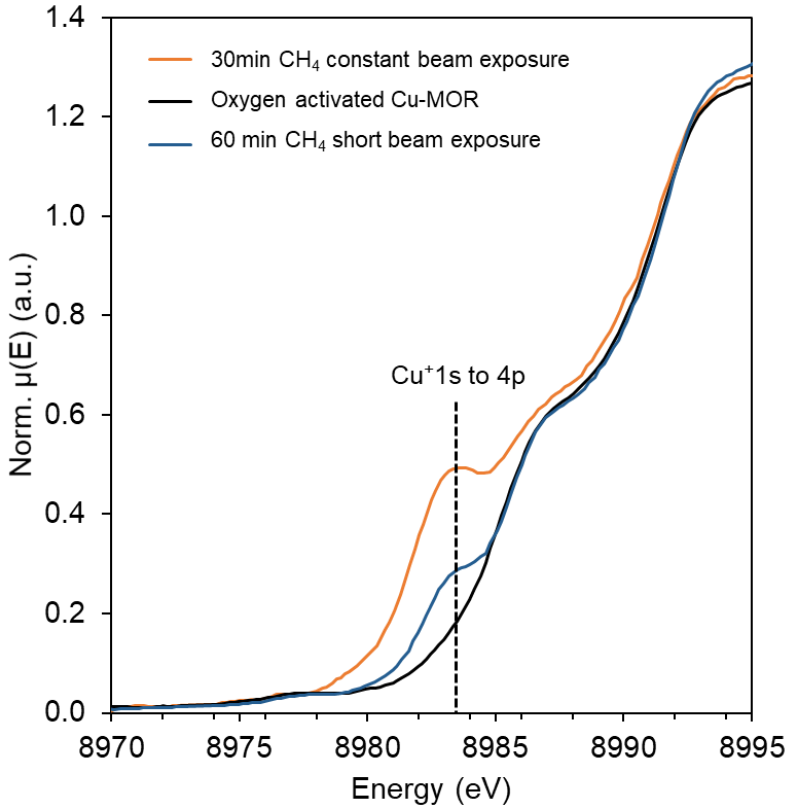


**Figure 6** Comparison of two separate experiments with constant (orange) and short (blue) beam exposure on Cu-MOR-283 (black, activated at 500°C) during $CH_4$ -reaction (at 200°C).

A well-studied Cu-MOR with a c(Cu) = 420 µmol/g is analyzed, where the active site for the selective methane oxidation has been successfully attributed to a trimeric Cu-oxo structure.[2] The $CH_4$- reaction has been analyzed Cu K-edge XANES after 3 h and the corresponding LCF-analysis shows that approximately 28 % of the $Cu^{2+}$ got reduced after $CH_4$, which is in line with the "activated $CH_4$/Cu = 0.33" (Figure S5).

These findings highly recommend to investigate Cu K-edge XAS of $CH_4$ reaction, He-treatments and oxygen activated Cu-MOR only with short X-ray exposure or with lower photon flux for minimal X-ray induced reduction. The investigation on oxygen activation and $CH_4$ reaction also suggests that beam induced autoreduction is also to be expected during He flush of activated Cu-MOR samples. Compared to FT-IR analysis

of oxidations state of Cu-species with probe molecules, Cu K-edge XANES allows us to interrogate all Cu-species. The different results on the oxidations state and speciation Cu between FT-IR and Cu K-edge XANES might also partially occur due to the different experimental setups and the experimental requirements of the two techniques.[8]

### *2.4.5 Enhancing the Spectroscopic Fingerprints by HERFD-XANES*

For deeper spectroscopic analysis, we selected the Cu-MOR with 283 micromol/g. HERFD-XANES allows us to gain further information on the spectral features. The widths of the peaks in conventional XANES depend on the 1s core-hole lifetime, while the widths in HERFD-XANES are determined by the 2p lifetime resulting in sharper spectral features.[28, 73] Monitoring the different X-ray exposure times during $CH_4$ reaction of an oxygen activated Cu-MOR reveals the existence of two different $Cu^+$ species.

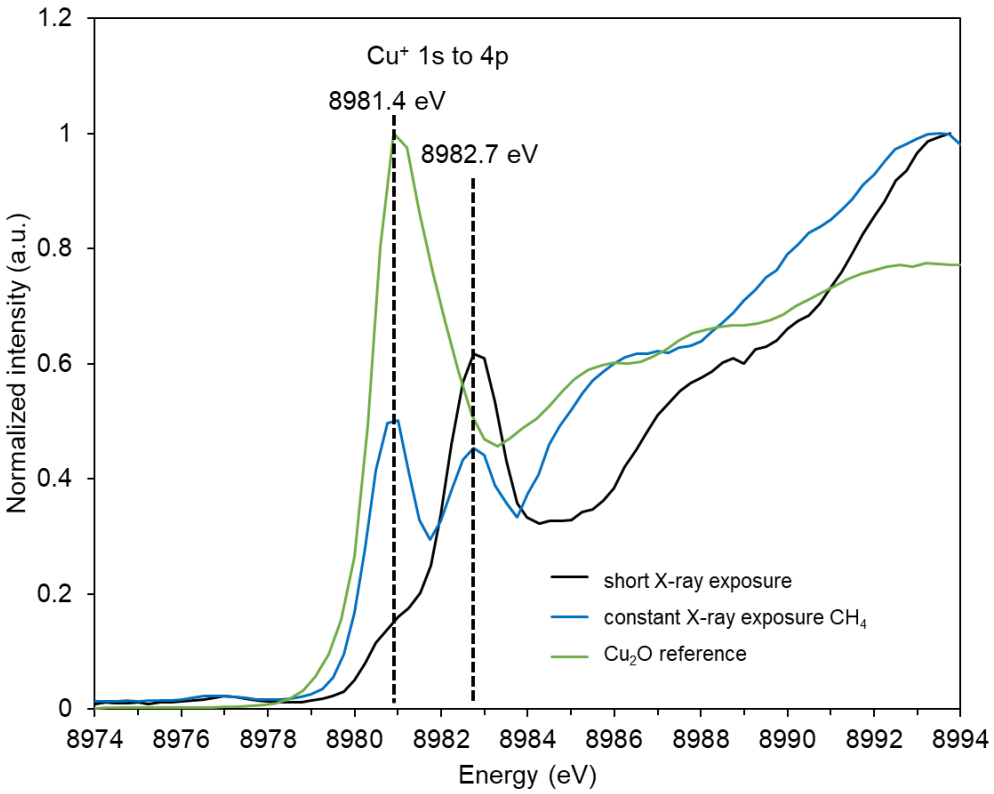


**Figure 7**. Comparison of two measurement experiments on Cu-MOR 283 with constant (blue) and short (black) X-ray exposure during $CH_4$-reaction (3h) after oxygen activation. The short X-ray exposure has been measured at the end of the 3 h $CH_4$ reaction and the constant X-ray exposure experiment has been exposed for the whole duration of the $CH_4$ reaction.

The measurement with constant beam exposure shows two prominent transitions at 8981.4 eV and 8982.7 eV, whereas the short exposure experiment shows the transition at 8982.7 eV as the most intense peak (Figure 7).

Comparison of both experiments indicates that the beam induced autoreduction of $Cu^{2+}$ corresponds to the transition at 8981.4 eV which corresponds to $Cu^{+}$ in $Cu_2O$,[56] which has a linear structure, whereas the 8982.7 eV feature belongs to $Cu^{+}$ transformed by the methane reduction. Both features are most likely convoluted in the conventional XANES due to the limitation of the 1s core-hole lifetime and hence are not visible.[28, 73] HERFD-XANES measurements are considered “photon hungry” methods, which require a high intensity and brilliant source with high photon flux compared to conventional XANES.[74] The observed beam-induced autoreduction $Cu^{2+}$ is expected to be more severe with this technique.

Based on HERFD-XANES and multivariate curve resolution (MCR) analysis, Pappas et al. have suggested that the active site in Cu-MOR consists of redox-inert Cu-species.[10] However, these results are contradicting with previous publications were a direct correlation between the autoreducible fraction of Cu and $CH_3OH$ yields were made for Cu-CHA. [10, 12] Although the HERFD-XANES measurements on He-treated Cu-MOR samples exhibit the presence and formation of $Cu^{+}$ from the beginning of oxygen activation throughout the end, the authors do not account this fact into their quantitative MCR-analysis.[10] It is evident that, the presence of $Cu^{+}$ and formation of $Cu^{+}$ can take place in both oxygen and He-treatment HERFD-XANES spectra. Furthermore, almost all the theoretical spectra derived from MCR analysis show the characteristic $Cu^{+}$ 1s to 4p transition. This feature is not expected to show up for $Cu^{2+}$ species and is leading to the assumption that $Cu^{+}$ is not formed at lower temperatures, not taking the possibility of beam induced (X-ray) radiolysis (or autoreduction).

In addition, quantitative comparisons such as LCF-analysis on HERFD-spectra by normalization[8, 10] should not be made. HERFD-XANES are incorrect XANES, which are obtained by taking a slice along the resonant inelastic X-ray scattering (RIXS) planes (Figure S6).[28] Whereas conventional XANES are directly measured by tuning the incident photon energy and normalized by pre-and post-edge line. The comparison of conventional and HERFD-XANES of CuO with a well-defined structure shows the complicated case (Figure S6). The weak pre-edge peak, which corresponds to the dipole forbidden $Cu^{2+}$ 1s to 3d transition and the $Cu^{2+}$ 1s to 4p transition are much

more enhanced in HERFD-XANES. Those transitions are in conventional XANES much lower compared to the white line. Overall intensities might be over or underestimated by HERFD-XANES and it should only be taken to further enhance spectral features, which were not detectable or separable in conventional XANES.

### *2.4.6 Activity of He-treated Cu-MOR*

According to Cu K-edge XANES, thermal treatment of Cu-MOR He leads to a majority or almost complete transformation of $Cu^{2+}$ to $Cu^{+}$. [10, 12, 14] Activity data of Cu-MOR treated in He at 500 °C, however, shows significant amounts of converted $CH_4$. The reaction products after He-treatment are with 62 and 57 µmol/g in the consecutive cycles, compared to the 139 µmol/g from oxygen treatment, quite high.

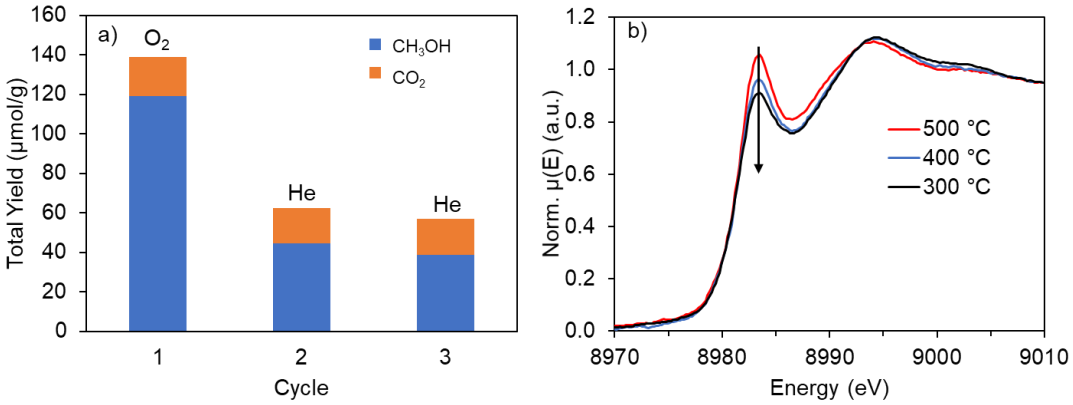


**Figure 8** a) Influence of gas during the activation procedure of Cu-MOR with 434 µmol/g on the $CH_4$ reaction. Methane reaction is performed at 200 °C for 4h and products are desorbed through steam treatment at 135 °C with 50 % $H_2O$ in He. The first cycle has been performed with an oxygen activation at 500 °C for 1h and the consecutive He cycles have been activated with He at 500 °C for 1h. The total yield consists of $CH_3OH$ (blue) and $CO_2$ (orange)- The yield of $CH_3OH$ (blue) consists of $CH_3OH$ and DME, as DME is considered as the condensation of two $CH_3OH$ molecules. b) Cu K-edge XANES of Cu-MOR with 446 µmol/g after He treatment at 500 °C for 1h and subsequent cooling to 300 °C

The dominant Cu species after He-treatment at 500 °C is expected to be $Cu^{+}$, which should not be able to oxidize $CH_4$. Brezicki et al. further analyzed the behavior by observing the Cu K-edge XANES of the cooling process after He-treatment and

speculated that traces of oxygen might partially reoxidize $Cu^+$ to active Cu-oxo species.[12] As already mentioned previously, reoxidation of He-treated Cu-MOR is easily achieved by contacting the autoreduced sample with oxygen.[15] Indeed, Cu K-edge XANES of high temperature He-treated Cu-MOR shows a decrease in $Cu^+$ upon subsequent cooling (Figure 8). Similar to Brezicki et al. a Supelco 5A Moisture trap was used for further drying and filtering of residual $O_2$ and $H_2O$ during the XAS experiments. However, small traces of $O_2$ are enough to oxidize the extremely sensitive Cu-MOR materials[12] and measurements on the elucidation of oxidations state have to be timed carefully.

## 2.5 Conclusion

In situ FT-IR spectroscopy with CO and NO, conventional Cu K-edge XANES, and Cu K-edge HERFD-XANES can elucidate the oxidation states of oxygen activated, He-treated, and $CH_4$-reacted Cu-MOR. However, the comparison of the FT-IR and Cu K-edge XAS spectroscopy demonstrates different reduction behavior of analyzed Cu-MOR. Particularly, the FT-IR experiments with NO probe molecules on autoreduced Cu-MOR show a significant amount of remaining $Cu^{2+}$-species, whereas the results from Cu K-edge XANES show that the majority of $Cu^{2+}$ species are reduced after thermal treatment. Inconsistent synthesis approaches and activation procedures in literature make direct comparisons and conclusions, especially on FT-IR with NO difficult. One reason for the difference can be found in the experimental instrumentation and conditions between FT-IR and XAS spectroscopy might be the reason for the different quantitative and qualitative outcomes.

High intense synchrotron generated X-rays utilized in many studies for the analysis of Cu-MOR have undesired effects on the active Cu-species for the selective oxidation of methane. Important reaction steps and processes such as oxygen activation, $CH_4$-reaction, and He-treatment are suffering under radiation damage. Intense and/or long X-ray exposure of oxygen activated Cu-MOR samples have the propensity to induce the reduction of $Cu^{2+}$ and kinetics derived from XANES spectra of $CH_4$-reaction can be significantly influenced by X-rays. Dynamics of He-treatment and thus the autoreduction process and mechanisms of $Cu^{2+}$ are also heavily influenced through radiolysis of hydrated Cu-MOR. Especially, quantitative assessments of Cu oxidation states during different conditions e.g. oxygen activation, He-treatment, etc. might be heavily distorted.

Great care has to be taken for the time frame of XANES measurements, as small trace impurities of $O_2$ can lead to reoxidation of $Cu^{+}$-species generated by He-treatment. All these effects can lead to complications in the interpretation of XAS results and thus misleading conclusions on the reactivity and nuclearity of Cu-oxo clusters in Cu-zeolites. The extent and speed of X-ray induced reduction on Cu-zeolites depend on the individual X-ray fluxes of the respective beamlines and each experiment must be systematically checked. Reliable XAS data under such conditions are still obtainable by constant observation of radiation damage, short X-ray exposures (or attenuation), and constant change of the beam spot on the sample.

## 2.6 Acknowledgement

The financial support from Deutsche Forschungsgemeinschaft (DFG, Project number 326562156) and the TUM International Graduate School of Science and Engineering (IGSSE) is acknowledged. The author acknowledges DESY beamlines P-64 and P-65 (Hamburg, Germany), a member of the Helmholtz Association HGF, for the provision of experimental facilities for X-ray experiments. The used infrastructure of the von Hamos spectrometer at the beamline P64 was realized in the frame of projects FKZ 05K13UK1 and FKZ 05K14PP1. Takaaki Ikuno, Lei Tao, Andreas Jentys, Rachit Khare, John Fulton, and Niri Govind are acknowledged for their support.

## 2.7 Appendix

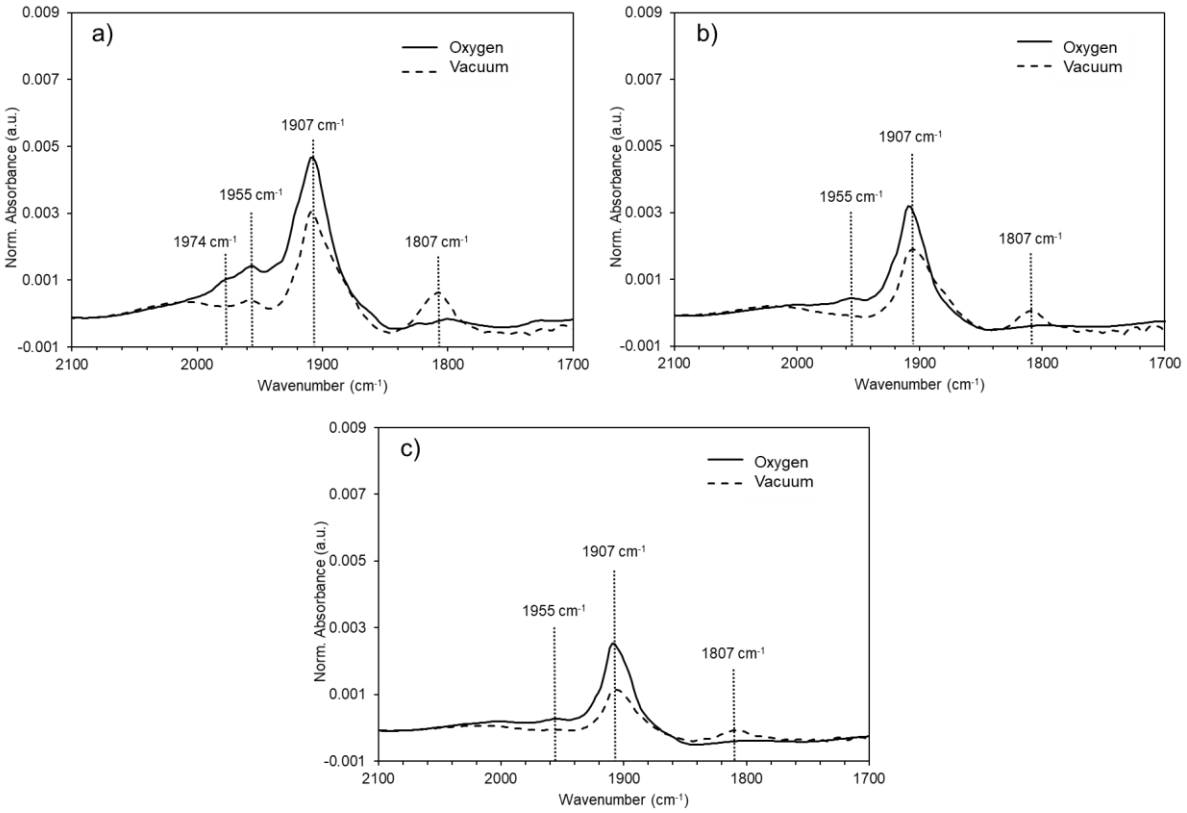


**Figure S1** FT-IR spectra of NO (p = 0.01mbar) adsorbed at liquid nitrogen temperature on oxygen (full line) and vacuum-activated (dotted line) a) Cu-MOR with a c(Cu) = 380 µmol/g, b) 156 µmol/g and c) 99 µmol/g.

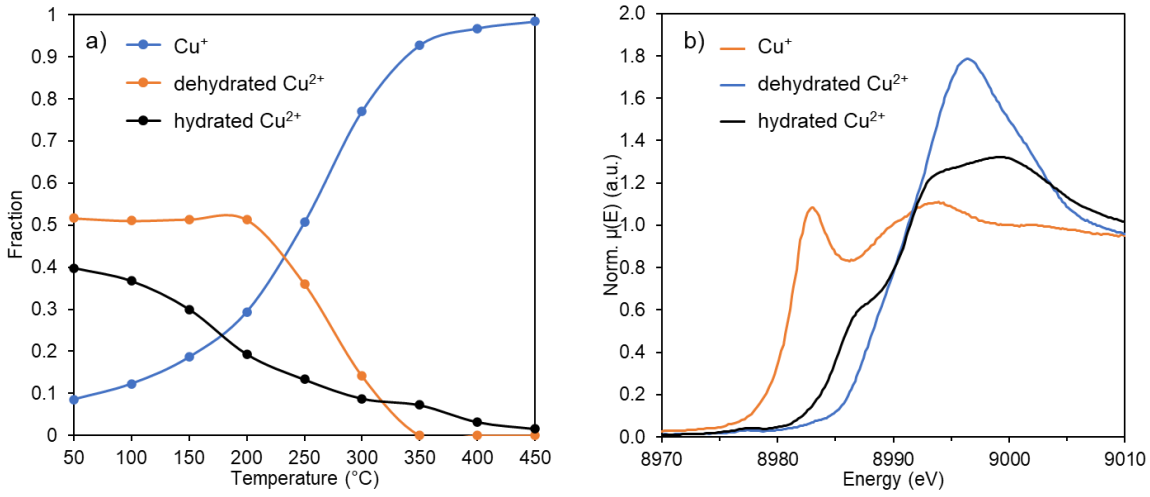


**Figure S2** a) Evolution of Cu speciation of Cu-MOR10 -3 280 catalyst during autoreduction in He. b) Cu standards used in XANES- LCF during He-treatment of Cu-MOR 283. $Cu^{+}$ standard is the Cu-MOR 283 after 1h He-activation at 500°C, the dehydrated $Cu^{2+}$ standard is the Cu-MOR 283 after 1h oxygen activation at 500 °C and the hydrated $Cu^{2+}$ standard is the fresh Cu-MOR 283.

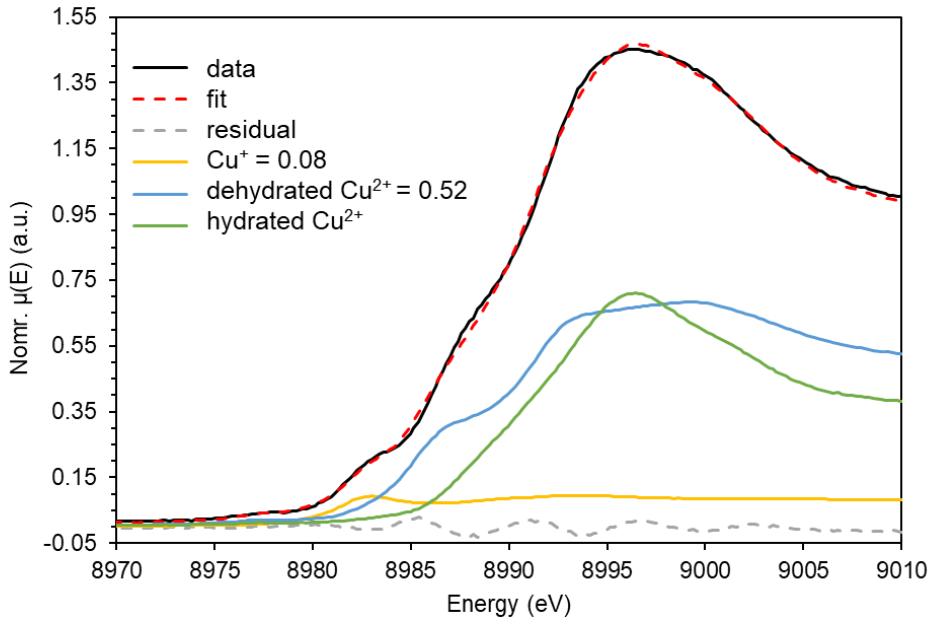


**Figure S3** XANES-LCF fitting of Cu-MOR 283 at 50°C in He. Fitting was performed by using the standards in Figure S2b.

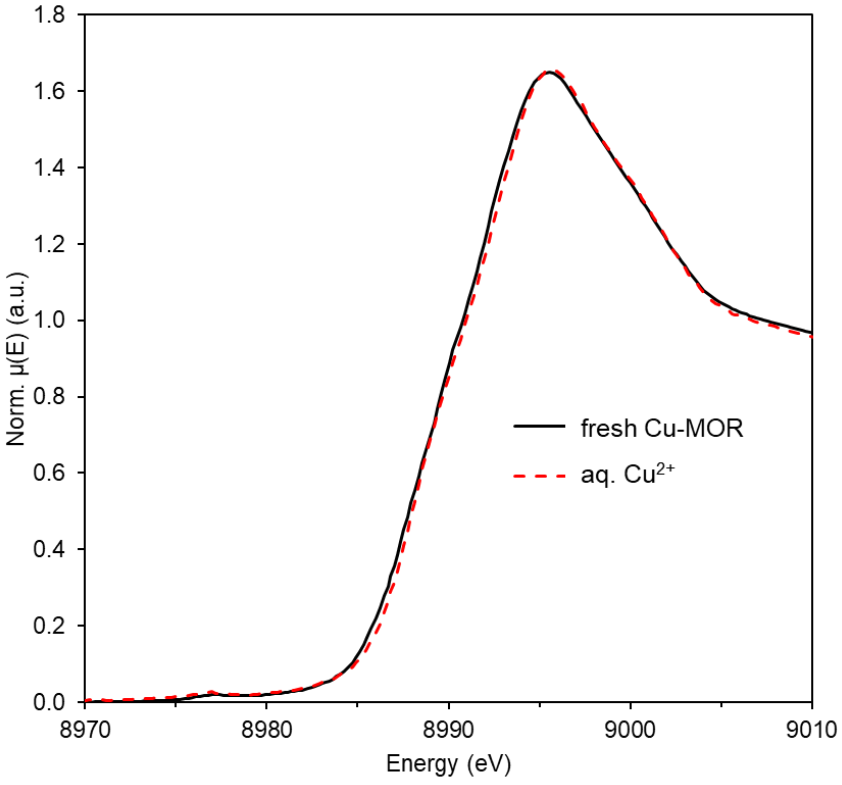


**Figure S4** Cu K-edge XANES of fresh (hydrated) Cu-MOR (black) and aqueous $Cu^{2+}$ (red dotted).

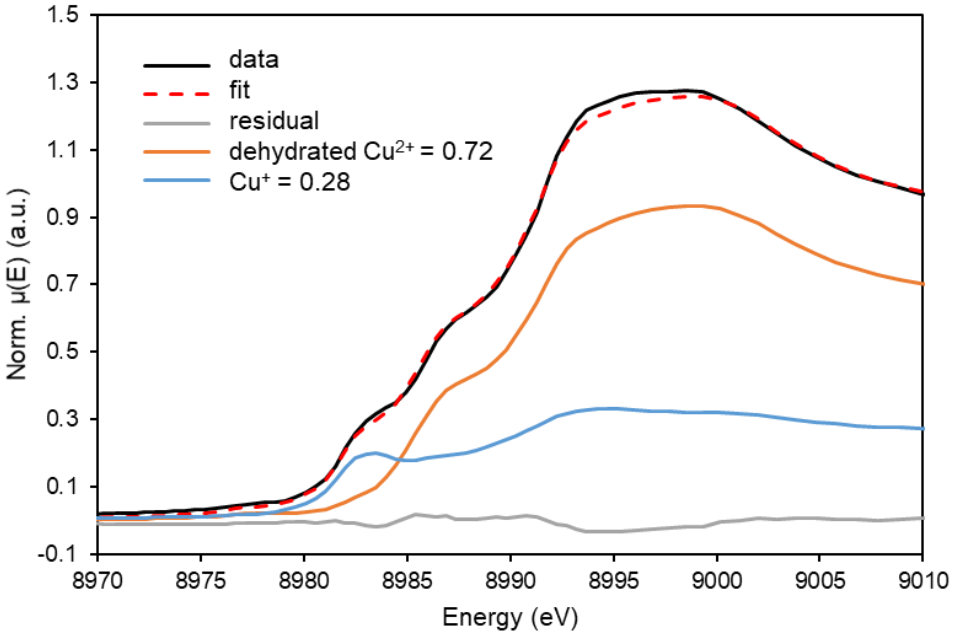


**Figure S5** LCF XANES-LCF fitting of Cu-MOR 420 µmol/g, where the active site has been attributed to a trimeric $[Cu_3O_3]^{2+}$ Cu-oxo cluster. Fitting was performed by using the oxygen activated Cu-MOR as dehydrated $Cu^{2+}$ standard and the He-treated Cu-MOR as the $Cu^{+}$ standard.

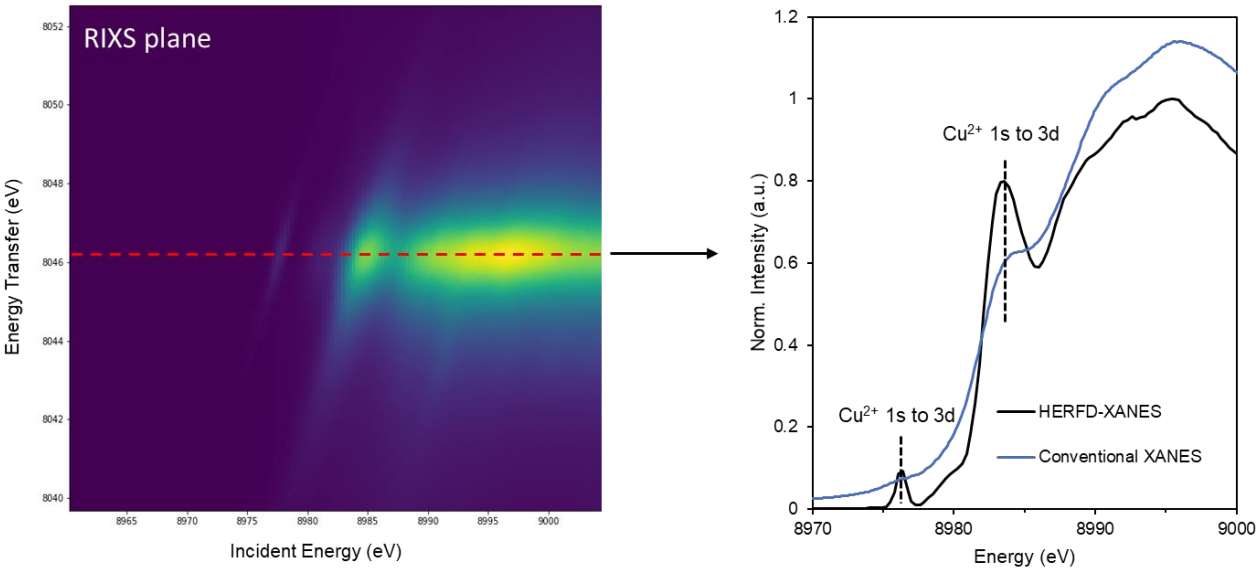


**Figure S6** HERFD-XANES of CuO sliced from RIXS-planes.

## 2.8 References


1. M. H. Groothaert, J. A. van Bokhoven, A. A. Battiston, B. M. Weckhuysen, R. A. Schoonheydt, Bis(μ-oxo)dicopper in Cu-ZSM-5 and Its Role in the Decomposition of NO: A Combined in Situ XAFS, UV−Vis−Near-IR, and Kinetic Study. *J. Am. Chem. Soc.,* (2003), **125**, 7629-7640.

2. S. Grundner *et al.*, Single-site trinuclear copper oxygen clusters in mordenite for selective conversion of methane to methanol. *Nat. Comm.,* (2015), **6**, 7546.

3. E. M. C. Alayon, M. Nachtegaal, A. Bodi, M. Ranocchiari, J. A. van Bokhoven, Bis(μ-oxo) versus mono(μ-oxo)dicopper cores in a zeolite for converting methane to methanol: an in situ XAS and DFT investigation. *Phys. Chem. Chem. Phys.,* (2015), **17**, 7681-7693.

4. E. M. Alayon, M. Nachtegaal, M. Ranocchiari, J. A. van Bokhoven, Catalytic conversion of methane to methanol over Cu–mordenite. *ChemComm,* (2012), **48**, 404-406.

5. E. M. C. Alayon, M. Nachtegaal, E. Kleymenov, J. A. van Bokhoven, Determination of the electronic and geometric structure of Cu sites during methane conversion over Cu-MOR with X-ray absorption spectroscopy. *Microporous Mesoporous mater.,* (2013), **166**, 131-136.

6. E. M. C. Alayon, M. Nachtegaal, A. Bodi, J. A. van Bokhoven, Reaction conditions of methane-to-methanol conversion affect the structure of active copper sites. *ACS Catal.,* (2014), **4**, 16-22.

7. E. Borfecchia *et al.*, Evolution of active sites during selective oxidation of methane to methanol over Cu-CHA and Cu-MOR zeolites as monitored by operando XAS. *Catal. Today,* (2019), **333**, 17-27.

8. D. K. Pappas *et al.*, Influence of Cu-speciation in mordenite on direct methane to methanol conversion: Multi-Technique characterization and comparison with NH3 selective catalytic reduction of NOx. *Catal. Today,* (2021), **369**, 105-111.

9. D. K. Pappas *et al.*, Methane to Methanol: Structure–Activity Relationships for Cu-CHA. *J. Am. Chem. Soc.,* (2017), **139**, 14961-14975.

10. D. K. Pappas *et al.*, The Nuclearity of the Active Site for Methane to Methanol Conversion in Cu-Mordenite: A Quantitative Assessment. *J. Am. Chem. Soc.,* (2018), **140**, 15270-15278.

11. D. K. Pappas *et al.*, Understanding and Optimizing the Performance of Cu-FER for The Direct CH4 to CH3OH Conversion. *ChemCatChem,* (2019), **11**, 621-627.

12. G. Brezicki, J. D. Kammert, T. B. Gunnoe, C. Paolucci, R. J. Davis, Insights into the Speciation of Cu in the Cu-H-Mordenite Catalyst for the Oxidation of Methane to Methanol. *ACS Catal.,* (2019), **9**, 5308-5319.

13. G. Brezicki, J. Zheng, C. Paolucci, R. Schlögl, R. J. Davis, Effect of the Co-cation on Cu Speciation in Cu-Exchanged Mordenite and ZSM-5 Catalysts for the Oxidation of Methane to Methanol. *ACS Catal.,* (2021), **11**, 4973-4987.

14. V. L. Sushkevich, A. V. Smirnov, J. A. van Bokhoven, Autoreduction of Copper in Zeolites: Role of Topology, Si/Al ratio, and Copper Loading. *J. Phys. Chem. C,* (2019), **123**, 9926-9934.

15. T. Ikuno *et al.*, Formation of Active Cu-oxo Clusters for Methane Oxidation in Cu-Exchanged Mordenite. *J. Phys. Chem. C,* (2019), **123**, 8759-8769.

16. J. Zheng *et al.*, Importance of Methane Chemical Potential for Its Conversion to Methanol on Cu-Exchanged Mordenite. *Chem. Eur. J.,* (2020), **26**, 7563-7567.

17. V. L. Sushkevich, D. Palagin, M. Ranocchiari, J. A. v. Bokhoven, Selective anaerobic oxidation of methane enables direct synthesis of methanol. *Science,* (2017), **356**, 523-527.

18. M. A. Newton *et al.*, Unwanted effects of X-rays in surface grafted copper(ii) organometallics and copper exchanged zeolites, how they manifest, and what can be done about them. *Phys. Chem. Chem. Phys.,* (2020), **22**, 6826-6837.

19. M. H. Groothaert, P. J. Smeets, B. F. Sels, P. A. Jacobs, R. A. Schoonheydt, Selective Oxidation of Methane by the Bis(μ-oxo)dicopper Core Stabilized on ZSM-5 and Mordenite Zeolites. *J. Am. Chem. Soc.,* (2005), **127**, 1394-1395.

20. K. I. Hadjiivanov, G. N. Vayssilov, in *Advances in Catalysis*. (Academic Press, 2002), vol. 47, pp. 307-511.

21. R. Bulánek, Investigation of IR vibrational band of C–O bond of carbonyl species in Cu+-MFI zeolites. *Phys. Chem. Chem. Phys.,* (2004), **6**, 4208-4214.

22. A. Zecchina *et al.*, Mono-, Di-, and Tricarbonylic Species in Copper(I)-Exchanged Zeolite ZSM-5: Comparison with Homogeneous Copper(I) Carbonylic Structures. *J. Phys. Chem. B,* (1999), **103**, 3833-3844.

23. R. Kefirov, A. Penkova, K. Hadjiivanov, S. Dzwigaj, M. Che, Stabilization of Cu+ ions in BEA zeolite: Study by FTIR spectroscopy of adsorbed CO and TPR. *Microporous Mesoporous mater.,* (2008), **116**, 180-187.

24. R. Zhang *et al.*, NO Chemisorption on Cu/SSZ-13: A Comparative Study from Infrared Spectroscopy and DFT Calculations. *ACS Catal.,* (2014), **4**, 4093-4105.

25. M. Tortorelli, K. Chakarova, L. Lisi, K. Hadjiivanov, Disproportionation of associated Cu2+ sites in Cu-ZSM-5 to Cu+ and Cu3+ and FTIR detection of Cu3+(NO)x (x=1, 2) species. *J. Catal.,* (2014), **309**, 376-385.

26. B. Wichterlová, J. Dědeček, Z. Sobalík, A. Vondrová, K. Klier, On the Cu Site in ZSM-5 Active in Decomposition of NO: Luminescence, FTIR Study, and Redox Properties. *J. Catal.,* (1997), **169**, 194-202.

27. J. Szanyi, J. H. Kwak, H. Zhu, C. H. F. Peden, Characterization of Cu-SSZ-13 NH3 SCR catalysts: an in situ FTIR study. *Phys. Chem. Chem. Phys.,* (2013), **15**, 2368-2380.

28. I. Lee *et al.*, Activity of Cu–Al–Oxo Extra-Framework Clusters for Selective Methane Oxidation on Cu-Exchanged Zeolites. *JACS Au,* (2021), **1**, 1412-1421.

29. C. Lamberti *et al.*, XANES, EXAFS and FTIR characterization of copper-exchanged mordenite. *J. Chem. Soc. Faraday Trans.,* (1998), **94**, 1519-1525.

30. V. L. Sushkevich, M. Artsiusheuski, D. Klose, G. Jeschke, J. A. van Bokhoven, Identification of Kinetic and Spectroscopic Signatures of Copper Sites for Direct Oxidation of Methane to Methanol. *Angew. Chem., Int. Ed.,* (2021), **60**, 15944-15953.

31. V. Zdravkova, N. Drenchev, E. Ivanova, M. Mihaylov, K. Hadjiivanov, Surprising Coordination Chemistry of Cu+ Cations in Zeolites: FTIR Study of Adsorption and Coadsorption of CO, NO, N2, and H2O on Cu–ZSM-5. *J. Phys. Chem. C,* (2015), **119**, 15292-15302.

32. G. Turnes Palomino *et al.*, Oxidation States of Copper Ions in ZSM-5 Zeolites. A Multitechnique Investigation. *J. Phys. Chem. B,* (2000), **104**, 4064-4073.

33. C. Lamberti *et al.*, XAFS, IR, and UV−Vis Study of the CuI Environment in CuI-ZSM-5. *J. Phys. Chem. B,* (1997), **101**, 344-360.

34. F. X. Llabrés i Xamena *et al.*, Thermal Reduction of Cu2+−Mordenite and Re-oxidation upon Interaction with H2O, O2, and NO. *J. Phys. Chem. B,* (2003), **107**, 7036-7044.

35. V. L. Sushkevich, J. A. van Bokhoven, Effect of Brønsted acid sites on the direct conversion of methane into methanol over copper-exchanged mordenite. *Catal. Sci. Technol.,* (2018), **8**, 4141-4150.

36. A. Zecchina *et al.*, Formation of Nonplanar CuI(CO)3Tricarbonyls on CuI–ZSM-5:An FTIR Study at 80 K. *J. Catal.,* (1998), **173**, 540-542.

37. D. Palagin, V. L. Sushkevich, A. J. Knorpp, M. Ranocchiari, J. A. van Bokhoven, Mapping Vibrational Spectra to the Structures of Copper Species in Zeolites

Based on Calculated Stretching Frequencies of Adsorbed Nitrogen and Carbon Monoxides. *J. Phys. Chem. C,* (2021), **125**, 12094-12106.

38. F. Giordanino *et al.*, Characterization of Cu-exchanged SSZ-13: a comparative FTIR, UV-Vis, and EPR study with Cu-ZSM-5 and Cu-β with similar Si/Al and Cu/Al ratios. *Dalton Trans.,* (2013), **42**, 12741-12761.

39. A. Guilherme Buzanich, Recent developments of X-ray absorption spectroscopy as analytical tool for biological and biomedical applications. *X-Ray Spectrom.*, **n/a**.

40. M. Wang, L. Árnadóttir, Z. J. Xu, Z. Feng, In Situ X-ray Absorption Spectroscopy Studies of Nanoscale Electrocatalysts. *Micro Nano Lett.,* (2019), **11**, 47.

41. J. Timoshenko, B. Roldan Cuenya, In Situ/Operando Electrocatalyst Characterization by X-ray Absorption Spectroscopy. *Chem. Rev.,* (2021), **121**, 882-961.

42. G. J. Sherborne, B. N. Nguyen, Recent XAS studies into Homogeneous metal catalyst in fine chemical and pharmaceutical syntheses. *Chem. Cent. J.,* (2015), **9**, 37.

43. P. Ghigna, E. Quartarone, Operando x-ray absorption spectroscopy on battery materials: a review of recent developments. *J. Phys. Energy,* (2021), **3**, 032006.

44. C. Pellegrini, The development of XFELs. *Nat. Rev. Phys.,* (2020), **2**, 330-331.

45. P. Sedigh Rahimabadi, M. Khodaei, K. R. Koswattage, Review on applications of synchrotron-based X-ray techniques in materials characterization. *X-Ray Spectrom.,* (2020), **49**, 348-373.

46. M. Fehse, A. Iadecola, L. Simonelli, A. Longo, L. Stievano, The rise of X-ray spectroscopies for unveiling the functional mechanisms in batteries. *Phys. Chem. Chem. Phys.,* (2021), **23**, 23445-23465.

47. B. Ravel, M. Newville, ATHENA, ARTEMIS, HEPHAESTUS: data analysis for X-ray absorption spectroscopy using IFEFFIT. *J. Synchroton Radiat.,* (2005), **12**, 537-541.

48. S. Grundner, W. Luo, M. Sanchez-Sanchez, J. A. Lercher, Synthesis of single-site copper catalysts for methane partial oxidation. *ChemComm,* (2016), **52**, 2553-2556.

49. M. A. C. Markovits, A. Jentys, M. Tromp, M. Sanchez-Sanchez, J. A. Lercher, Effect of Location and Distribution of Al Sites in ZSM-5 on the Formation of Cu-Oxo Clusters Active for Direct Conversion of Methane to Methanol. *Top. Catal.,* (2016), **59**, 1554-1563.

50. M. Dyballa *et al.*, On How Copper Mordenite Properties Govern the Framework Stability and Activity in the Methane-to-Methanol Conversion. *ACS Catal.,* (2019), **9**, 365-375.

51. C. W. Andersen *et al.*, Redox-Driven Migration of Copper Ions in the Cu-CHA Zeolite as Shown by the In Situ PXRD/XANES Technique. *Angew. Chem., Int. Ed.,* (2017), **56**, 10367-10372.

52. A. Martini *et al.*, Composition-driven Cu-speciation and reducibility in Cu-CHA zeolite catalysts: a multivariate XAS/FTIR approach to complexity. *Chem. Sci.,* (2017), **8**, 6836-6851.

53. E. Borfecchia *et al.*, Revisiting the nature of Cu sites in the activated Cu-SSZ-13 catalyst for SCR reaction. *Chem. Sci.,* (2015), **6**, 548-563.

54. S. C. Larsen, A. Aylor, A. T. Bell, J. A. Reimer, Electron Paramagnetic Resonance Studies of Copper Ion-Exchanged ZSM-5. *J. Phys. Chem.,* (1994), **98**, 11533-11540.

55. P. A. Jacobs, W. de Wilde, R. A. Schoonheydt, J. B. Uytterhoeven, H. Beyer, Redox behaviour of transition metal ions in zeolites. Part 3.—Auto-reduction of cupric ions in Y zeolites. *J. Chem. Soc., Faraday Trans.,* (1976), **72**, 1221-1230.

56. T. Günter *et al.*, Structural snapshots of the SCR reaction mechanism on Cu-SSZ-13. *ChemComm,* (2015), **51**, 9227-9230.

57. G. Spoto *et al.*, Cu(I)-ZSM-5 zeolites prepared by reaction of H-ZSM-5 with gaseous CuCl: Spectroscopic characterization and reactivity towards carbon monoxide and nitric oxide. *Appl. Catal. B,* (1994), **3**, 151-172.

58. V. L. Sushkevich, D. Palagin, J. A. van Bokhoven, The Effect of the Active-Site Structure on the Activity of Copper Mordenite in the Aerobic and Anaerobic Conversion of Methane into Methanol. *Angew. Chem., Int. Ed.,* (2018), **57**, 8906-8910.

59. A. J. Knorpp *et al.*, Paired Copper Monomers in Zeolite Omega: The Active Site for Methane-to-Methanol Conversion. *Angew. Chem., Int. Ed.,* (2021), **60**, 5854-5858.

60. P. Tomkins *et al.*, Isothermal Cyclic Conversion of Methane into Methanol over Copper-Exchanged Zeolite at Low Temperature. *Angew. Chem., Int. Ed.,* (2016), **55**, 5467-5471.

61. F. Stellato *et al.*, Dealing with Cu reduction in X-ray absorption spectroscopy experiments. *Metallomics,* (2019), **11**, 1401-1410.

62. J. Yang *et al.*, Soft X-ray Induced Photoreduction of Organic Cu(II) Compounds Probed by X-ray Absorption Near-Edge (XANES) Spectroscopy. *Anal. Chem.,* (2011), **83**, 7856-7862.

63. J. G. Mesu, A. M. Beale, F. M. F. de Groot, B. M. Weckhuysen, Probing the Influence of X-rays on Aqueous Copper Solutions Using Time-Resolved in Situ Combined Video/X-ray Absorption Near-Edge/Ultraviolet−Visible Spectroscopy. *J. Phys. Chem. B,* (2006), **110**, 17671-17677.

64. S. Jayanetti, R. A. Mayanovic, A. J. Anderson, W. A. Bassett, I.-M. Chou, Analysis of radiation-induced small Cu particle cluster formation in aqueous CuCl2. *J. Chem. Phys.,* (2001), **115**, 954-962.

65. K. L. Summers *et al.*, X-ray Absorption Spectroscopy Investigations of Copper(II) Coordination in the Human Amyloid β Peptide. *Inorg. Chem.,* (2019), **58**, 6294-6311.

66. C. Paolucci *et al.*, Catalysis in a Cage: Condition-Dependent Speciation and Dynamics of Exchanged Cu Cations in SSZ-13 Zeolites. *J. Am. Chem. Soc.,* (2016), **138**, 6028-6048.

67. V. L. Sushkevich, J. A. van Bokhoven, Revisiting copper reduction in zeolites: the impact of autoreduction and sample synthesis procedure. *ChemComm,* (2018), **54**, 7447-7450.

68. C. D. Jonah, A Short History of the Radiation Chemistry of Water. *Radiat. Res.,* (1995), **144**, 141-147.

69. J. A. LaVerne, S. M. Pimblott, New Mechanism for H2 Formation in Water. *J. Phys. Chem. A,* (2000), **104**, 9820-9822.

70. B. C. Garrett *et al.*, Role of Water in Electron-Initiated Processes and Radical Chemistry: Issues and Scientific Advances. *Chem. Rev.,* (2005), **105**, 355-390.

71. B. Pastina, J. A. LaVerne, S. M. Pimblott, Dependence of Molecular Hydrogen Formation in Water on Scavengers of the Precursor to the Hydrated Electron. *J. Phys. Chem. A,* (1999), **103**, 5841-5846.

72. T. Jahnke *et al.*, Inner-Shell-Ionization-Induced Femtosecond Structural Dynamics of Water Molecules Imaged at an X-Ray Free-Electron Laser. *Physical Review X,* (2021), **11**, 041044.

73. P. Glatzel, U. Bergmann, High resolution 1s core hole X-ray spectroscopy in 3d transition metal complexes—electronic and structural information. *Coord. Chem. Rev.,* (2005), **249**, 65-95.

74. M. Bauer, HERFD-XAS and valence-to-core-XES: new tools to push the limits in research with hard X-rays? *Phys. Chem. Chem. Phys.,* (2014), **16**, 13827-13837.

# 3 Activity of Cu-Al-Oxo Extra-Framework Clusters for Selective Methane Oxidation on Cu-exchanged Zeolites

## 3.1 Abstract

Cu-zeolites are able to directly convert methane to methanol via a 3-step process using $O_2$ as oxidant. Among the different zeolite topologies, Cu-exchanged mordenite (MOR) shows the highest methanol yields, attributed to a preferential formation of active Cu-oxo species in its 8-MR pores. The presence of extra-framework or partially detached Al species entrained in the micropores of MOR leads to the formation of nearly homotopic redox active Cu-Al-oxo nanoclusters with the ability to activate $CH_4$. Studies of the activity of these sites together with characterization by $^{27}Al$ NMR and IR spectroscopy leads to the conclusion that the active species are located in the 8-MR side pockets of MOR and it consists of two Cu ions and one Al linked by O. This Cu-Al oxo cluster shows an activity per Cu in methane oxidation significantly higher than of any previously reported active Cu-oxo species. To determine the structure of the active Cu-Al-oxo cluster, a combination of experimental XANES of Cu K- and L- edges, Cu K-edge HERFD-XANES, and Cu K-edge EXAFS with TDDFT and AIMD-assisted simulations is employed. The results provide evidence of a $[Cu_2AlO_3]^{2+}$ cluster exchanged on MOR Al pairs that can oxidize up to two methane molecules per cluster at ambient pressure.

---

This chapter is adapted with permission from the publication of the same title as appeared in the JACS Au: I. Lee, M. Lee, L. Tao, T. Ikuno, R. Khare, A. Jentys T. Huthwelker, C. N. Borca, A. Kalinko, O. Y. Gutierrez, N. Govind, J. L. Fulton, J. Z. Hu, V. Glezakou, R. Rousseau, M. Sanchez-Sanchez, J. A. Lercher, Activity of Cu-Al-oxo extra-framework clusters for selective methane oxidation on Cu exchanged zeolite, *JACS Au* **2021**, *1*, 9, 1412-1421. Copyright [2021], I. Lee, M. Lee, L. Tao, T. Ikuno, R. Khare, A. Jentys T. Huthwelker, C. N. Borca, A. Kalinko, O. Y. Gutierrez, N. Govind, J. L. Fulton, J. Z. Hu, V. Glezakou, R. Rousseau, M. Sanchez-Sanchez, J. A. Lercher, published by American Chemical Society.

## 3.2 Introduction

Increased availability of light hydrocarbons from shale gas raised the interest in methane as feedstock for the petrochemical industry.[1] Currently, methane is mainly converted via synthesis gas to methanol, higher alcohols, and a range of hydrocarbons.[1, 2] Despite the high maturity of these routes a single step transformation would have significant advantages, triggering substantial interest in the direct conversion of methane to methanol.[2-5]

Cu exchanged zeolites have shown activity in the selective oxidation in repeatable single turnovers using $O_2$ as oxidant.[3, 6, 7] Grootheart et al. were the first to demonstrate this via a cyclic three-stage-process, which is depicted schematically in Figure 1.[8] Among the variety of zeolite topologies, zeolite MOR having straight 12 MR channels and intersecting 8 MR side pockets had the best utilization of copper.[3, 6, 9] Dimeric[10-15] and trimeric[16-19] Cu-oxo clusters have been proposed to be the main active sites. Al pairs in the 8 MR side pockets of MOR favor the formation and stabilization of such active Cu-oxo sites.[17, 18, 20, 21] It has been established that each Cu-oxo cluster is able to oxidize one $CH_4$ at ambient pressure and up to two $CH_4$ at higher $CH_4$ chemical potentials.[22]

The fraction of Cu that can be stabilized as active Cu-oxo clusters in a zeolite depends on the concentration of Al in the zeolite lattice, its crystallographic position, the fraction of Al T sites among its next nearest neighbors, and the presence of other cations in the zeolite. Optimized ion-exchange protocols and the absence of co-cations leads to high concentrations of active Cu-oxo sites.[17, 18]

In the absence of other metal cations Brønsted acidic zeolites undergo some dealumination, resulting in the formation of (partially detached) extra-framework Al (EFAl) species such as $Al(OH)_x$ $Al_xO_y$).[23-27] These EFAl species influence Brønsted acid site (BAS) catalyzed reactions.[28-32] A recent study by Dyballa et al. reported Cu-MOR materials with increased activity in methane oxidation and associated it to the presence of higher concentrations of extra-framework aluminum.[33] However, it is unknown, how EFAl influences active Cu-oxo species.

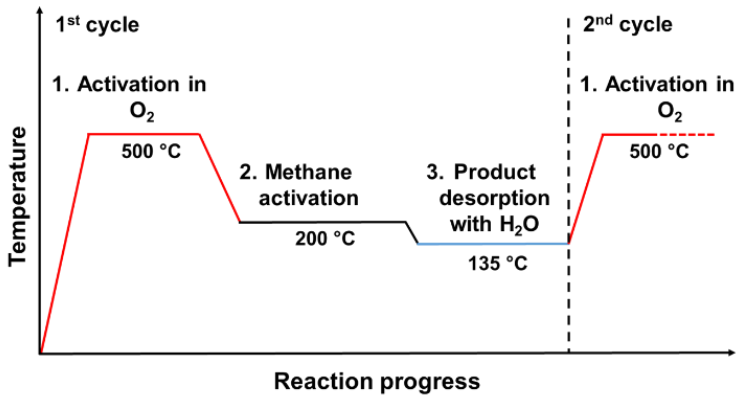


**Figure 1.** Scheme of the three stage reaction cycle for the conversion of methane to methanol over Cu-exchanged zeolites.

In this chapter, the activity of methane oxidation to methanol by Cu-oxo species in MOR in the presence of EFAl is investigated. A series of Cu-MOR series with nearly 2 times higher productivity per Cu atom than so far established for the best Cu-MOR materials is reported (under 1 bar and stepwise mode).[14, 16, 17] This drastic increase in activity points to an intrinsically different Cu-oxo species.

Using nuclear NMR and IR spectroscopy, evidence of the interaction of Cu with extra-framework Al species in these highly active Cu-exchanged zeolites is reported. To better understand the sites the Cu-MOR samples were studied by a combination of XAS and theory. HERFD and XANES of the Cu K-edge were used to define the nature and local geometry of Cu.[34] The combination of structural and chemical information derived from these measurements together with EXAFS of the Cu K- and Al K-edges of the Cu-MOR materials and Cu L-edge XANES is used to characterize the oxidation state of Cu together with highly specific information about the bonding of the oxo ligands.[35] To complement and augment experimental measurements, ground state spin-polarized DFT based AIMD simulations, EXAFS and TDDFT-based XANES calculations are performed.[36]

## 3.3 Experimental Methods

### *3.3.1 Preparation of Cu-MOR samples*

Commercial $NH_4$-MOR (Si/Al=11 and 10) were purchased from Clariant and the corresponding H-form was obtained after calcination in synthetic air (100 mL/min) at 550 °C (10K/min) for 6 h. The H-MOR samples with Si/Al = 11 and 10 were denoted as H-MOR-A and H-MOR-B.

Cu-MOR samples were prepared by aqueous ion exchange of H-MOR with $Cu^{2+}$ under controlled conditions to avoid precipitation of unwanted CuO and $Cu(OH)_2$ nanoparticles. $Cu^{2+}$-exchange was carried out at ambient temperature with 5 g zeolites in 300 mL of a 0.001-0.01 M aqueous solution of $Cu(CH_3COO)_2$ (Sigma Aldrich, 99,99%) for 20 h. The pH of the solution was kept to 5.5-6.0 during the Cu-exchange. The sample was separated from the mother liquor by centrifugation and rinsed four times with double deionized water with an intervening centrifugation step between each rinse cycle. Obtained samples were dried at 110 °C for 24 h. Cu-zeolite samples were all calcined in synthetic air at 550 °C for 2 h before IR, $^{27}Al$ NMR and XAS measurement. Si, Al, Na, and Cu contents were measured by atomic absorption spectroscopy (AAS) on a UNICAM 939 AA spectrometer after dissolution in boiling hydrofluoric acid.

### *3.3.2 Testing of Activity for Selective Oxidation of Methane*

The activity of the Cu-MOR samples for the selective $CH_4$ oxidation to methanol was tested under atmospheric pressure in a stainless-steel plug flow reactor with a 4 mm inner diameter. In a typical reaction, 50 mg of Cu-MOR (250-400 µm) was first activated for 1 h in $O_2$ at 500 °C, cooled down to 200 °C, and then flushed with He. In the next step, 90% $CH_4$ in He was flown over the sample for 4 h. The samples were then cooled to 135 °C in He and steam-assisted product desorption was performed with 50% $H_2O$ in He. Reaction products were identified and quantified with online mass spectroscopy by monitoring the m/z signals of 31, 44, and 46 for $CH_3OH$, $CO_2$, and $(CH_3)_2O$ respectively. $(CH_3)_2O$ was considered as a condensation of two $CH_3OH$ molecules and therefore considered as two $CH_3OH$ equivalents. The sum of all detected products was considered as the total yield.

### *3.3.3 In Situ IR Spectroscopy*

The samples for IR spectroscopy were pressed as self-supporting wafers with a density of ca. 10 mg/cm$^2$ and activated in vacuum (1.0 x 10$^{-7}$ mbar) at 450 °C with a heating rate of 10 K/min for 1 h. The measurements of *n*-hexane adsorption were recorded on a Vertex 70 spectrometer (Bruker Optics) with a resolution of 4 cm$^{-1}$. After pretreatment, the measurements for *n*-hexane were performed at 30 °C upon adsorption (0.5 – 5 mbar) and the target pressures were equilibrated for at least 15 min. IR spectroscopy of pyridine adsorption was measured on Thermo Nicolet 5700 FT-IR spectrometer with a resolution of 4 cm$^{-1}$. After pretreatment, adsorption of pyridine was performed at 150 °C at 0.1 mbar for 1 h and subsequently evacuated for 30 min to desorb physisorbed pyridine. The measurements were performed before and after pyridine adsorption at 150 °C.

### *3.3.4 $^{27}$Al NMR Spectroscopy*

Prior to NMR measurements, the samples were hydrated in $H_2O$ (42 mbar) for at least 48 h and then packed into $ZrO_2$ rotors. $^{27}$Al MAS NMR spectra were recorded on a Bruker Avance 500 Ultrashield NMR spectrometer with a magnetic field of 11.75 T corresponding to the Lamor frequency of 130.3 MHz and the rotor was spun at 12 kHz. 2400 spectra were accumulated in a single pulse sequence with a pulse width of 1.16 µs and a relaxation delay of 2 s. Parent H-MOR zeolites were measured on a Varian-Agilent Inova 63 mm wide-bore 900 MHz NMR spectrometer. The samples were packed in a 3.2 mm pencil type MAS probe with a magnetic field of 21.1 T, corresponding to the Lamor frequency of 234.56 MHz and the rotor was spun at 20 kHz. A total of 5000 scans were recorded in a single pulse sequence with a pulse length of 2.0 µs and a relaxation delay of 1 s.

### *3.3.5 Al K-edge and Cu L-edge XAFS*

X-ray absorption spectra at Al K-edge and Cu L-edge spectra were measured at the Swiss Light Source (SLS) of the Paul Scherrer Institute (Villigen, Swiss) on PHOENIX II. The photon source is an elliptical undulator and monochromatic light was generated by a planar grating monochromator. For Al K-edge measurements, energy calibration

was achieved by setting an inflection point of a measured Al-foil to 1559.6 eV. Al K-edge and Cu L-edge measurements of the samples were consecutively performed. The samples were pressed into self-supporting pellets with a thickness of ca. 0.5 mm and placed into a multi-pellet holder. The samples were first activated in 1% $O_2$ in Ar at 800 mbar at 450 °C with a heating rate of 10 K/min for 1 h and then cooled down to room temperature. The measurements were performed before and after thermal activation in vacuum ($1.0 \times 10^{-4}$ mbar). The beam spot was constantly changed to avoid extensive radiation damage. All measurements were carried out in fluorescence mode and the incoming $I_0$ was measured as total electron yield signal taken from a 0.5 µm thin polyester foil coated with 50 nm of Ni. The described $I_0$ detector was held 1m upstream of the sample in the beamline vacuum of ca $10^{-6}$ mbar. The X-ray fluorescence signal was detected by a one-element energy dispersive Silicon drift diode (DSS, KeteK). The introduced gases were further dried by using Supelco 5A Moisture trap. ATHENA software was used during the background processing. XANES normalization follows the standard protocol used within the Athena software.[37]

### *3.3.6 Cu K-edge HERFD-XANES*

HERFD XANES measurements were carried on beamline P64 at PETRA III of DESY (Hamburg, Germany). Approximately 10 mg of the sample was in a quartz capillary reactor with an outer diameter of 1 mm and 0.02 mm wall thickness. The packed sample was then mounted on top of a gas blower for controlled heating and the sample was thermally activated in 10 % $O_2$ in He at 450 °C for 1 h with a heating rate of 10 K/min and subsequently cooled down to r.t.. Measurements were performed before and after activation. The beam spot was constantly changed to avoid extensive radiation damage. The incident photon energy was controlled by a double-crystal Si(111) monochromator and a von Hamos-type X-ray emission spectrometer with eight Si(444) mirrors were used to record the spectra. Energy calibration was performed by recording the elastic scattering at 8015 eV, 8027 eV, 8047 eV, and 8060 eV. The gas flow over the samples was introduced by Bronkhorst mass-flow controllers and the gases were further dried by using Supelco 5A Moisture trap.

### *3.3.7 Conventional Cu K-edge XANES*

Cu K-edge XANES measurements were carried out on beamline P65 at PETRA III of DESY in Hamburg, Germany. Approximately 10 mg of the sample was in a quartz capillary reactor with an outer diameter of. 1 mm and 0.02 mm wall thickness. The packed sample was then mounted on top of a gas blower for controlled heating and the sample was thermally activated in 10% $O_2$ in He at 450 °C for 1 h with a heating rate of 10 K/min and subsequently cooled down to r.t.. The beam spot was constantly changed to avoid extensive radiation damage. A double-crystal Si(111) monochromator was used to control the incident photon energy, and the spectra were recorded with ionization chamber detectors in the transmission mode. The gas flow over the samples was introduced by Bronkhorst mass-flow controllers and the gases were further dried by using Supelco 5A Moisture trap. ATHENA software was used during the background processing. XANES normalization follows the standard protocol used within the Athena software.[37]

### *3.3.8 Computational Models*

First, the cell parameters and atomic positions of the bare Si mordenite were optimized. The optimized cell parameters of 1×1×2 orthorhombic supercell, *a* = 18.1937Å, *b* = 20.5890 Å, *c* = 15.1290 Å, are in very good agreement with experimental data (*a*=18.131 Å, *b*=20.507 Å, *c*=7.5221 Å for orthorhombic unit cell).[38] Then the examined 11 different Cu-oxo and Cu-Al-oxo clusters, including one to three Cu ions connected by O or OH, at different sites in12 MR or 8-MR side-pocket of the MOR, see Figures S4 and S5 and Table S3. We substituted two framework $Si^{4+}$ ions in the MOR with two $Al^{3+}$ ions to compensate for the positive charge of the Cu clusters. Al ions were examined at different T sites, see Figure S7. Figure S7 depicts a schematic illustration of the 3 different Cu-cluster locations (12-MR or inside an 8-MR side pocket), and the 3 different T sites with a framework Al pair. Sites S1 and S2 indicate configurations with framework Al atoms at T2 sites and Cu cluster inside a 12 MR (S1) or inside an 8 MR side pocket (S2). S3 and S4 indicate configurations with Cu cluster inside an 8 MR side pocket and with framework Al atoms at T1 and T3 sites, respectively (S3 at T1/T1 and S4 at T3/T3 sites). In addition to Cu-oxo dimers and trimers, Al-containing Cu-oxo clusters were included (Figure S6).

### *3.3.9 DFT Calculations*

Periodic spin-polarized DFT calculations are performed within the generalized gradient approximation (GGA) with the exchange correlation functional of Perdew, Burke, and Ernzerhoff (PBE)[39] as implemented in the CP2K package[40, 41]. Grimme's third-generation corrections (DFT-D3) are used to take into account dispersion forces or van der Waals interactions to describe energies more precisely.[42] For the core electrons, Goedecker–Teter–Hutter (GTH) pseudopotentials are used,[43] , while the valence wave functions are expanded in terms of double-ζ quality basis, sets optimized for condensed systems to minimize linear dependencies and superposition errors.[44] Electrostatic terms are calculated using an additional auxiliary plane-wave basis set with a 400 Ry cutoff. The Γ-point approximation is employed for the Brillouin zone integration because of the significant size of the supercell.

### *3.3.10 AIMD Simulations*

Starting with a cell-optimized mordenite supercell, DFT-based AIMD simulations are performed within the canonical NVT ensemble at room temperature using a1.0 fs time step and a Nosé−Hoover chain thermostat with a frequency of 1500 $cm^{-1}$ to control the temperature to determine the local structure and their dynamic properties. The different spin multiplicities for each system were considered. For each simulation, well-equilibrated trajectories of ≥ 35 ps were collected to obtain reliable statistical properties.

### *3.3.11 EXAFS Simulations*

K-edge EXAFS spectra were simulated with FEFF8.5 program[45] using ≥ 500 snapshots extracted from NVT trajectories with equally spaced by ~0.05 ps for each system. For each system, each snapshot was used to calculate a full set of scattering (single and multiple scattering) paths for all atoms within 6.5 Å of each Cu site using FEFF8.5 program.[45] The calculated ensemble average of these scattering paths was directly compared with the experimental spectra. This approach has led to a quantitative treatment of all photoelectron single and multiple scattering paths generating an EXAFS spectrum that captures all the structural details inherent in the MD simulation, including the bond lengths, bond angles, vibrational disorder, and local symmetry about the Cu site(s). Since dynamic fluctuations are an intrinsic part of the

sampling, the simulations implicitly include an exact treatment of the Debye-Waller factors in the EXAFS simulations. This allows the direct comparison of Cu-O and Cu-Cu coordination numbers and distances between calculated and experimental EXAFS spectra (Figure S8).

### *3.3.12 XANES Calculations with Time-Dependent DFT*

Excited state XANES calculations were performed at the Cu K- and $L_3$-edge for selected systems screened from a comparison of experimental and simulated XANES spectra using a TDDFT-based restricted excitation window approach[46, 47] as implemented in the NWChem quantum chemistry program.[46, 48] This approach involves defining a model subspace of single excitations from the relevant core orbitals and is a valid ansatz because core excitation energies are well separated from pure valence−valence excitations. For each Cu site conformation, the Sapporo-TZP-2012 all-electron basis set[49] was used for the single absorbing Cu site, while other Cu atoms (s) were represented with the Stuttgart RSC 1997 ECP[50, 51]. The Si and Al were represented with the Stuttgart RLC ECPs and O and H atoms were represented with a 6-31G* basis set.[50] The exchange-correlation was treated with the PBE0 functional.[52] All boundary O atoms with unsatisfied bonds were passivated with H atoms. All calculated spectra were Lorentzian-broadened by 0.6. The ensemble averaged TDDFT XANES spectra were generated from >50 structures that were equally spaced by 0.5 ps.

## 3.4 Results and discussions

### *3.4.1 Activity of Cu-MOR Catalysts Prepared Under Controlled Conditions*

The reactivity of two Cu-MOR-series, denoted as Cu-MOR-A and Cu-MOR-B, were measured in a typical three stage reaction comprising of (1) high temperature activation 500 °C in $O_2$, (2) exposure to methane at 200 °C and 1 bar, and (3) product desorption by steam treatment. In order to compare the relative reactivity of Cu-MOR samples, we define the Cu efficiency ($Cu_{eff}$) as the molar ratio of all converted $CH_4$ to the total amount of Cu present. Previously reported values agree well with those of other authors in reporting an upper limit of $Cu_{eff}$ = 0.35 for Cu-MOR materials at 1 bar .[14, 16, 17, 22, 53] Only when the $CH_4$ chemical potential was significantly increased (by increasing $P_{CH4}$ to 40 bar, for instance) it was possible to achieve higher $Cu_{eff}$ values, in the range of 0.45-0.6.[14, 22]

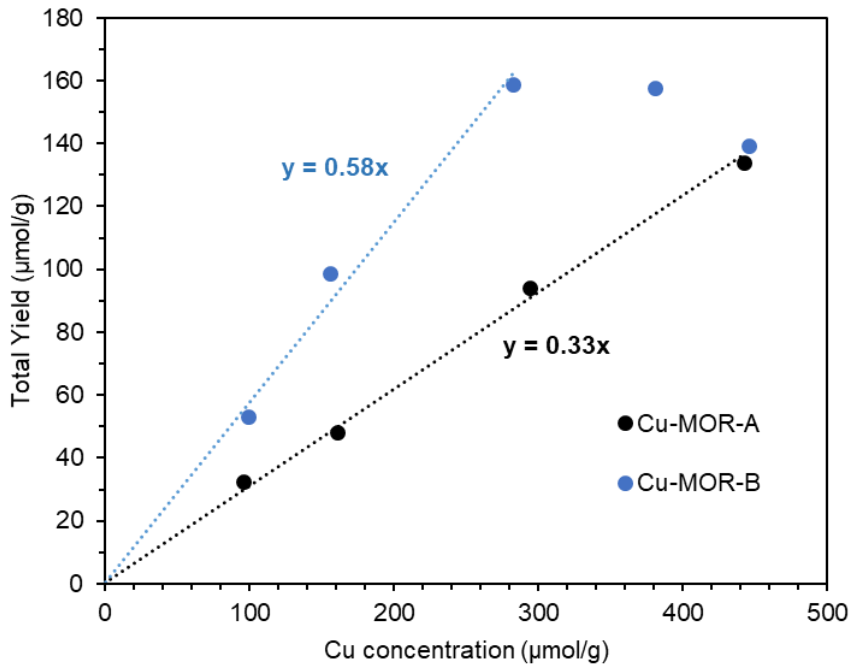


**Figure 2.** The yield of $CH_4$ oxidation on the Cu-MOR catalysts prepared from different parent H-MOR samples with different Cu loading of Cu-MOR-A and Cu-MOR-B series. Numerical values of the $Cu_{eff}$ are given as $y=Cu_{eff}x$ for Cu-MOR-A (black) and Cu-MOR-B (blue). Activity tests were repeated three times on each catalyst and averaged values are reported.

Here, an unusually high $Cu_{eff}$ for Cu exchanged on a zeolite (H-MOR-B) is reported, which contains extra-framework aluminum (EFAl) at a different T-site position. For this highly active Cu-MOR zeolite series an average $Cu_{eff}$ of 0.58 was obtained at 1 bar for Cu loadings up to 300 µmol/g (Figure 2).[14, 15, 33] Selectivities to MeOH and its dehydration product DME were in the range of 65 to 85 % (see Supporting Information Figure S1) and activity was fully restored by the oxidative treatment at least for seven consecutive catalytic cycles (Figure S2). For comparison, the Cu-MOR-A series is included, showing consistently a $Cu_{eff}$ of 0.33 and selectivities to MeOH+DME between 65 and 80% (Figure S1). Previous work on this material allows to firmly attribute the activity to the oxidation of one molecule of $CH_4$ by a $[Cu_3(\mu\text{-}O)_3]^{2+}$ cluster.[17] Characterization of these different Cu-MOR samples is used to elucidate the origin of the high efficiency achieved for the new material.

### *3.4.2 Characterization of Parent MOR-A and MOR-B Samples*

The distribution of Al in the zeolite framework is an important parameter for the location of $Cu^{2+}$ after ion exchange. Two next nearest neighboring Al tetrahedra ("Al pairs") allows best to stabilize divalent cations.[54, 55] The formation of dimeric and trimeric Cu-oxo clusters, is proposed to occur on such paired Al sites.[14, 15, 17, 56, 57] The concentration of Al pairs in the parent H-MOR materials can be determined by aqueous $Co^{2+}$-exchange.[54, 55] Two commercial zeolites MOR-A and MOR-B were employed that only differ in their Al distribution, originated by differences in the zeolite synthesis parameters. Table S1 shows the concentrations of the Al pairs for H-MOR-A (63 %) and H-MOR-B (66 %). As the number of Al pairs is nearly identical, the concentration of exchange sites alone is, thus, ruled out as a reason for the higher $Cu_{eff}$ of Cu-MOR-B. The location of the ion exchange sites was determined from the IR spectra of adsorbed *n*-hexane and pyridine on the parent H-MOR samples. *n*-Hexane is only able to interact with BAS in the 12-MR channels (Figure S3).[17, 58] Conversely, the more basic pyridine is protonated by all BAS in 12-MR and in the pore mouth of the 8-MR side pockets. Table 1 shows clearly that the concentration and location of BAS, as obtained by a combination of these probe molecules, are also similar for H-MOR-A and H-MOR-B. The location of the EFAl species is deduced from both pyridine adsorbed on Lewis acid sites and from the total Al concentration derived from the elemental analysis.

**Table 1.** Quantification of Al species and their distribution in the parent H-MOR-A and H-MOR-B, by combination of chemical analysis, IR spectroscopy of *n*-hexane and pyridine adsorption, and $^{27}$Al NMR.

| | H-MOR-A | H-MOR-B |
|---|---|---|
| Total Al (µmol/g)[a] | 1440 | 1620 |
| Total BAS (µmol/g)[b] | 1090[h] | 1130 |
| Total EFAl (µmol/g)[c] | 350 | 490 |
| $BAS_{main\ channeled}$ (µmol/g) | 400[h] | 419 |
| $BAS_{side\text{-}pockets}$ (µmol/g) | 690[h] | 706 |
| $LAS_{Py}$ (µmol/g)[e] | 260[h] | 230 |
| $EFAl_{inaccessible}$ (µmol/g)[f] | 90 | 260 |
| $Al_{Tetrahedral}$ (µmol/g)[g] | 1156 | 1290 |
| $Al_{Octahedral}$ (µmol/g)[g] | 284 | 330 |

[a] Total Al concentration is determined by elemental analysis (AAS).
[b] Total BAS concentration determined by elemental analysis after Na ion exchange of the parent H-MOR samples (assuming all $H^+$ are exchanged by $Na^+$).
[c] Total EFAl concentration was determined by [Total Al] – [Total BAS]
[d] Concentration of BAS located in 12-MR and 8-MR as determined by deconvolution of the IR-band at 3600 $cm^{-1}$ (Figure S3) after *n*-hexane adsorption.
[e] Concentration of LAS accessible by pyridine, as determined by IR spectroscopy.
[f] Concentration of EFAl located in the inaccessible bottom of 8-MR side pockets was determined by [Total EFAl] – [$LAS_{Py}$]
[g] Based on $^{27}$Al NMR.
[h] Values as reported in reference [17]

With the assumption that Lewis coordinated pyridine adsorbs in a 1:1 ratio to Al atoms of extra-framework species, the inaccessible EFAl can be calculated as the total measured Al concentration minus the sum of all BAS (framework Al) and LAS. While the total concentration of LAS determined by pyridine is similar for H-MOR-A and H-MOR-B (Table 1), the concentration of EFAl in H-MOR-B inaccessible to pyridine was significantly higher than in H-MOR-A. Therefore, it is hypothesized that this inaccessible EFAl is located near the bottom of the 8-MR side pockets.

$^{27}$Al NMR spectra in Figure S4a show two peaks at 58 and 0 ppm, corresponding to tetrahedral and octahedral Al species.[33] The octahedral Al fraction was found to account for approximately 20 % of Al for both parent H-MOR samples (Table 1). This concentration of octahedral Al determined by $^{27}$Al MAS NMR is smaller than that determined from pyridine adsorption (Table 1) suggesting that some of the EFAl-related Lewis acid sites have tetrahedral coordinated Al.[59] It should be emphasized

that H-MOR-B has about 3 times higher concentration of inaccessible EFAl than MOR-A.

### *3.4.3 Location of exchanged Cu Species in Standard and Highly active MOR*

All samples in this study have more than 90 % of Cu at ion exchange sites (determined, by $Na^+$ back-exchange see Table S2 in the SI). The preferred exchange sites for $Cu^{2+}$ in H-MOR were determined by analysis of the decrease in intensity of the band of Si-OH-Al groups at 3600 $cm^{-1}$ after $Cu^{2+}$ ion exchange. This band consists of two contributions at 3612 and 3590 $cm^{-1}$, attributed to BAS in the 12 MR main channel and the 8-MR side pockets, respectively.[57] The preferred sites for ion-exchange in MOR are the more constrained 8 MR side-pockets.[60] In Cu-MOR-A, the formation of active trimeric Cu-oxo cluster was observed selectively at the pore mouth of the 8-MR-side pockets.[17] Given the similar BAS distribution in H-MOR-A and H-MOR-B (Table 1), it is not surprising that the preferred exchange sites for $Cu^{2+}$ in the Cu-MOR-B series are also the Al-sites located in the pore mouth of 8-MR pockets.

However, it should be noted that while in Cu-MOR-A series ca. 0.7 BAS were consumed per Cu ion exchanged, it was approximately 0.9 with the Cu-MOR-B series. The ratio of 0.7 BAS/Cu in the activated sample has been explained by the location of a tri-copper cluster stabilized by two Al tetrahedra.[17] Thus, the higher involvement of BAS per $Cu^{2+}$ ion in Cu-MOR-B is a first indication for differences in the speciation of Cu ions compared to the A series.

$^{27}$Al MAS NMR spectra of Cu-MOR-B series show a significant decrease of octahedral Al, associated with EFAl with increasing Cu concentration (Figure S4b). The decrease of intensity for the tetrahedral Al-species is accompanied by a simultaneous line broadening due to the impact of the paramagnetic $Cu^{2+}$. Integration of the peak area corresponding to tetrahedral Al showed that its concentration remained constant with Cu loading. The linear decrease of octahedral Al upon Cu-exchange is, therefore, attributed to the formation of new NMR-silent Al or, alternatively, to the conversion from octahedral to tetrahedral coordination upon Cu introduction.

The quantification of Al species having different coordination based solely on NMR spectroscopy is subject to uncertainties, due to the paramagnetism of $Cu^{2+}$.[33, 61, 62]. Therefore, we used Al K-edge XAS to determine and quantify Al in different coordination. Figure 3 shows the Al XANES spectra for samples of Cu-MOR-B series.

The broad peak at 1568 eV decreases with Cu loading. Because this peak is attributed to Al in octahedral coordination, [63] the changes in Al K-XANES with increasing Cu loadings are attributed to the gradual transformation of octahedral into tetrahedral Al.[24, 63-65]

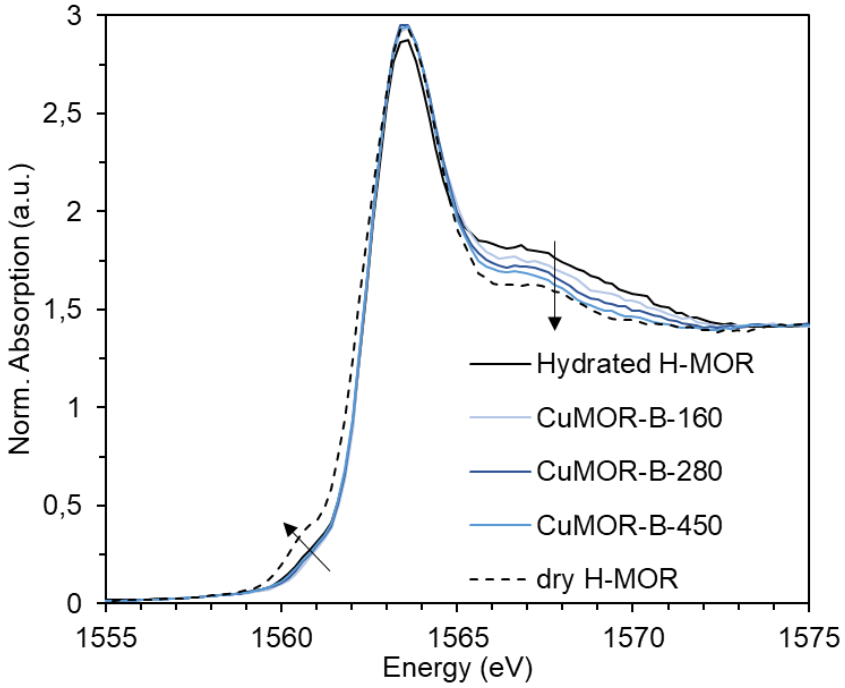


**Figure 3.** Al K-edge XANES of Cu-MOR-B series with different Cu-loadings. Measurements were performed in hydrated states unless stated.

Linear combination fitting of XANES spectra was used to determine the concentration of tetrahedral and octahedral Al species. The spectra of dehydrated H-MOR-B was taken as a reference for 0% octahedral Al, since extra-framework Al changes its coordination from octahedral to tetrahedral upon losing water ligands. A small pre-edge feature at 1560.5 eV appeared with the dehydrated form of H-MOR-B sample due to the localization of $H^+$ at the negatively charged framework Al site, resulting from the loss of $H_2O$ ligand molecules.[65] Hydrated H-MOR-B was used as a reference for octahedral Al quantification, with a concentration of 20 % EFAl as determined by $^{27}$Al MAS NMR. It can be seen from Figure 4 that the concentration of octahedral Al decreased with increasing Cu-concentration, in good agreement with $^{27}$Al MAS NMR spectra (Figure 4, hollow symbols). The relative amount of tetrahedral Al linearly increased with increasing Cu-concentration.

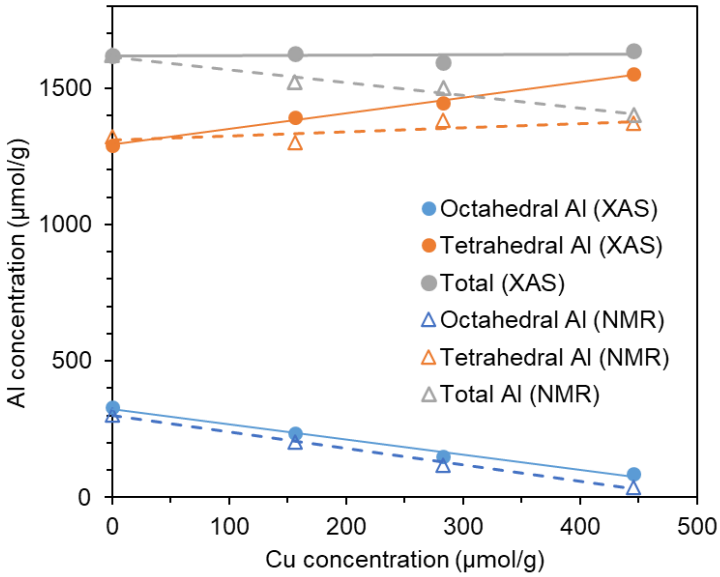


**Figure 4.** The concentration of tetrahedral, octahedral and total Al of hydrated Cu-MOR-B series obtained by LCF of Al K-edge XANES (full symbols) and $^{27}$Al NMR measured on 500 MHz instrument (hollow symbols).

These results lead to the hypothesis that the direct interaction of octahedral Al with $Cu^{2+}$ ions induces the change in Al coordination. In view of the calculated concentrations of octahedral Al by XAS and NMR, we conclude that the linear decrease of the octahedral fraction of Al is mainly due to the change in coordination upon interaction with Cu ions. In particular, concentrations obtained from Al XAS analysis (Figure 4) point to the reaction of ca. 2 Cu atoms with 1 Al. The specific interaction of $Cu^{2+}$ with octahedral, i.e., extra-framework, suggests the formation of tetrahedral Al, and of $CuAl_xO_y$ nanoclusters as possible structure, with x = 0.5.

### *3.4.4 X-ray Absorption Spectroscopic Study of Highly Active Cu-MOR species*

In order to investigate a representative member of the Cu-MOR-B series, a sample with a Cu concentration of 283 µmol/g and a $Cu_{eff}$ of 0.58 was selected for detailed XAS experimental studies in combination with computational studies. Figure 5 shows the Cu K-edge and Cu $L_3$-edge XANES of $O_2$ activated CuMOR-B-280. The combined use of K- and $L_3$-edge XANES allows unambiguous determination of the coordination structure and environment of Cu. Using HERFD-XANES resolves spectral features in the Cu K edge (Figure 5a) that are not detectable using conventional XANES.[66-69]

However, it must be noted that the peak heights are different between the two measurements. The Cu K-edge XANES spectrum is provided for comparison (Figure S5a) in the SI.

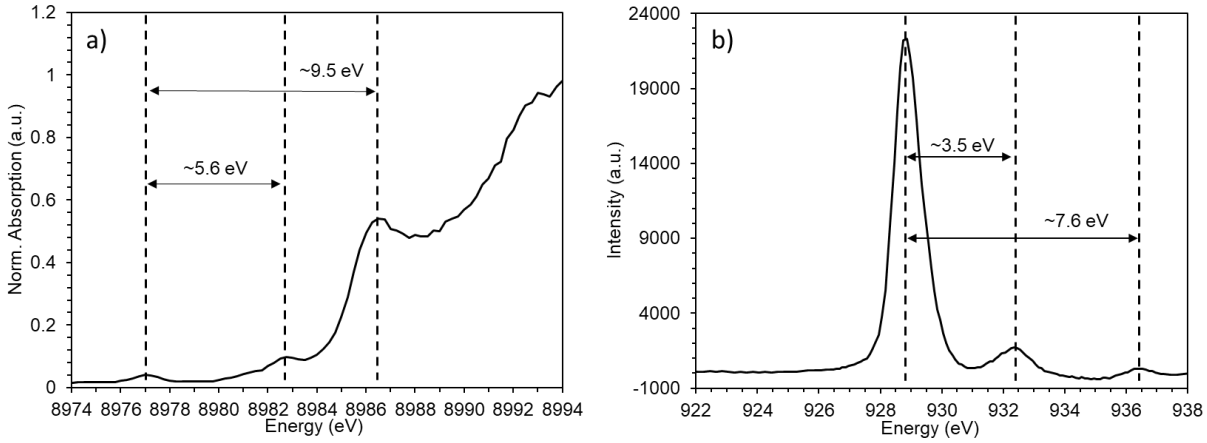


**Figure 5.** a) Cu K-edge HERFD-XANES b) Cu $L_3$-edge XANES of CuMOR-B-280 activated in $O_2$ at 450 °C for 1h.

In Cu K-edge XANES the pre-edge peak at ca. 8977.3 eV is attributed to quadrupole allowed 1s to 3d transitions. The appearance of the pre-edge feature is an indicator that Cu species in this Cu-MOR material are predominantly $Cu^{2+}$. Between the pre-edge at 8977.3 eV and the peak at 8986.7 eV (ΔE = 9.5 eV), a peak appeared at ca. 8982.8 eV (ΔE = 5.6 eV) (Figures 5a and S5a). The energy corresponds to the $Cu^+$ 1s to 4p transition and is hypothesized to indicate either presence of $Cu^+$ stabilized by the zeolite,[14, 15, 57, 66] or is caused by beam damage due to the larger X-ray dose in HERFD-XANES.[70, 71] In either form, this cation would not be actively involved in $CH_4$ oxidation. Figure 5b shows the $L_3$-edge XANES of CuMOR-B-280 with the main peak at ca. 928.8 eV and distinct satellite peaks at ca 932.4 eV and 936.5 eV.

### 3.4.5 *Structural Assignment of Cu Species using AIMD and simulated K- and $L_3$-edge XANES and EXAFS Spectra*

After establishing that Al is part of the active site, 11 Cu-Al-oxo and Cu-oxo clusters have been explored by AIMD simulations. The cluster models studied and the snapshots extracted from AIMD trajectories are shown in Figure S6. AIMD simulations at 298 K with clusters and Al atoms at different sites are compiled in Figure S8. As $Cu^{2+}$ has been established to be located in the 8-MR side pockets of MOR,[17, 18, 72, 73] only clusters in that location were considered. For a tentative composition of $Cu_2AlO_3$, two configurations are considered, i.e., one with the Al atom away from the MOR surface (Cu-Al-Cu), and another with Al near the surface (Al-Cu-Cu). Spin multiplicities were found only to have a minor influence on the results. The simulated systems are listed in Table S3 of SI. It should be emphasized at this point that the strength of the spectroscopic characterization and the associated modeling lies in the fact that three probes must yield agreement: XANES at the K and the $L_3$ edge as well as the K edge EXAFS. Only this combination provides the ability of an unequivocal assignment, while each of the approaches alone would remain ambiguous, even when experiment and modeling are combined.

The comparison of both k- and R-space EXAFS simulated spectra with the experiments indicates that neither Cu monomers, nor mono-oxo $[Cu\text{-}(\mu\text{-}O)\text{-}Cu]^{2+}$ and mono-hydroxo dicopper $[Cu\text{-}(OH)\text{-}Cu]^{2+}$ clusters or the $[Cu_2AlO_3]^{2+}$ with the Al-Cu-Cu configuration are likely structures. For these model clusters, EXAFS simulations show large discrepancies with the experimental data obtained on the current samples in peak positions and/or intensities (Figure S8 in SI). Figure 6a compiles snapshots of simulated structures having a reasonable agreement with the experiment. Figures 6b and S10 show the averaged k- and R-space EXAFS, respectively, for these selected structures. In Figures 6c and 6d, we also show the corresponding ensemble averaged K-edge and $L_3$-edge XANES spectra. It should be noted that for the $[Cu_3O_3]^{2+}$ and $[Cu_2AlO_3]^{2+}$ clusters in Figure 6 the spectra from S2-S4 sites were averaged (see Figures S8 and S10 in SI shows the spectra for each site). This allows a reliable comparison with experimental spectra, which likely also represent an average of slightly different locations of the clusters.

Figure 6b clearly shows that the calculated $k^2(k)$ EXAFS spectra of the $Cu_2AlO_3$ species agrees well with the experimental spectra. This can be also seen for the R-

space (Figure S9a-S9c). The simulated spectra for $[Cu_3O_3]^{2+}$ reproduce the positions of the first and second peaks very well but show higher intensities than the experiment.

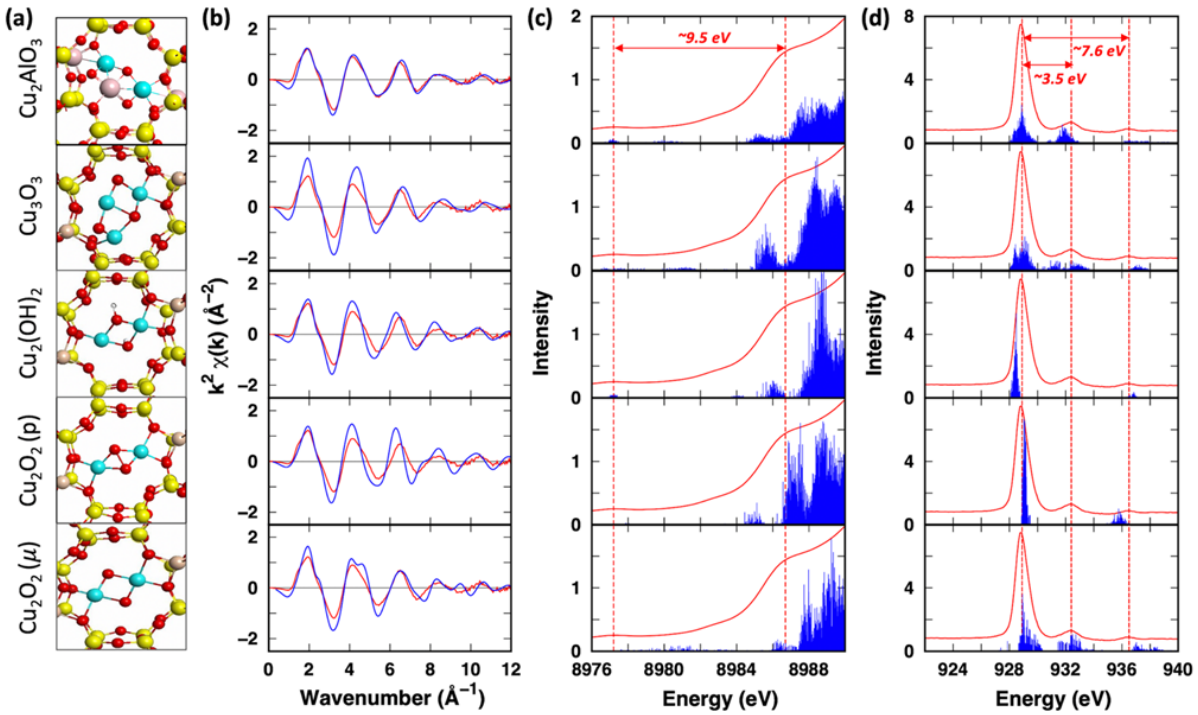


**Figure 6.** (a) annealed structure, (b) compared $k^2$-weighted EXAFS ($k^2\chi(k)$) from calculation (blue line) and measurement (red lines), (c) K-edge XANES, and (d) L3 edge XANES spectra of selected systems. For spectra of Cu trimer and $Cu_2AlO_3$, we plot ensemble averaged data with different Al and Cu cluster sites where individual spectra can be found in Figures S6 and S8. K-edge and $L_3$-edge XANES spectra are shifted by 88 and 2.1 eV respectively in order to match experimental pre-edge and main peak, and their intensities are with arbitrary units. Figure (c) and (d) compare theoretical (blue lines) spectra with experimental ones (red line) along with red vertical guiding lines and energies as shown in Figure 5a and 5b, respectively.

For the bis($\mu$-hydroxo) $[Cu(OH)_2Cu]^{2+}$ and peroxo dicopper [Cu-(*trans*-$\mu$-O)$_2$-Cu]$^{2+}$ systems, only the posit,ion and intensity of the first peak of $k^2\chi(k)$ EXAFS shows a good agreement with experimental data. The $k^2\chi(k)$ EXAFS of bis($\mu$-oxo) Cu dimer $[Cu(\mu\text{-}O)_2\text{-}Cu]^{2+}$ can be ruled out, therefore, as neither the intensity of the first peak, nor the shape of the second peak is reproduced and also scattering above $k$ = 8 Å$^{-1}$ is poorly reproducing the experimental data (Figure S8). The detailed analysis of the EXAFS peaks and their relation to the structure is compiled in Section S6 of the SI.

Analysis of K-edge and $L_3$-edge XANES simulated spectra offer further insight in the structure of the active species. Figures 6c and 6d show the simulated XANES spectra with guiding lines added to facilitate comparisons of the calculated energy difference (ΔE) with the experimental values (Figure 5 and red line in Figures 6c and 6d). The simulated K-edge XANES spectrum of $[Cu_2AlO_3]^{2+}$, $[Cu_3(\mu\text{-}O)_3]^{2+}$ and the bis($\mu$-oxo) and peroxo $[Cu\text{-}(trans\text{-}\mu\text{-}O)_2\text{-}Cu]^{2+}$ clusters show a transition at ΔE greater than 10 eV, which is attributed to the dipole allowed 1s to 4p transition, but at higher energies than the experimental value of 9.5 eV (see Figure 5).

All simulated $L_3$-edge XANES spectra show a main peak at ~929 eV, corresponding to $Cu^{2+}$ 2p to 3d dipole transitions, with distinct satellite features. Simulated $L_3$-edge XANES spectrum of $Cu_2AlO_3$ species shows transitions at ΔE = ~3.3 and ~7.8 eV, which agree well with the features observed at ΔE = ~3.5 and ~7.6 eV (Figure 5b). While the $Cu_3O_3$ structure shows a main peak and satellite peak at ΔE values similar to the $Cu_2AlO_3$ structure, the additional peak at ΔE = ~2.0 eV has not been detected in the experiment and the structure can be ruled out on this basis. For the $[Cu\text{-}(OH)_2\text{-}Cu]^{2+}$ and $[Cu\text{-}(trans\text{-}\mu\text{-}O)_2\text{-}Cu]^{2+}$, the satellite peak at ΔE = ~3.5 eV was not observed in simulated spectra. Interestingly, for the bis($\mu$-oxo) dimer, which is ruled out on the basis of the EXAFS calculations, the simulated spectra show energy differences similar to the experiment although with higher peak energies. Based on $L_3$-edge XANES, the spectra calculated for $[Cu_2AlO_3]^{2+}$ is consistent with all experimental spectra and is, therefore, concluded to be the most likely structure causing the transformation of methane to methanol; see SI (section S7 and Figure S11) for further discussion. The activation of $CH_4$ in the highly efficient Cu-MOR materials is indeed performed by a $[Cu_2AlO_3]^{2+}$ species with the structure shown in Figure 6a top. The data suggest that the formation of such $[Cu_2AlO_3]^{2+}$ clusters requires the presence of extra-framework alumina at the bottom of the side pocket (i.e., not accessible for pyridine).

## 3.5 Conclusion

A series of Cu-MOR catalysts with an unprecedently high fraction of Cu being active in selective methane oxidation to methanol has been synthesized. The activity to form oxidized molecules in a stepwise reaction combined with characterization by NMR, IR, and X-ray absorption spectroscopy point to the formation of Cu-Al clusters in the 8-MR side pockets, linking exchanged $Cu^{2+}$ species with extra-framework Al moieties that were originally located at the bottom of the side pocket of MOR.

The combined experiment and simulation of Cu K and $L_3$ XANES together with EXAFS spectra allows unequivocally identifying the oxide clusters to consist of two Cu and one Al atom linked by oxygen (Figure 6a). This cluster is located in the side pocket and shows the ability to oxidize 1.2 methane molecules on average when exposed to 1 bar methane. Therefore, the amount of $CH_4$ activated per Cu in these materials corresponds to the utilization of one to up to two O atoms per cluster, analogous to the variations in reactivity observed for $\mu$-oxo species in $[Cu_3O_3]^{2+}$ clusters with chemical potential.[22] However, the presence of a minority species cannot be ruled out, a highly active Cu-oxo cluster with $Cu_{eff} > 0.5$, that could also account for the excess of $CH_4$ activated.

At present, one can only speculate about the reason for the higher reactivity of the oxygen or the easier reducibility of $Cu^{2+}$ in the $[Cu_2AlO_3]^{2+}$ cluster. One of the currently preferred hypotheses is that the distortion of the cluster decreases the stability of the Me-O bond strength. Detailed calculations on the chemical reactivity are currently being performed, but the discussion of these aspects is beyond the scope of the current study.

## 3.6 Acknowledgement

The financial support from the Deutsche Forschungsgemeinschaft (DFG, Project number 326562156) and the TUM International Graduate School of Science and Engineering (IGSSE) is acknowledged. Part of this work was supported by the U.S. Department of Energy (DOE), Office of Science, Office of Basic Energy Sciences, Division of Chemical Sciences, Geosciences and Biosciences (Transdisciplinary Approaches to Realize Novel Catalytic Pathways to Energy Carriers, FWP 47319). Computational work was performed using the Molecular Sciences Computing Facility (MSCF) in the William R. Wiley Environmental Molecular Sciences Laboratory, a US Department of Energy (DOE) national scientific user facility sponsored by the DOE's Office of Biological and Environmental Research and located and the Pacific Northwest National Laboratory (PNNL) and the National Energy Research Scientific Computing Center (NERSC) located at Lawrence Berkley National Laboratory provided by a user proposal. PNNL is operated by Battelle for DOE. The author further acknowledges Paul Scherrer Institut (Villigen, Schweiz) for the provision of synchrotron beamtime at PHOENIX of the SLS and DESY beamlines P-64 and P-65 (Hamburg, Germany), a member of the Helmholtz Association HGF, for the provision of experimental facilities for X-ray experiments. The used infrastructure of the von Hamos spectrometer at the beamline P64 was realized in the frame of projects FKZ 05K13UK1 and FKZ 05K14PP1. The author thanks Xaver Hecht for his support in the laboratory. The author thanks Matthias Bauer for his assistance with XAS discussions.

## 3.7 Appendix

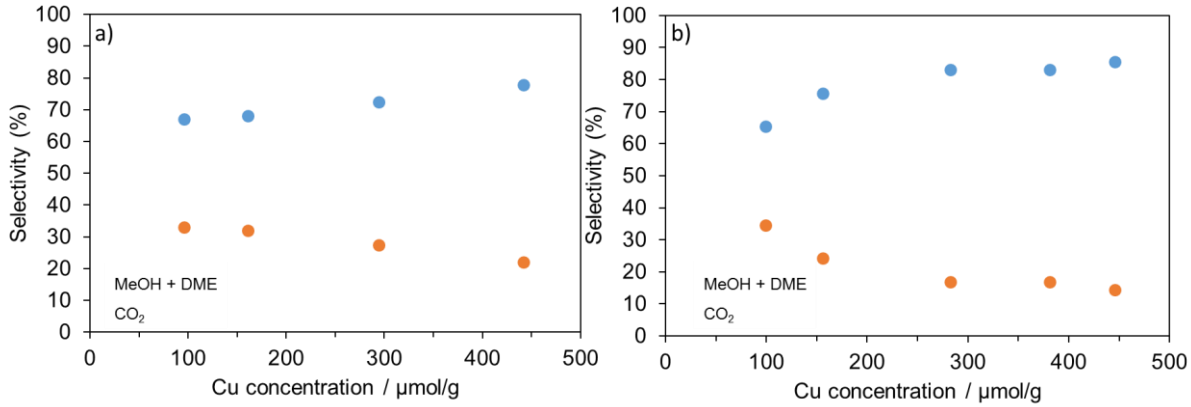


**Figure S1.** Selectivity of $CH_4$-oxidation reaction on a) Cu-MOR-A and b) Cu-MOR-B catalysts towards MeOH+DME (blue) and $CO_2$ (orange). DME is considered as the condensation of two MeOH molecules.

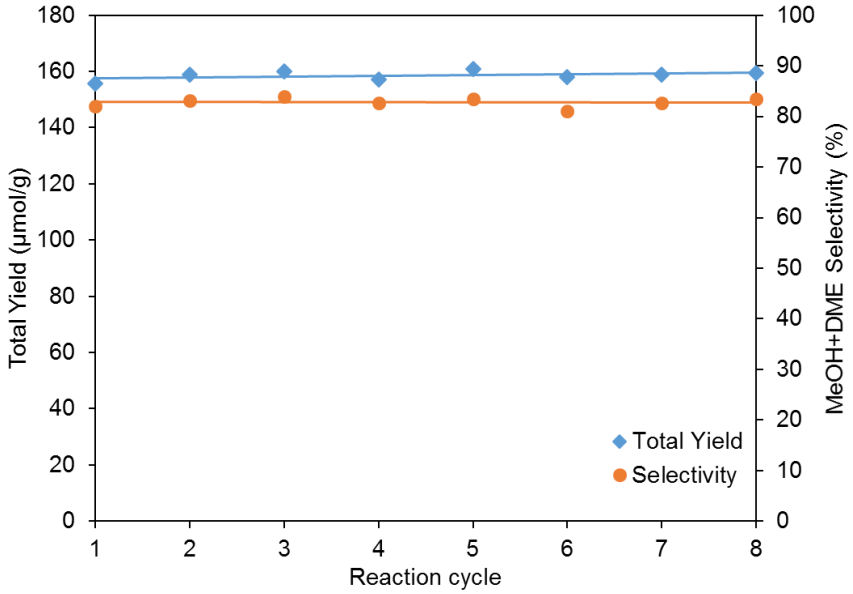


**Figure S2.** The total yield of $CH_4$ oxidation (blue) on CuMOR-B-280 for selective partial oxidation of methane over 8 cycles with the corresponding selectivity towards MeOH+DME (orange). DME is considered as the condensation of two MeOH molecules. The catalyst has been recycled over 8 cycles with activation at 500 °C for 1h in $O_2$, methane reacted at 200 °C for 4h, and steam treated at 135 °C for 1h.

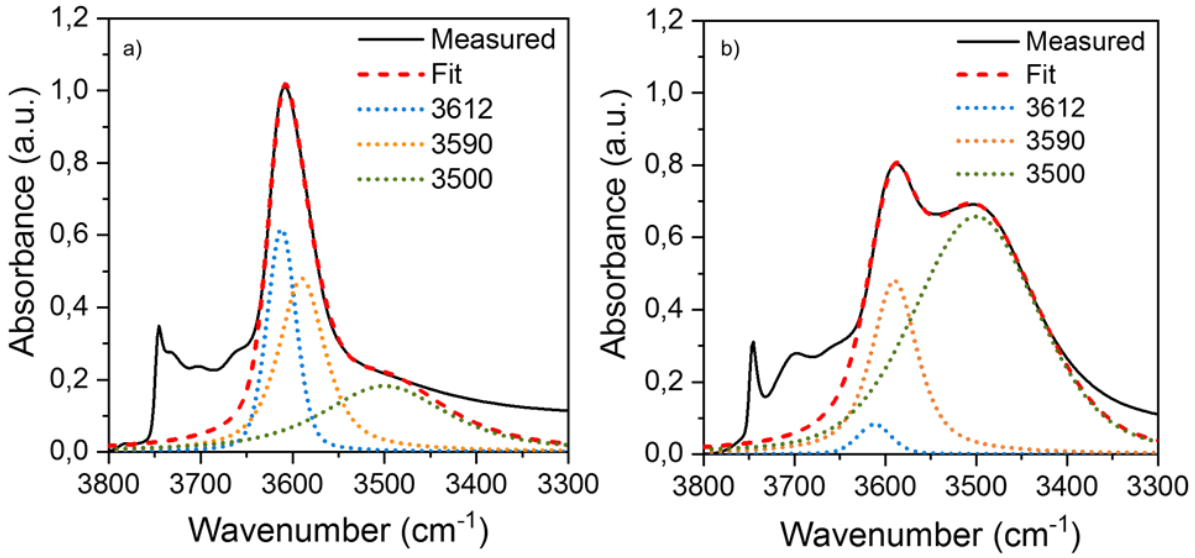


**Figure S3.** Deconvolution of IR spectra of H-MOR-*B* before adsorption of *n*-hexane (a) and after adsorption of *n*-hexane at 1.0 mbar (b)

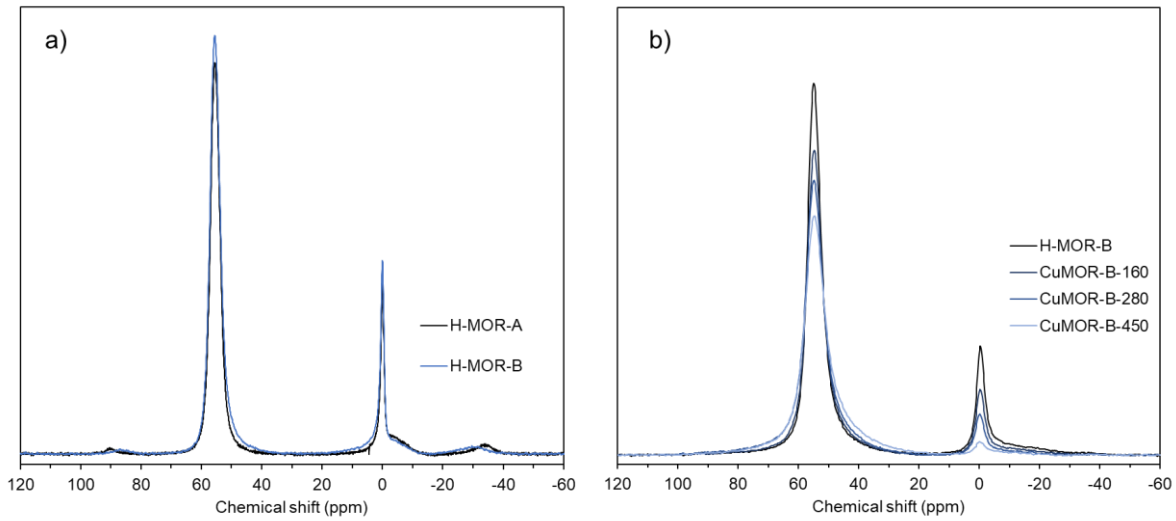


**Figure S4.** $^{27}$Al-NMR spectra of a) of parent H-MOR-A and H-MOR-B (900 MHz instrument) and b) hydrated Cu-MOR-B series with different Cu loadings (500 MHz instrument).

## Cu K edge and L edge XANES spectra

Cu K edge XANES spectra of Cu-MOR-B-280 sample is provided herein Figure S5a for comparison with the HERFD-XANES spectra (Figure 5a) in the main text. It should be noted that a conventional XANES measurement is a projection of a resonant inelastic scattering (RIXS) measurement onto the incident X-ray energy axis, while a

HERFD-XANES measurement, on the other hand, is a slice along the RIXS plane. The width of the peaks in the former are mostly determined by the 1s core-hole lifetime, while the widths of the peaks in the latter are determined by the 2p lifetime resulting in sharper spectral features.

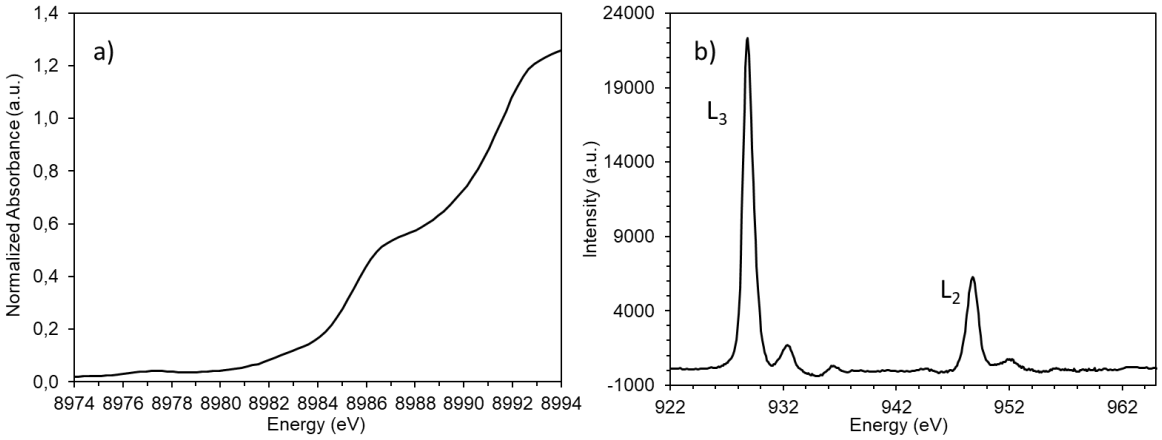


**Figure S5.** a) Conventional Cu K-edge b) XANES and Cu $L_{3,2}$-edge measurement of $O_2$ activated (at 500 °C) Cu-MOR-B with c(Cu) = 283 µmol/g.

**Table S1.** Properties of H-MOR-A and H-MOR-B

| | **H-MOR-A** | **H-MOR-B** |
|---|---|---|
| Total Al (elemental analysis) | 1440 µmol/g | 1620 µmol/g |
| Framework Al (Na-exchange) | 1070 µmol/g (74%) | 1130 µmol/g (78%) |
| BAS (IR spectroscopy) | 1090 µmol/g (76%) | 1130 µmol/g (76%) |
| Al pairs ($Co^{2+}$-exchange) | 63% | 66 % |
| $Al_{tetrahedral}$ | 1156 µmol/g (80%) | 1290 µmol/g (80%) |
| $Al_{octahedral}$ | 284 µmol/g (20%) | 330 µmol/g (20%) |

**Table S2.** Si/Al ratios of Cu-MOR-B catalysts and Cu concentrations before and after Na back-exchange, as determined by elemental analysis.

| Sample | Cu concentration (μmol/g) | Si/Al after Cu-exchange (-) | Cu concentration after Na back-exchange (μmol/g) | Not back-exchanged Cu (%) |
|---|---|---|---|---|
| **CuMOR-100** | 99 | 9.6 | 6.3 | 6.4 |
| **CuMOR-150** | 155 | 9.4 | 10 | 6.4 |
| **CuMOR-280** | 283 | 9.3 | 20 | 7.0 |
| **CuMOR-380** | 381 | 10.2 | 25 | 6.6 |
| **CuMOR-450** | 446 | 9.4 | 32 | 7.1 |

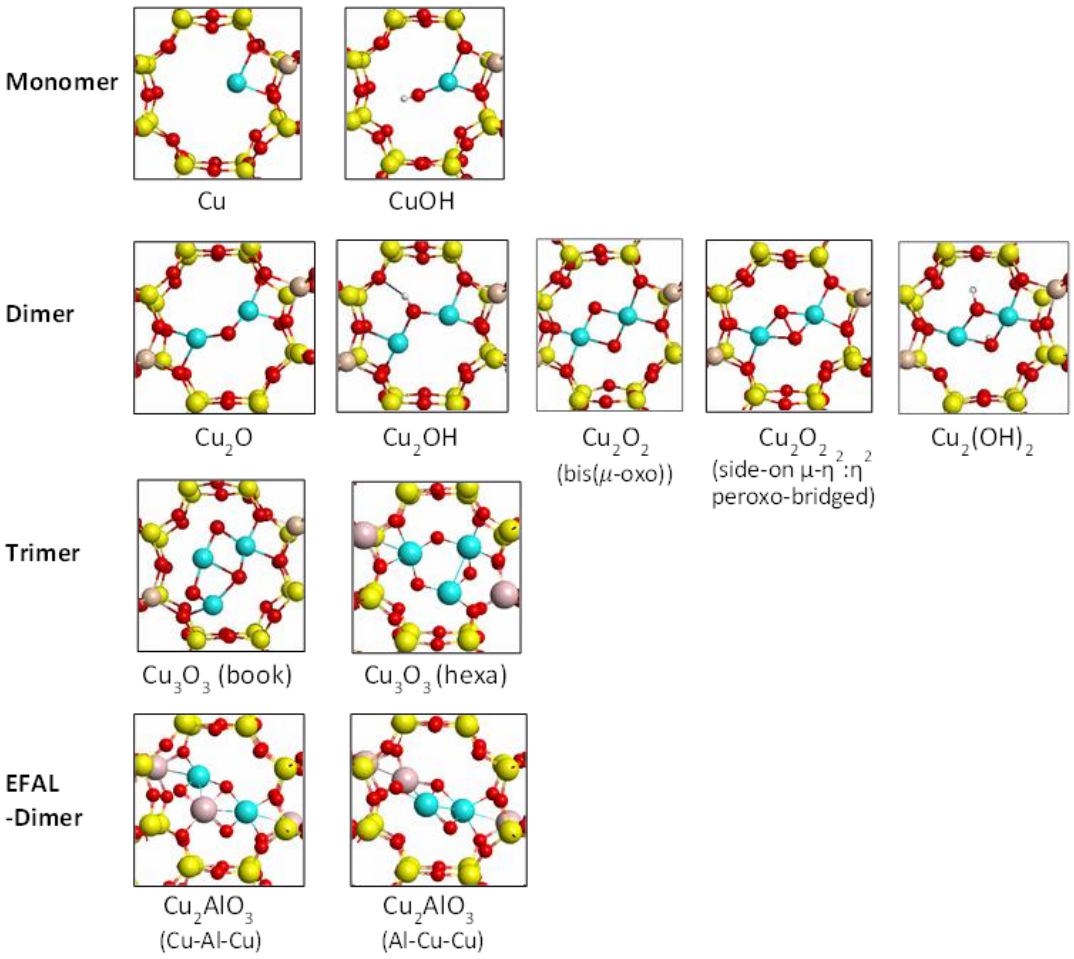


**Figure S6.** List of Cu cluster models and top view (xy plane) snapshots extracted from AIMD simulations. Color codes: Si-yellow, Al-pink, Cu-Cyan, O-red, H-white.

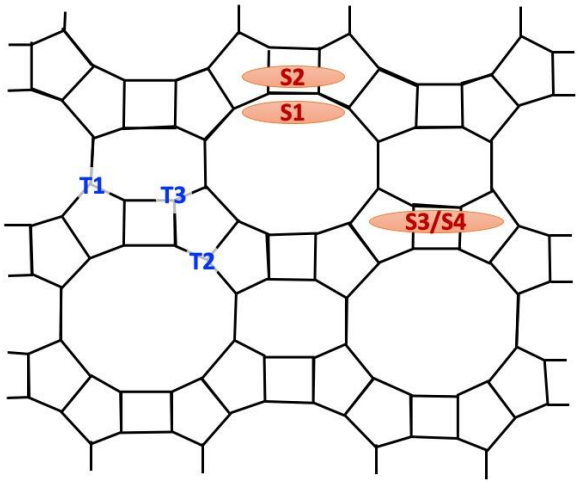


**Figure S7.** Schematic illustration of Cu cluster sites (S1-S4) having different occupied locations (12 MR or 8-MR side pocket) of the cluster and T site(s) (T1-T3) of Al atom(s).

**Table S3.** Systems studied with AIMD simulations

| | | Site 1 | Site 2 | Site 3 | Site 4 |
|---|---|---|---|---|---|
| Cu monomers | Cu | o (→ S2) | | | |
| | CuOH | o (→ S2) | | | |
| Cu dimers | $Cu_2O$ | o | o | | |
| | $Cu_2OH$ | o | | | |
| | $Cu_2O_2$ bis($\mu$-oxo) | o (→ S2) | o | o (→ peroxo) | |
| | $Cu_2O_2$ (peroxo) | o | o | o | o |
| | $Cu_2(OH)_2$ | o | o | o | |
| Cu trimers | hexagonal | | | o | |
| | book-like | o | o | o | o |
| Cu-Al clusters | Cu-Al-Cu | o | o | o | o |
| | Al-Cu-Cu | o | o | o | |

## Structural changes during AIMD simulations

Several of the optimized structures on the potential energy surface rapidly isomerized during the equilibration period within 1.05 ps of > 35 ps of AIMD simulations. For instance: i) the Cu monomer (Cu and CuOH) and bis(*μ*-oxo) dicopper change from site S1 to S2, ii) the bis(μ-oxo) dicopper at site S3 transformed to peroxo structure, (iii) the initial μ-1,2-peroxo structure of peroxo dicopper transformed to side-on μ-η2:η2 peroxo-bridged structure (see Figure S4), and iv) the initial hexagonal structure (denoted as hexa) of the $[Cu_3(\mu\text{-}O_3)]^{2+}$ cluster transformed to open-book-like structure (denoted as book).

### I. Cu-monomer

a. Cu at S2 site with Al on T2 site

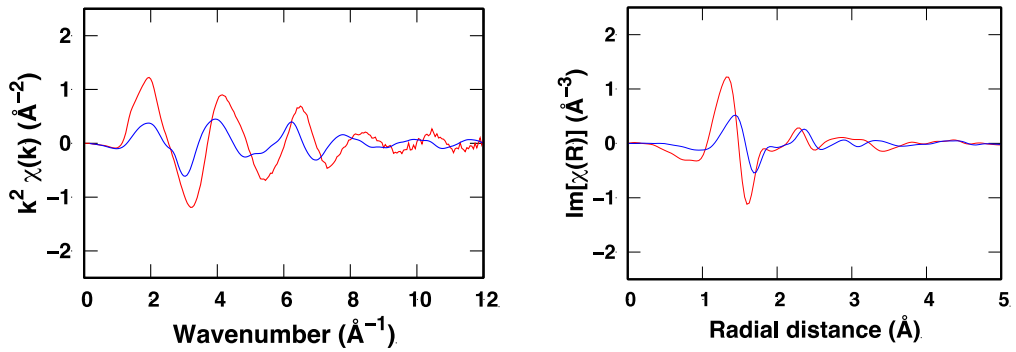


b. CuOH at S2 site with Al on T2 site

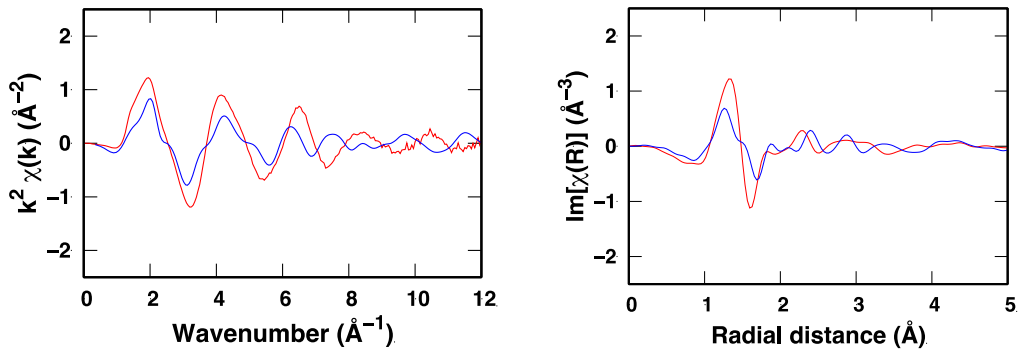

## II. Cu-dimer

a. $[Cu\text{-}(\mu\text{-}O)\text{-}Cu]^{2+}$

- S1 site with Al on T2 sites

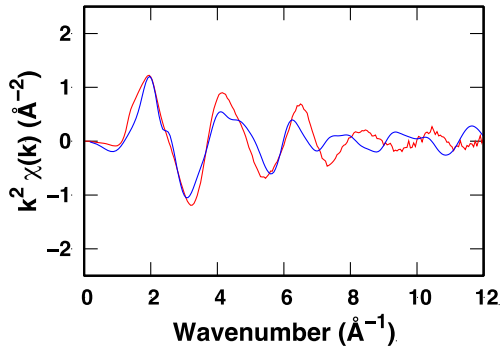


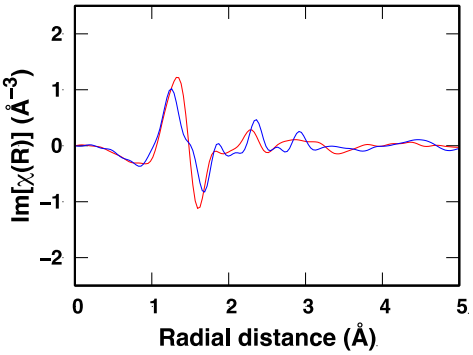


- S2 site with Al on T2 sites

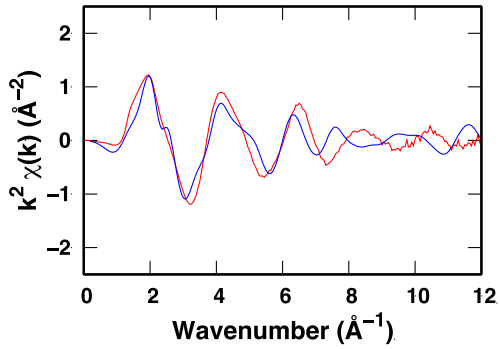


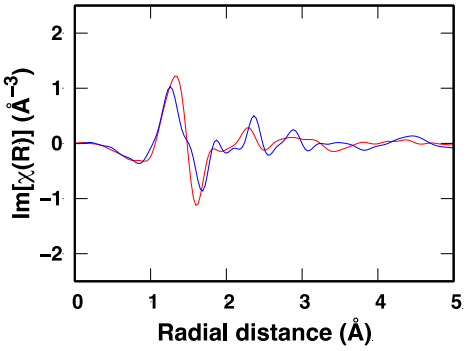


b. $[Cu\text{-}(OH)\text{-}Cu]^{2+}$ at S1 site with Al on T2 sites

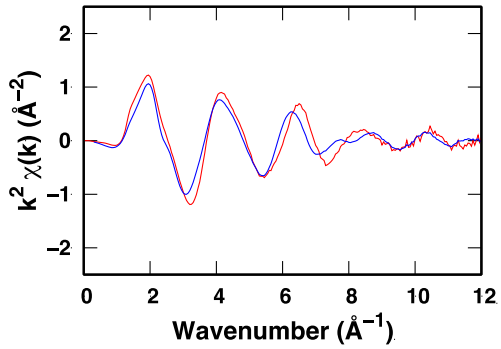


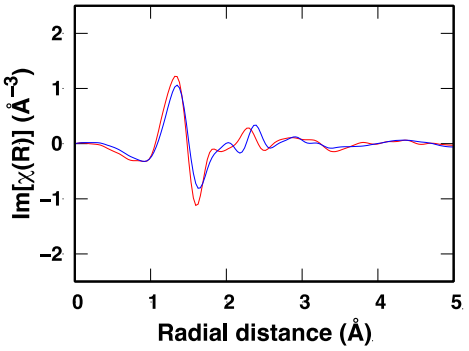

c. $[Cu\text{-}(\mu\text{-}O)_2\text{-}Cu]^{2+}$ at S2 site with Al on T2 sites

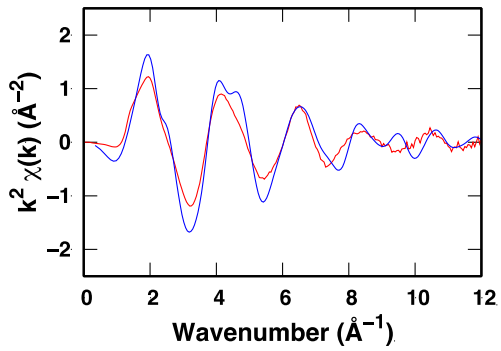


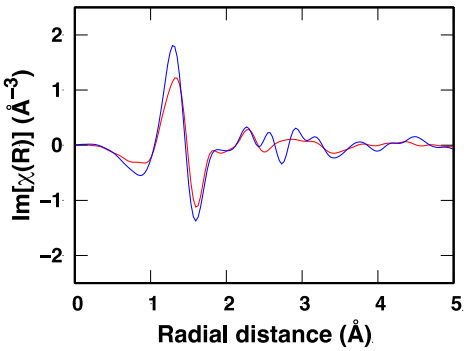


d. $[Cu\text{-}(\textit{trans}\text{-}\mu\text{-}O)_2\text{-}Cu]^{2+}$

- S1 site with Al on T2 sites

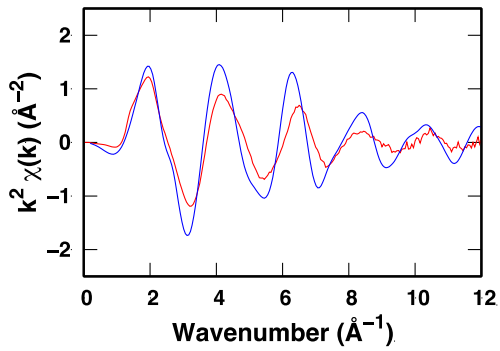


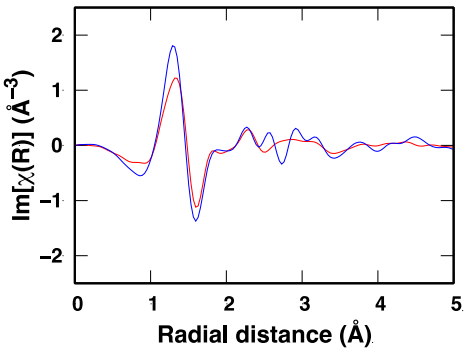


- S2 site with Al on T2 sites

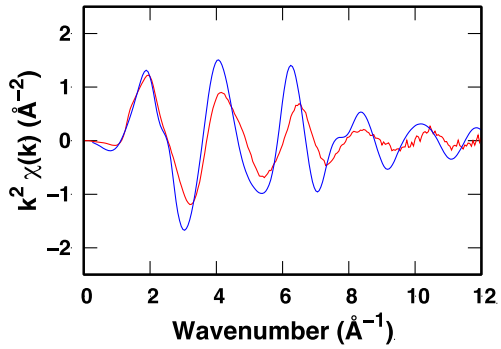


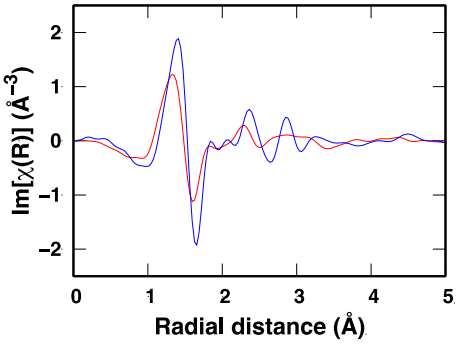

- S3 site with Al on T1 sites

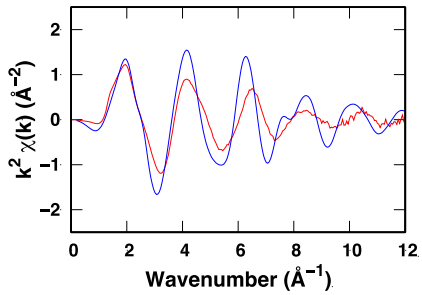


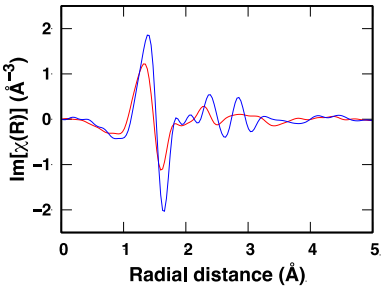


- S3 site with Al on T3 sites

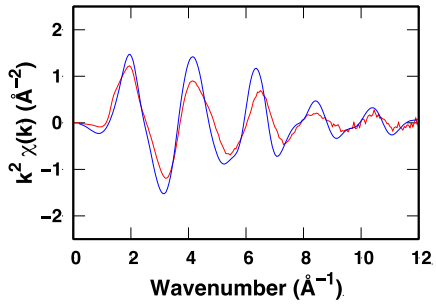


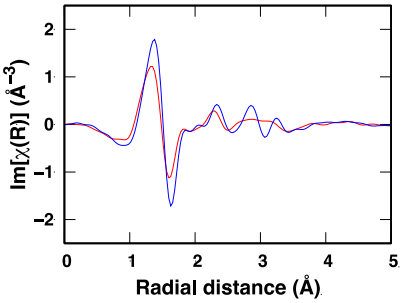


e. $[Cu\text{-}(OH)_2\text{-}Cu]^{2+}$

- S1 site with Al on T2 sites

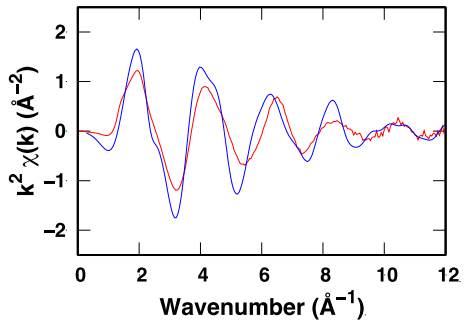


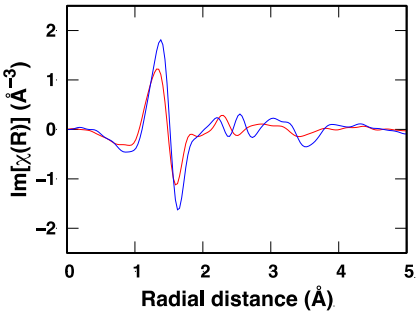


- S2 site with Al on T2 sites

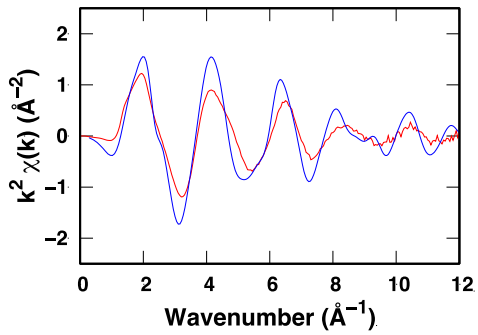


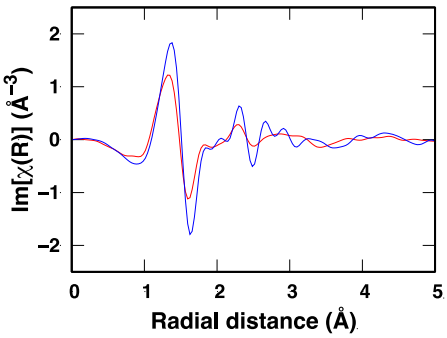

- S3 site with Al on T1 sites

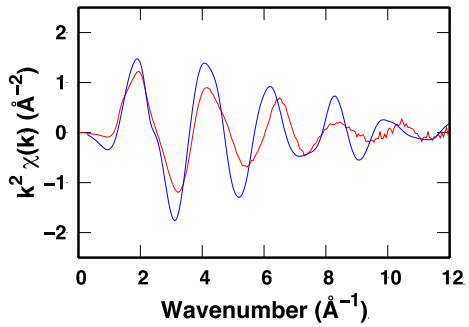


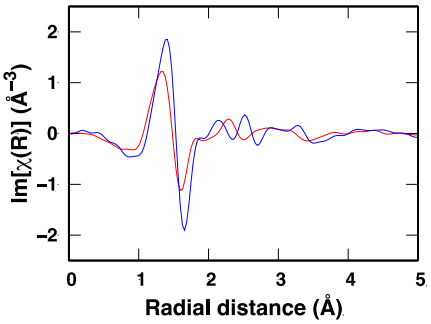


**III. Cu-trimer**

a. book-like $[Cu_3(\mu\text{-}O)_3]^{2+}$

- S2 site with Al on T2 sites

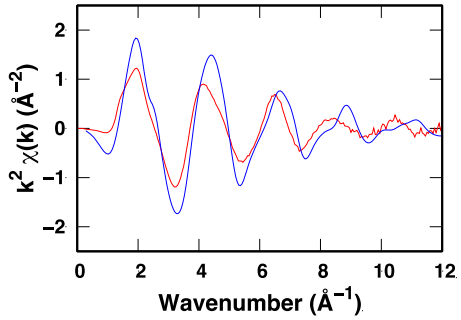


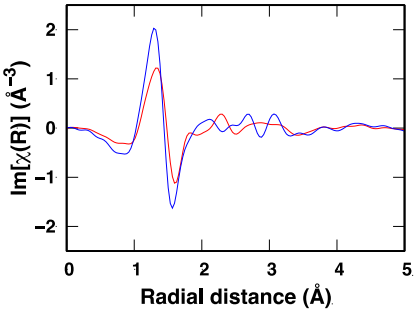


- S3 site with Al on T1 sites

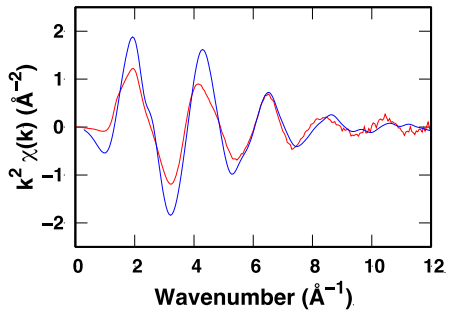


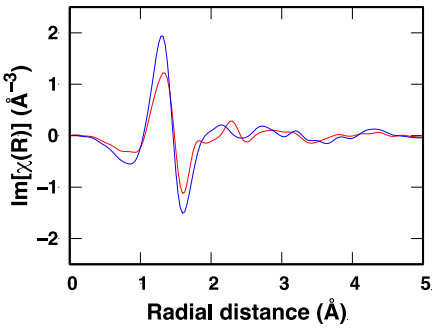

- S4 site with Al on T3 sites

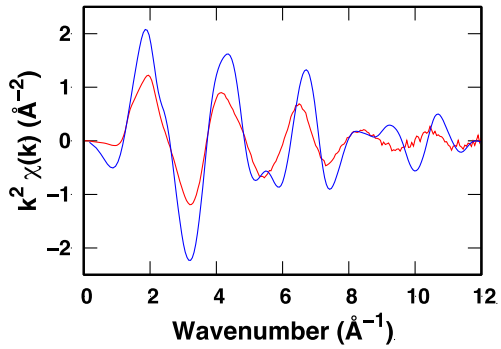


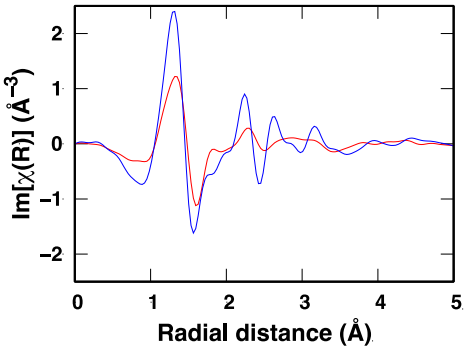


b. hexagonal $[Cu_3(\mu\text{-}O)_3]^{2+}$ at S3 site with Al on T1 sites

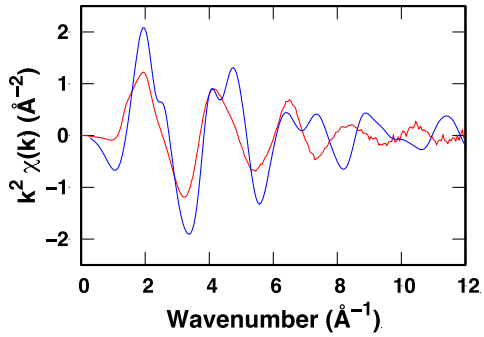


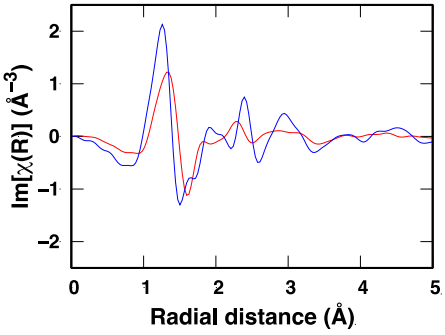


## IV. Cu-Al clusters

a. $[Cu_2AlO_3]^{2+}$ (Cu-Al-Cu)

- S1 site with Al on T2 sites

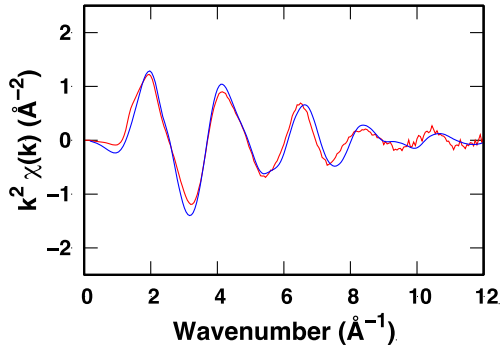


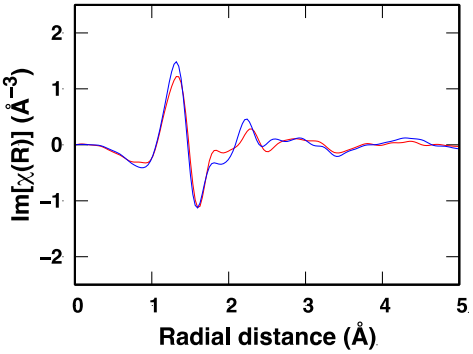


- S2 site with Al on T2 sites

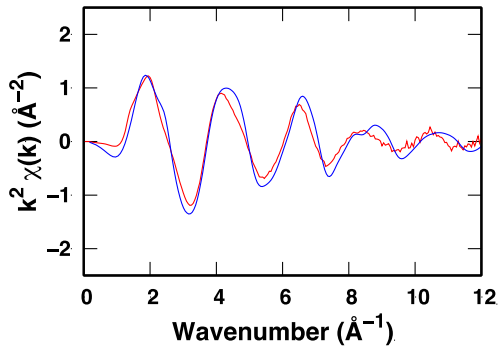


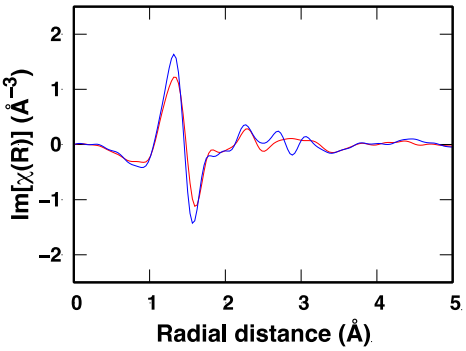

- S3 site with Al on T1 sites - a

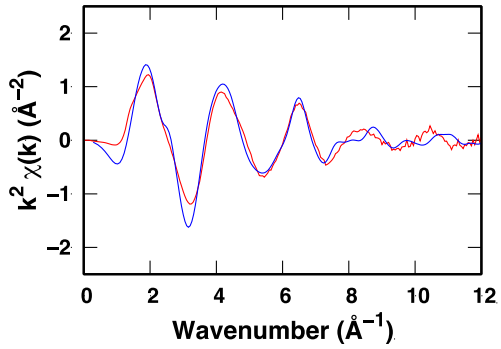


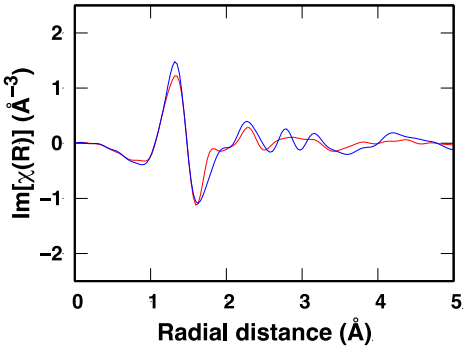


- S3 site with Al on T1 sites - b

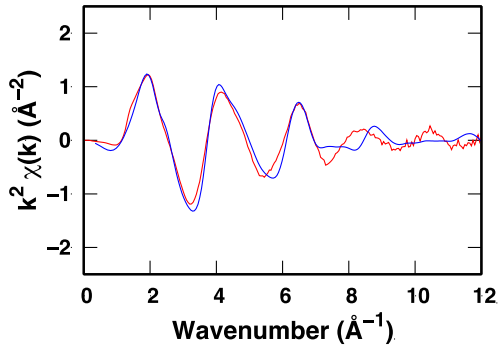


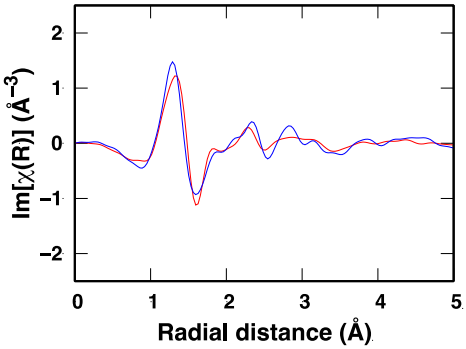


- S4 site with Al on T3 sites – a

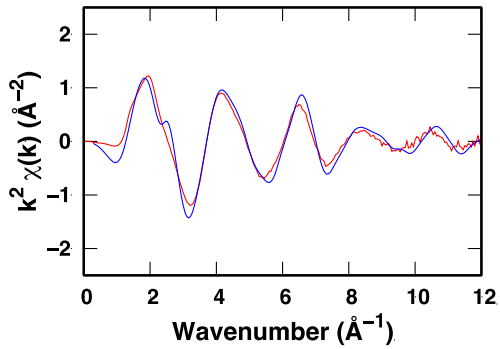


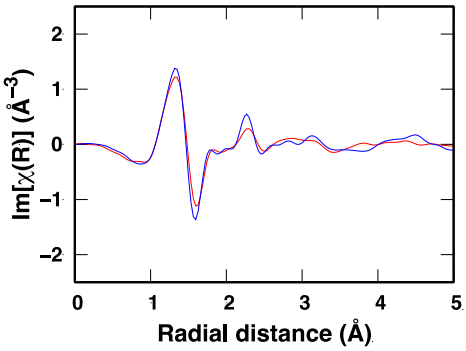


- S4 site with Al on T3 sites – b

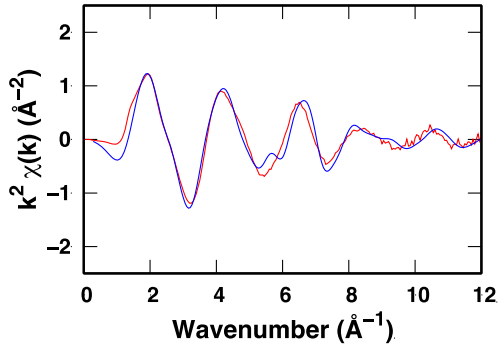


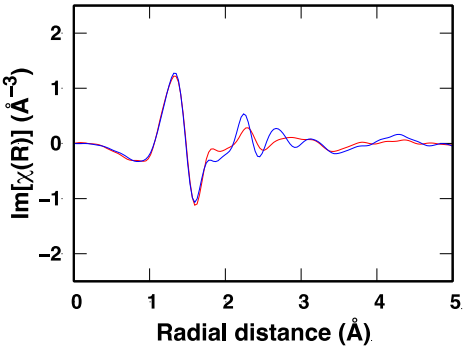

b. $[Cu_2AlO_3]^{2+}$ (Al-Cu-Cu)

- S1 site with Al on T2 sites

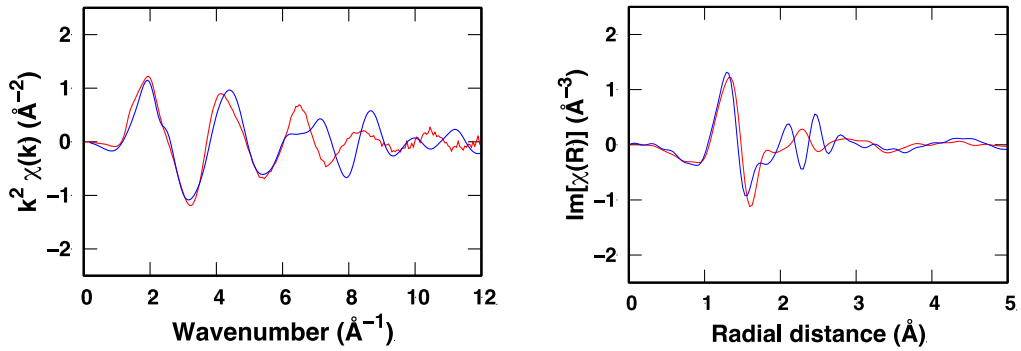


- S2 site with Al on T2 sites

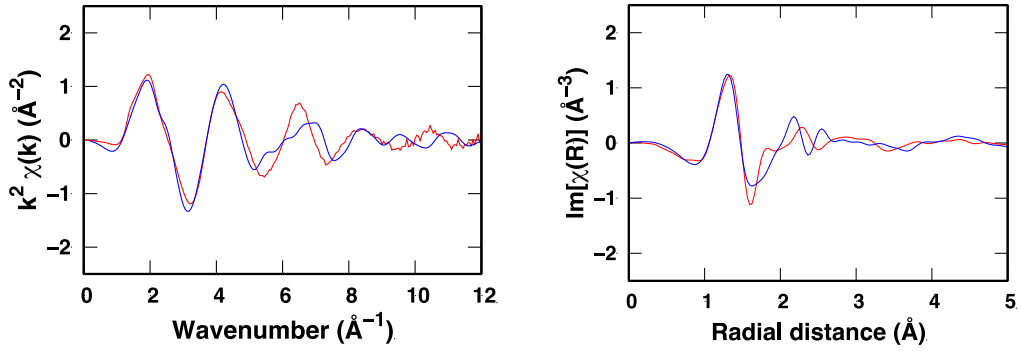


- S3 site with Al on T1 sites

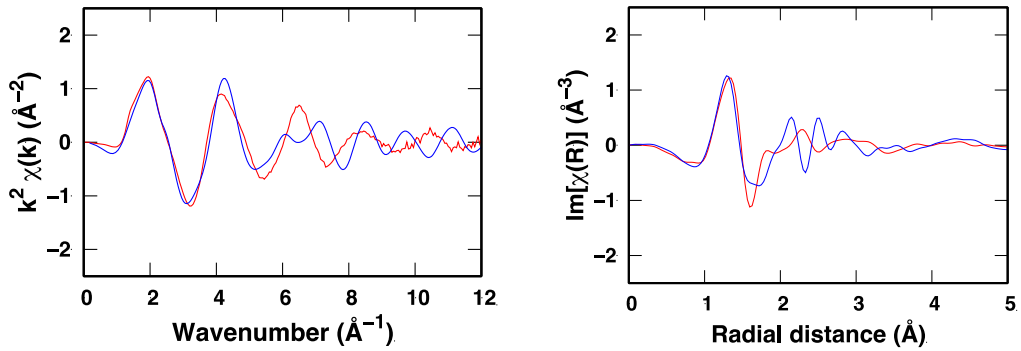


**Figure S8.** Comparison of the $k^2$-weighted EXAFS ($k^2(k)$) (left panel) and the imaginary part of the corresponding $k^2$-weighted Fourier transformed EXAFS (Img[$\bar{\chi}(k)$]) (right panel) for EFAl Cu dimer systems. Color key: red for measured spectra and blue for calculated spectra using extracted structures from AIMD simulations.

## A detailed analysis of the EXAFS peaks and their relation to the structures

To understand differences observed from EXAFS, we calculated radial distribution functions, g(R), which show average distances between two species, see Figure S9. By comparing g(R) and |$\chi$ (R)|, we can deduce the origin peak in |$\chi$ (R)|. The peaks in R-space spectra (Figure S9a-S9c) are directly associated to the distance from Cu atom to others.

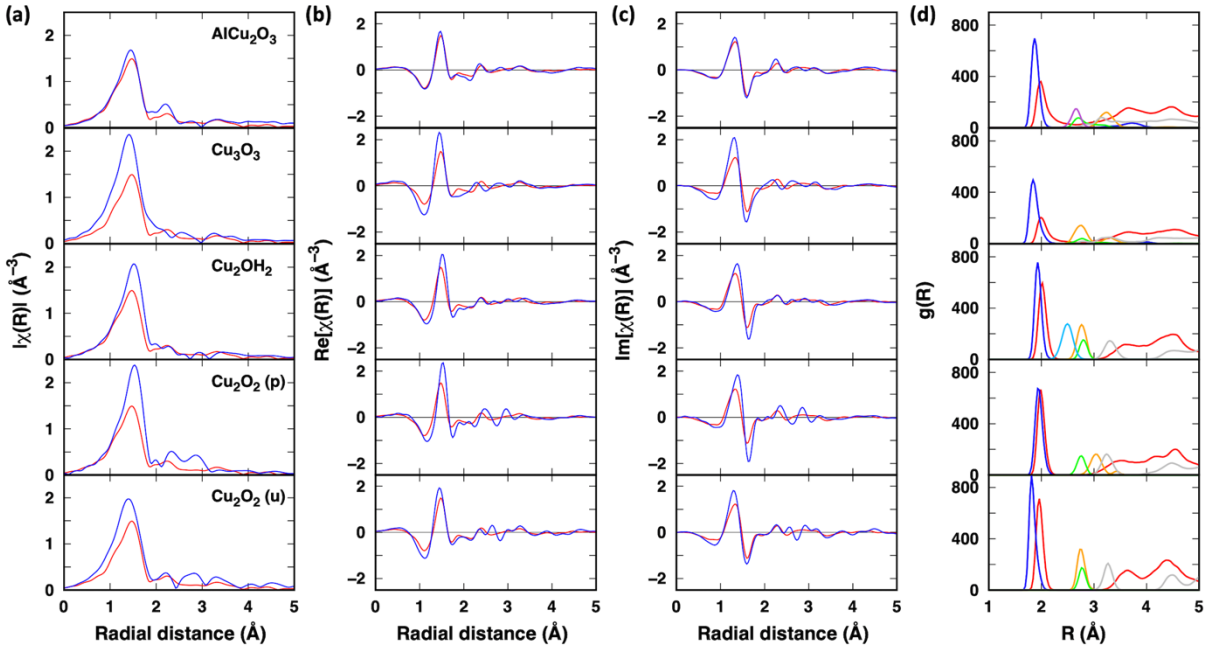


**Figure S9.** Ensemble averaged R-space EXAFS showing magnitude (a), real part (b), imaginary part (c), and radial distribution function showing the average distance between two species (d) for dimer, trimer, and $Cu_2AlO_3$ systems. Color key: (a-c) red for measured spectra and blue for calculated spectra using extracted structures from AIMD simulations, (d) red for Cu-$O_{mor}$, blue for Cu-$O_{oxo}$, orange for Cu-Cu, green for Cu-Al, gray for Cu-Si, violet for Cu-EFAl, and sky blue for Cu-H.

The highest peak below 2 Å is consistent with known backscattering the from nearest neighbor Cu-O bond. Comparing with the experimental peak at ~1.6 Å, the peak in $Cu_2AlO_3$ shows nearly the same value. This peak in $Cu_3O_3$ and bis($\mu$-oxo) dicopper clusters is shifted to lower values while the peak in bis($\mu$-hydroxo) and perodicopperers are shifted to higher values. the In g(R) plot, Cu-$O_{oxo}$ (blue lines) shows the shortest distance. Compared with Cu-$O_{oxo}$ distance in $Cu_2AlO_3$, those of $Cu_3O_3$ and bis($\mu$-oxo) dicopper clusters indeed are shorter while those of bis($\mu$-hydroxo) and peroxodicoppers are longer. The major difference between these five systems can be

seen in two peaks at ~2.3 and ~2.8 Å in R-space spectra. The peak at ~2.3 Å shown in the experimental spectra is consistent with known Cu-Al distances. The $Cu_2AlO_3$ and bis($\mu$-oxo) dicopper spectra show a strong and well resolved peak while the others show either a weak or no peak. In the g(R), the $Cu_2AlO_3$ shows overlapping peaks between Cu and framework Al (green line), and Cu and extra-framework Al (violet line) at ~2.8 Å.

Likewise, the g(R) of the bis($\mu$-oxo) dicopper shows the mixture of Cu-Al and Cu-Cu peaks at 2.8 Å. As a result, both systems show a strong peak at ~2.3 Å in simulated R-spectra. For the Cu-Cu distances the experimental Rspacespectrashowss a peak at ~2.8 Å. The $Cu_2AlO_3$ and bis($\mu$-oxo) dicopper spectra both show a peak at ~2.8 Å, which is seen as a peak at ~3.2 Å in the Cu-Cu g(R) (orange line), as seen in the experiment. However, only $Cu_2AlO_3$ shows similar intensity compared with experiment. Thus, the $Cu_2AlO_3$ is the only model which exhibits a structure consistent with experimental EXAFS.

**I. Cu trimer**

a. book-like $[Cu_3(\mu\text{-}O)_3]^{2+}$

- S2 site with Al on T2 sites

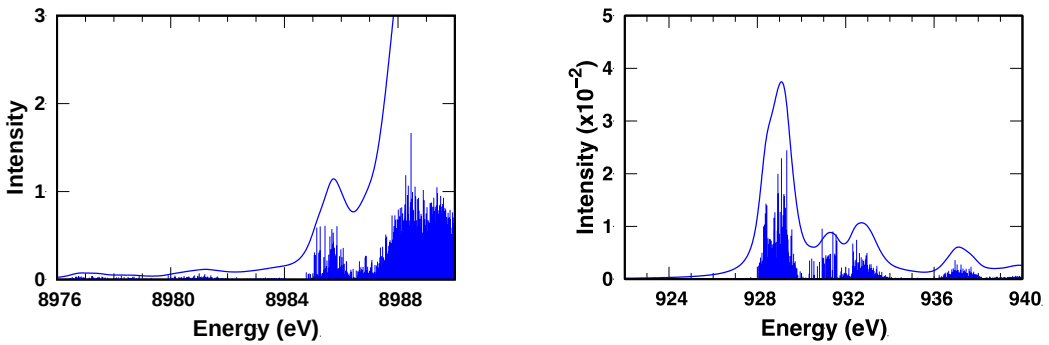


- S3 site with Al on T1 sites

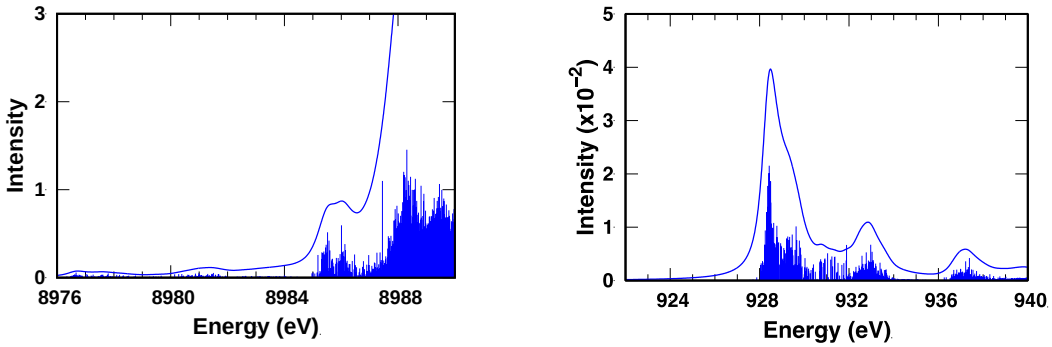

- S3 site with Al on T3 sites

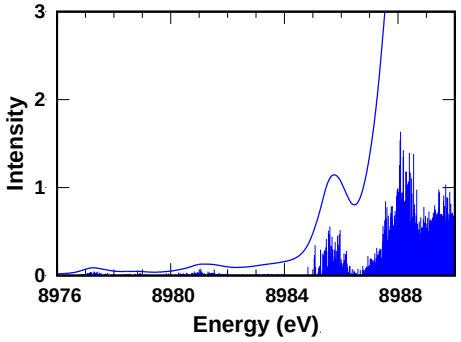


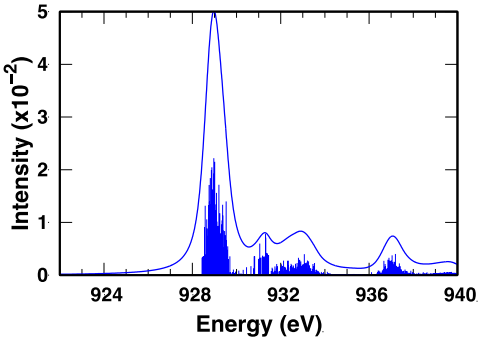


b. hexagonal $[Cu_3(\mu\text{-}O)_3]^{2+}$ at S3 site with Al on T1 sites

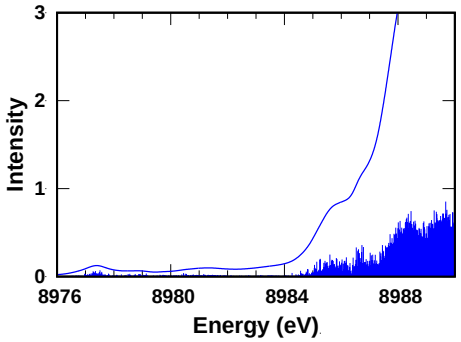


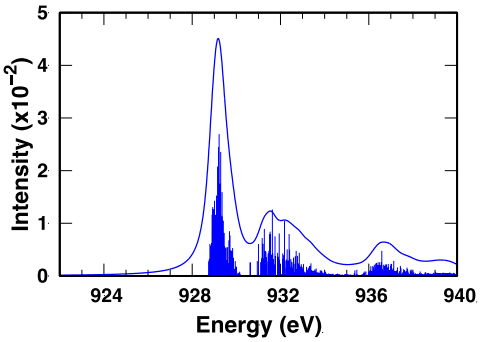


**II. $Cu_2AlO_3$ (Cu-Al-Cu)**

- S2 site with Al on T2 sites

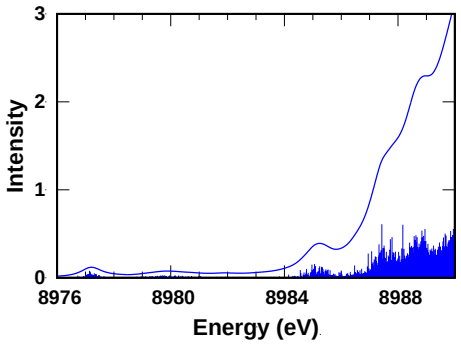


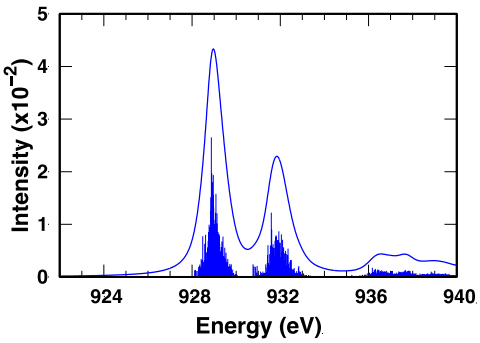


- S3 site with Al on T1 sites

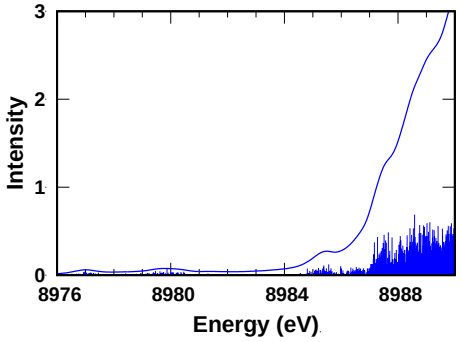


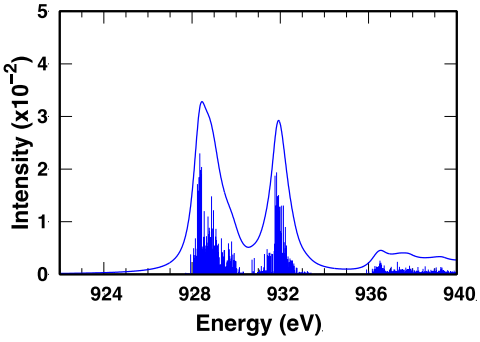

- S4 site with Al on T3 sites

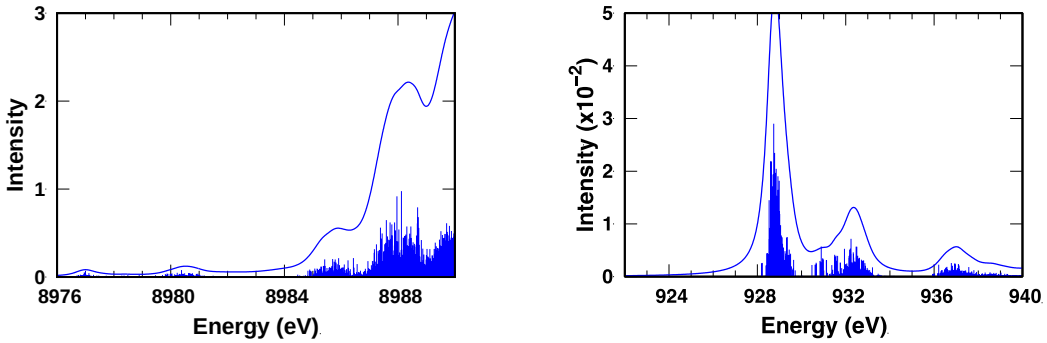


**Figure S10.** Simulated Cu K- and $L_3$-edge XANES spectra of selected Cu-cluster systems where bar lines are discrete roots before Lorentzian line broadening. Calculated spectra are obtained using extracted structures from AIMD simulations.

## Tri-coordinated Cu on $Cu_2AlO_3$

Dynamic changes in the structural features of the $Cu_2AlO_3$ cluster affect the observed peaks in both K- and $L_3$-edge XANES as shown in Figure S11. By comparing spectra obtained over different simulation times, the system shows the growth of a shoulder at ~8987 eV in the K-edge XANES, see arrows in the left panel of Figure S11. In the $L_3$-edge XANES, a change in the intensity is more significant at the main peak at ~929 eV, see arrows in the middle panel of Figure S11. From a visualization of the trajectory using VMD,[74] Cu atoms dynamically interconvert between 3 and 4 coordinate geometries, where only one Cu atom (denoted as Cu1 in Figure S11) is primarily responsible for this change. By calculating contributions of each Cu atom on the spectra (Figure S11), it can be seen that the changes of the intensities are strongly influenced by the configuration of Cu1. This observation is supported by the Cu-O coordination number (CN) calculated over different simulation times (at 35 and 150 ps, the total simulation time), see the right panel of Figure S11. This results from the change in CN between 3 and 4 of Cu1 which occurs approximately 10 times in 150 ps time period. Hence, sampling is significantly better at 150 ps (10 crossings) as opposed to 35 ps (2 crossings). The figure clearly shows that 3 CN is significantly increased for Cu1, while Cu2 mostly shows 4 CN regardless of the time period. Therefore, the differences in relative intensity, but not frequency, between the main peak and the satellite in the $L_3$ edge are significantly affected by this change in CN of Cu1.

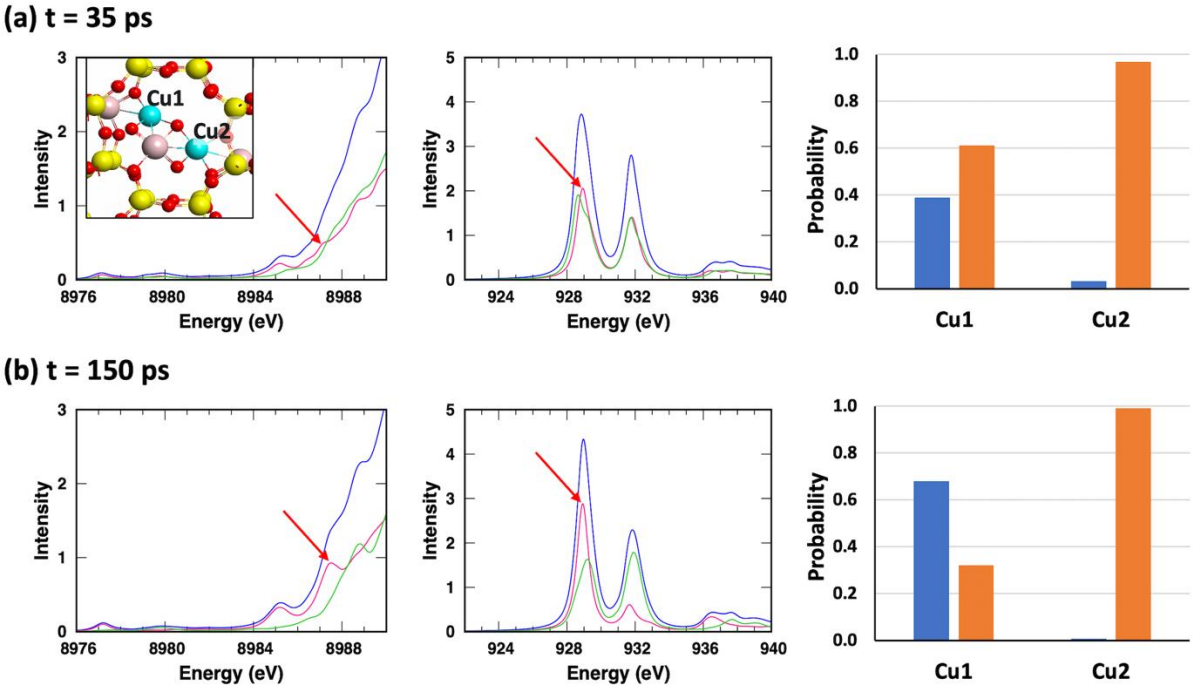


**Figure S11.** Time-function analysis of K-edge (left panel) and $L_3$-edge XANES (middle panel), and Cu-O coordination number (CN) (right panel) of $Cu_2AlO_3$ system in the site S2. XANES spectra show the contribution of each Cu atom (blue line for total, red line for Cu1, and green line for Cu2), where arrows show the change of intensity with changed simulation time. The CN plots show the probability of 3 (blue bar) and 4 CN (orange bar) for each atom during the calculated time period.

For a configuration with tri-coordinated Cu1, the simulated spectra show, similar to the experimental spectra, ~10 times higher intensity of the main peak than that of the satellite peak. In the Cu K-edge XANES, there is an increase in the feature at ΔE = ~10 eV for the Cu in 3 CN configuration.

## 3.8 References


1. A. Caballero, P. J. Perez, Methane as raw material in synthetic chemistry: the final frontier. *Chem. Soc. Rev,* (2013), **42**, 8809-8820.

2. M. C. Alvarez-Galvan *et al.*, Direct methane conversion routes to chemicals and fuels. *Catal. Today,* (2011), **171**, 15-23.

3. M. A. Newton, A. J. Knorpp, V. L. Sushkevich, D. Palagin, J. A. van Bokhoven, Active sites and mechanisms in the direct conversion of methane to methanol using Cu in zeolitic hosts: a critical examination. *Chem. Soc. Rev,* (2020), **49**, 1449-1486.

4. D. Malakoff, The gas surge. *Science,* (2014), **344**, 1464.

5. G. A. Olah, Beyond Oil and Gas: The Methanol Economy. *Angew. Chem., Int. Ed.,* (2005), **44**, 2636-2639.

6. Y. Ma *et al.*, Low-Temperature Solid-State Ion-Exchange Method for Preparing Cu-SSZ-13 Selective Catalytic Reduction Catalyst. *ACS Catal.,* (2019), **9**, 6962-6973.

7. M. Ravi, M. Ranocchiari, J. A. van Bokhoven, The Direct Catalytic Oxidation of Methane to Methanol—A Critical Assessment. *Angew. Chem., Int. Ed.,* (2017), **56**, 16464-16483.

8. M. H. Groothaert, J. A. van Bokhoven, A. A. Battiston, B. M. Weckhuysen, R. A. Schoonheydt, Bis(μ-oxo)dicopper in Cu-ZSM-5 and Its Role in the Decomposition of NO: A Combined in Situ XAFS, UV−Vis−Near-IR, and Kinetic Study. *J. Am. Chem. Soc.,* (2003), **125**, 7629-7640.

9. M. B. Park, S. H. Ahn, A. Mansouri, M. Ranocchiari, J. A. van Bokhoven, Comparative Study of Diverse Copper Zeolites for the Conversion of Methane into Methanol. *ChemCatChem,* (2017), **9**, 3705-3713.

10. M. H. Groothaert, P. J. Smeets, B. F. Sels, P. A. Jacobs, R. A. Schoonheydt, Selective Oxidation of Methane by the Bis(μ-oxo)dicopper Core Stabilized on ZSM-5 and Mordenite Zeolites. *J. Am. Chem. Soc.,* (2005), **127**, 1394-1395.

11. E. M. C. Alayon, M. Nachtegaal, A. Bodi, M. Ranocchiari, J. A. van Bokhoven, Bis(μ-oxo) versus mono(μ-oxo)dicopper cores in a zeolite for converting methane to methanol: an in situ XAS and DFT investigation. *Phys. Chem. Chem. Phys.,* (2015), **17**, 7681-7693.

12. E. M. C. Alayon, M. Nachtegaal, A. Bodi, J. A. van Bokhoven, Reaction conditions of methane-to-methanol conversion affect the structure of active copper sites. *ACS Catal.,* (2014), **4**, 16-22.

13. P. Vanelderen *et al.*, Spectroscopic Definition of the Copper Active Sites in Mordenite: Selective Methane Oxidation. *J. Am. Chem. Soc.,* (2015), **137**, 6383-6392.

14. G. Brezicki, J. D. Kammert, T. B. Gunnoe, C. Paolucci, R. J. Davis, Insights into the Speciation of Cu in the Cu-H-Mordenite Catalyst for the Oxidation of Methane to Methanol. *ACS Catal.,* (2019), **9**, 5308-5319.

15. D. K. Pappas *et al.*, The Nuclearity of the Active Site for Methane to Methanol Conversion in Cu-Mordenite: A Quantitative Assessment. *J. Am. Chem. Soc.,* (2018), **140**, 15270-15278.

16. T. Ikuno *et al.*, Formation of Active Cu-oxo Clusters for Methane Oxidation in Cu-Exchanged Mordenite. *J. Phys. Chem. C,* (2019), **123**, 8759-8769.

17. S. Grundner *et al.*, Single-site trinuclear copper oxygen clusters in mordenite for selective conversion of methane to methanol. *Nat. Comm.,* (2015), **6**, 7546.

18. S. Grundner, W. Luo, M. Sanchez-Sanchez, J. A. Lercher, Synthesis of single-site copper catalysts for methane partial oxidation. *ChemComm,* (2016), **52**, 2553-2556.

19. Y. Kim, T. Y. Kim, H. Lee, J. Yi, Distinct activation of Cu-MOR for direct oxidation of methane to methanol. *ChemComm,* (2017), **53**, 4116-4119.

20. A. A. Latimer *et al.*, Understanding trends in C–H bond activation in heterogeneous catalysis. *Nat. Mater.,* (2017), **16**, 225-229.

21. B. E. R. Snyder, P. Vanelderen, R. A. Schoonheydt, B. F. Sels, E. I. Solomon, Second-Sphere Effects on Methane Hydroxylation in Cu-Zeolites. *J. Am. Chem. Soc.,* (2018), **140**, 9236-9243.

22. J. Zheng *et al.*, Importance of Methane Chemical Potential for Its Conversion to Methanol on Cu-Exchanged Mordenite. *Chem. Eur. J.,* (2020), **26**, 7563-7567.

23. B. Xu, F. Rotunno, S. Bordiga, R. Prins, J. A. van Bokhoven, Reversibility of structural collapse in zeolite Y: Alkane cracking and characterization. *J. Catal.,* (2006), **241**, 66-73.

24. J. A. van Bokhoven, A. M. J. van der Eerden, D. C. Koningsberger, Three-Coordinate Aluminum in Zeolites Observed with In situ X-ray Absorption Near-Edge Spectroscopy at the Al K-Edge: Flexibility of Aluminum Coordinations in Zeolites. *J. Am. Chem. Soc.,* (2003), **125**, 7435-7442.

25. Z. Yu *et al.*, Insights into the Dealumination of Zeolite HY Revealed by Sensitivity-Enhanced 27Al DQ-MAS NMR Spectroscopy at High Field. *Angew. Chem., Int. Ed.,* (2010), **49**, 8657-8661.

26. J. A. van Bokhoven, D. C. Koningsberger, P. Kunkeler, H. van Bekkum, A. P. M. Kentgens, Stepwise Dealumination of Zeolite Beta at Specific T-Sites Observed with 27Al MAS and 27Al MQ MAS NMR. *J. Am. Chem. Soc.,* (2000), **122**, 12842-12847.

27. G. Agostini *et al.*, In Situ XAS and XRPD Parametric Rietveld Refinement, To Understand Dealumination of Y Zeolite Catalyst. *J. Am. Chem. Soc.,* (2010), **132**, 667-678.

28. X. Yi *et al.*, Origin and Structural Characteristics of Tri-coordinated Extra-framework Aluminum Species in Dealuminated Zeolites. *J. Am. Chem. Soc.,* (2018), **140**, 10764-10774.

29. C. Liu, G. Li, E. J. M. Hensen, E. A. Pidko, Relationship between acidity and catalytic reactivity of faujasite zeolite: A periodic DFT study. *J. Catal.,* (2016), **344**, 570-577.

30. S. Schallmoser *et al.*, Impact of the local environment of Brønsted acid sites in ZSM-5 on the catalytic activity in n-pentane cracking. *J. Catal.,* (2014), **316**, 93-102.

31. J. A. van Bokhoven *et al.*, An Explanation for the Enhanced Activity for Light Alkane Conversion in Mildly Steam Dealuminated Mordenite: The Dominant Role of Adsorption. *J. Catal.,* (2001), **202**, 129-140.

32. C. Liu, G. Li, E. J. M. Hensen, E. A. Pidko, Nature and Catalytic Role of Extraframework Aluminum in Faujasite Zeolite: A Theoretical Perspective. *ACS Catal.,* (2015), **5**, 7024-7033.

33. M. Dyballa *et al.*, On How Copper Mordenite Properties Govern the Framework Stability and Activity in the Methane-to-Methanol Conversion. *ACS Catal.,* (2019), **9**, 365-375.

34. K. Hämäläinen, D. P. Siddons, J. B. Hastings, L. E. Berman, Elimination of the inner-shell lifetime broadening in x-ray-absorption spectroscopy. *Phys. Rev. Lett,* (1991), **67**, 2850-2853.

35. M. F. Qayyum *et al.*, L-Edge X-ray Absorption Spectroscopy and DFT Calculations on Cu2O2 Species: Direct Electrophilic Aromatic Attack by Side-on Peroxo Bridged Dicopper(II) Complexes. *J. Am. Chem. Soc.,* (2013), **135**, 17417-17431.

36. E. Aprà *et al.*, NWChem: Past, present, and future. *J. Chem. Phys.,* (2020), **152**, 184102.

37. B. Ravel, M. Newville, ATHENA, ARTEMIS, HEPHAESTUS: data analysis for X-ray absorption spectroscopy using IFEFFIT. *J. Synchroton Radiat.,* (2005), **12**, 537-541.

38. P. Simoncic, T. Armbruster, Peculiarity and defect structure of the natural and synthetic zeolite mordenite: A single-crystal X-ray study. *Am. Mineral.,* (2004), **89**, 421-431.

39. J. P. Perdew, K. Burke, M. Ernzerhof, Generalized Gradient Approximation Made Simple. *Phys. Rev. Lett,* (1996), **77**, 3865-3868.

40. T. D. Kühne *et al.*, CP2K: An electronic structure and molecular dynamics software package - Quickstep: Efficient and accurate electronic structure calculations. *J. Chem. Phys.,* (2020), **152**, 194103.

41. J. VandeVondele *et al.*, Quickstep: Fast and accurate density functional calculations using a mixed Gaussian and plane waves approach. *Comput. Phys. Commun.,* (2005), **167**, 103-128.

42. S. Grimme, J. Antony, S. Ehrlich, H. Krieg, A consistent and accurate ab initio parametrization of density functional dispersion correction (DFT-D) for the 94 elements H-Pu. *J. Chem. Phys.,* (2010), **132**, 154104.

43. S. Goedecker, M. Teter, J. Hutter, Separable dual-space Gaussian pseudopotentials. *Phys. Rev. B,* (1996), **54**, 1703-1710.

44. J. VandeVondele, J. Hutter, Gaussian basis sets for accurate calculations on molecular systems in gas and condensed phases. *J. Chem. Phys.,* (2007), **127**, 114105.

45. A. L. Ankudinov, B. Ravel, J. J. Rehr, S. D. Conradson, Real-space multiple-scattering calculation and interpretation of x-ray-absorption near-edge structure. *Phys. Rev. B,* (1998), **58**, 7565-7576.

46. M. Valiev *et al.*, NWChem: A comprehensive and scalable open-source solution for large scale molecular simulations. *Comput. Phys. Commun.,* (2010), **181**, 1477-1489.

47. K. Lopata, B. E. Van Kuiken, M. Khalil, N. Govind, Linear-Response and Real-Time Time-Dependent Density Functional Theory Studies of Core-Level Near-Edge X-Ray Absorption. *J. Chem. Theory Comput.,* (2012), **8**, 3284-3292.

48. G. Henkelman, A. Arnaldsson, H. Jónsson, A fast and robust algorithm for Bader decomposition of charge density. *Comp. Mater. Sci.,* (2006), **36**, 354-360.

49. Sapporo Segmented Gaussian Basis Sets. http://setani.sci.hokudai.ac.jp/sapporo.

50. B. P. Pritchard, D. Altarawy, B. Didier, T. D. Gibson, T. L. Windus, New Basis Set Exchange: An Open, Up-to-Date Resource for the Molecular Sciences Community. *J. Chem. Inf. Model.,* (2019), **59**, 4814-4820.

51. EMSL Basis Set Exchange. https://bse.pnl.gov/bse/portal. .

52. J. P. Perdew, M. Ernzerhof, K. Burke, Rationale for mixing exact exchange with density functional approximations. *J. Chem. Phys.,* (1996), **105**, 9982-9985.

53. L. Tao, I. Lee, M. Sanchez-Sanchez, Cu oxo nanoclusters for direct oxidation of methane to methanol: formation, structure and catalytic performance. *Catal. Sci. Technol.,* (2020), **10**, 7124-7141.

54. J. Dedecek, D. Kaucky, B. Wichterlova, O. Gonsiorova, Co2+ ions as probes of Al distribution in the framework of zeolites. ZSM-5 study. *Phys. Chem. Chem. Phys.,* (2002), **4**, 5406-5413.

55. J. Dědeček, Z. Sobalík, B. Wichterlová, Siting and Distribution of Framework Aluminium Atoms in Silicon-Rich Zeolites and Impact on Catalysis. *Catal Rev.,* (2012), **54**, 135-223.

56. M. A. C. Markovits, A. Jentys, M. Tromp, M. Sanchez-Sanchez, J. A. Lercher, Effect of Location and Distribution of Al Sites in ZSM-5 on the Formation of Cu-Oxo Clusters Active for Direct Conversion of Methane to Methanol. *Top. Catal.,* (2016), **59**, 1554-1563.

57. D. K. Pappas *et al.*, Methane to Methanol: Structure–Activity Relationships for Cu-CHA. *J. Am. Chem. Soc.,* (2017), **139**, 14961-14975.

58. F. Eder, M. Stockenhuber, J. A. Lercher, Brønsted Acid Site and Pore Controlled Siting of Alkane Sorption in Acidic Molecular Sieves. *J. Phys. Chem. B,* (1997), **101**, 5414-5419.

59. C. S. Triantafillidis, A. G. Vlessidis, N. P. Evmiridis, Dealuminated H−Y Zeolites: Influence of the Degree and the Type of Dealumination Method on the Structural and Acidic Characteristics of H−Y Zeolites. *Ind. Eng. Chem. Res.,* (2000), **39**, 307-319.

60. V. A. Veefkind, M. L. Smidt, J. A. Lercher, On the role of strength and location of Brønsted acid sites for ethylamine synthesis on mordenite catalysts. *Appl. Catal. A,* (2000), **194-195**, 319-332.

61. J. H. Kwak *et al.*, Effects of hydrothermal aging on NH3-SCR reaction over Cu/zeolites. *J. Catal.,* (2012), **287**, 203-209.

62. A. M. Beale, F. Gao, I. Lezcano-Gonzalez, C. H. F. Peden, J. Szanyi, Recent advances in automotive catalysis for NOx emission control by small-pore microporous materials. *Chem. Soc. Rev,* (2015), **44**, 7371-7405.

63. I. J. Drake *et al.*, An In Situ Al K-Edge XAS Investigation of the Local Environment of H+- and Cu+-Exchanged USY and ZSM-5 Zeolites. *J. Phys. Chem. B,* (2006), **110**, 11665-11676.

64. L. A. Bugaev, J. A. van Bokhoven, A. P. Sokolenko, Y. V. Latokha, L. A. Avakyan, Local Structure of Aluminum in Zeolite Mordenite as Affected by Temperature. *J. Phys. Chem. B,* (2005), **109**, 10771-10778.

65. A. Vjunov *et al.*, Tracking the Chemical Transformations at the Brønsted Acid Site upon Water-Induced Deprotonation in a Zeolite Pore. *Chem. Mater.,* (2017), **29**, 9030-9042.

66. E. M. C. Alayon, M. Nachtegaal, E. Kleymenov, J. A. van Bokhoven, Determination of the electronic and geometric structure of Cu sites during methane conversion over Cu-MOR with X-ray absorption spectroscopy. *Microporous Mesoporous mater.,* (2013), **166**, 131-136.

67. T. Günter, D. E. Doronkin, H. W. P. Carvalho, M. Casapu, J. D. Grunwaldt, HERFD-XANES and XES as complementary operando tools for monitoring the structure of Cubased zeolite catalysts during NOx-removal by ammonia SCR. *J. Phys. Conf. Ser.,* (2016), **712**, 012071.

68. E. Borfecchia *et al.*, Revisiting the nature of Cu sites in the activated Cu-SSZ-13 catalyst for SCR reaction. *Chem. Sci.,* (2015), **6**, 548-563.

69. D. K. Pappas *et al.*, Understanding and Optimizing the Performance of Cu-FER for The Direct CH4 to CH3OH Conversion. *ChemCatChem,* (2019), **11**, 621-627.

70. M. Bauer, HERFD-XAS and valence-to-core-XES: new tools to push the limits in research with hard X-rays? *Phys. Chem. Chem. Phys.,* (2014), **16**, 13827-13837.

71. S. Lafuerza *et al.*, New reflections on hard X-ray photon-in/photon-out spectroscopy. *Nanoscale,* (2020), **12**, 16270-16284.

72. D. Palagin, A. J. Knorpp, A. B. Pinar, M. Ranocchiari, J. A. van Bokhoven, Assessing the relative stability of copper oxide clusters as active sites of a CuMOR zeolite for methane to methanol conversion: size matters? *Nanoscale,* (2017), **9**, 1144-1153.

73. A. R. Kulkarni, Z.-J. Zhao, S. Siahrostami, J. K. Nørskov, F. Studt, Monocopper Active Site for Partial Methane Oxidation in Cu-Exchanged 8MR Zeolites. *ACS Catal.,* (2016), **6**, 6531-6536.

74. W. Humphrey, A. Dalke, K. Schulten, VMD: Visual molecular dynamics. *J. Mol. Graph.,* (1996), **14**, 33-38.

# 4 Role of Zeolite Topology for the Formation of Cu-Oxo Species for the Selective Oxidation of Methane to Methanol

## 4.1 Abstract

Comparison of Cu-MOR, Cu-CHA, Cu-FER and Cu-MFI shed light on the importance of 8 membered-rings (MRs) for the efficient formation of Cu-oxo clusters active for the selective oxidation of methane. The absence of 8 MR channels, as in the case of MFI lead to a decreased $Cu_{eff} = 0.19$. However, the presence of 8 MR is not the only important factor for high $Cu_{eff}$. The combination of 8 MR with 6 MR led to a similar decrease of $Cu_{eff}$. $Cu^{2+}$ species are preferably occupying BAS in 6 MR, resulting in a significant amount of inactive (monomeric) Cu-species. Therefore, both Cu-FER and Cu-CHA have an activity threshold. FT-IR analysis of the OH-region of Cu-FER confirmed the location Cu-species in 6 MR. Furthermore, it revealed the steady formation of Cu-oxo clusters in 8 and 10 MR positions. Next to inactive Cu-species, heterogeneity of Cu-oxo clusters in Cu-CHA was revealed by high-pressure studies. Comparison of methane reaction conducted at different methane pressures: at 1 bar and 40 bar, confirmed the role of $Cu^{2+}$-species in 6 MR as Cu-spectators.

## 4.2 Introduction

Cu-exchanged zeolites can selectively oxidize methane to methanol.[1-17] The range of different zeolites frameworks offers a large structural variety on the pore size, channel, and cage structure, having a significant influence on the formation of Cu-oxo clusters for the selective of methane. Among the variety of zeolite topologies, MOR has shown the ability to efficiently utilize Cu for the selective oxidation of methane.[7, 18-20] $Cu_{eff}$ of 0.33 and higher have been reported for Cu-MOR.[4, 6, 8] Formation and activity of Cu-oxo clusters active for selective oxidation of methane have been attributed to 8-MR side channels.[7, 12, 21] However, Cu-oxo cluster hosted in MFI, which consists of straight and sinusoidal 10-MR channels, show activity towards the selective oxidation of methane to methanol.[1, 2, 5] Cu-CHA shows a lower $Cu_{eff}$, despite the presence of 8 MR[7, 18-20] and Cu-FER materials, which also contains 8-MR, have been able to achieve $Cu_{eff}$ comparable to Cu-MOR[11]. The complex ensemble of channel structure and local constraints, and its effect on the formation of Cu-oxo cluster hosted in zeolites, will be subject to this chapter.

## 4.3 Experimental Methods

### *4.3.1 Preparation of Cu-zeolite samples*

H-form of FER, CHA and MOR, and MFI were obtained after calcination of the respective $NH_4$-form in synthetic air (100 mL/min) at 550 °C (10K/min) for 6 h. The $NH_4$-MOR (Si/Al = 10) sample and $NH_4$-CHA (Si/Al = 11) were purchased from Clariant. $NH_4$-FER (Si/Al = 9) was purchased from Tosoh. The $NH_4$-form of the MFI has been obtained after $NH_4$-exchange of Na-MFI (Si/Al = 14), purchased from Clariant, with $NH_4NO_3$ for 20h. The ion-exchanged sample was subsequently washed 4 times with double-ionized water and dried for 24h at 110°C.

Cu-exchanged samples were prepared by aqueous ion exchange of the respective H-form of the zeolites with $Cu^{2+}$ under controlled conditions to avoid precipitation of unwanted CuO and $Cu(OH)_2$ nanoparticles. $Cu^{2+}$-exchange was carried out at ambient temperature with 5 g zeolites in 300 mL of a 0.001-0.01 M aqueous solution of $Cu(CH_3COO)_2$ (Sigma Aldrich, 99,99%) for 20 h. The pH of the solution was kept to 5.5-6.0 during the Cu-exchange. The sample was separated from the mother liquor by centrifugation and rinsed four times with double deionized water with an intervening centrifugation step between each rinse cycle. Obtained samples were dried at 110 °C for 24 h. Si, Al, Na, and Cu contents were measured by atomic absorption spectroscopy (AAS) on a UNICAM 939 AA spectrometer after dissolution in boiling hydrofluoric acid. Cu-zeolite samples were all calcined in synthetic air at 550 °C for 2 h before IR and UV-Vis measurement.

### *4.3.2 Testing of Activity for Selective Oxidation of Methane*

The activity of the Cu-zeolite samples for the selective $CH_4$ oxidation to methanol was tested under atmospheric pressure in a stainless-steel plug flow reactor with a 4-mm inner diameter. In a typical reaction, 50 mg of Cu-zeolite (250-400 µm) was first activated for 1 h in $O_2$ at 500 °C, cooled down to 200 °C, and then flushed with He. In the next step, 90% $CH_4$ in He was flown over the sample for 4 h. The samples were then cooled to 135 °C in He and steam-assisted product desorption was performed with 50 % $H_2O$ in He. Reaction products were identified and quantified with online mass spectroscopy by monitoring the m/z signals of 31, 44, and 46 for $CH_3OH$, $CO_2$, and $(CH_3)_2O$ respectively. $(CH_3)_2O$ was considered as a condensation of two $CH_3OH$

molecules and therefore considered as two $CH_3OH$ equivalents. The sum of all detected products was considered as the total yield. High pressure reactions were performed like the conventional three stage process. The methane pressure during methane reaction was slowly increased to 40 bar with a back-pressure regulator and the reaction was kept for 4h at 200°C when the desired pressure was reached.

### *4.3.3 In Situ Ultraviolet-Visible Spectroscopy on Cu-zeolites*

Ultra-visible (UV-Vis) spectra measurements were performed in a square quartz flow reactor with a 6 mm inner diameter. The Cu-zeolites were pressed and sieved into 250-400 µm and placed in the quartz flow reactor between quartz wool. The flow reactor was then heated in a lab-made heating chamber with a hole at the bottom for the high temperature optical fiber from Avantes (FCR-7UV400 2ME-HTX). The used spectrometer was an Avaspec 2048 from Avantes with an AvaLight-DH-S-BAL (in diffuse reflectance mode) as a light source. The samples were first activated in pure $O_2$ (16mL/min) at 450 °C for 1

### 4.3.4 *In Situ IR-Spectroscopy*

The Cu-FER samples for IR spectroscopy were pressed as self-supporting wafers with a density of ca. 10 mg/cm$^2$ and activated in vacuum (1.0 x 10$^{-7}$ mbar) at 450 °C with a heating rate of 10 K/min for 1 h. The measurements were recorded on a Vertex 70 spectrometer (Bruker Optics) with a resolution of 4 cm$^{-1}$. After pretreatment, the measurements were performed at 40 °C. IR deconvolution of theOH-band region were followed after the procedure of Schallmoser et al.[29]

## 4.4 Results and Discussion

### *4.4.1 Influence of Zeolite Framework on the Activity*

A series of Cu-FER, Cu-CHA, Cu-MFI, and Cu-MOR materials with increasing Cu-loadings have been prepared by aqueous ion-exchange and tested in the three-stage process for the selective oxidation of $CH_4$ to $CH_3OH$. The results on the stoichiometric conversion of methane to methanol are sum up in Figure 1.

The term $Cu_{eff}$, "activated $CH_4$/Cu concentration, helps to the comparison of the different zeolite frameworks and Cu-loadings. In order to compare the sole influence of the different zeolite frameworks, a MOR material without Cu-Al-oxo a $Cu_{eff}$ = 0.33, without the enhancing effect of EFAl, has been chosen.

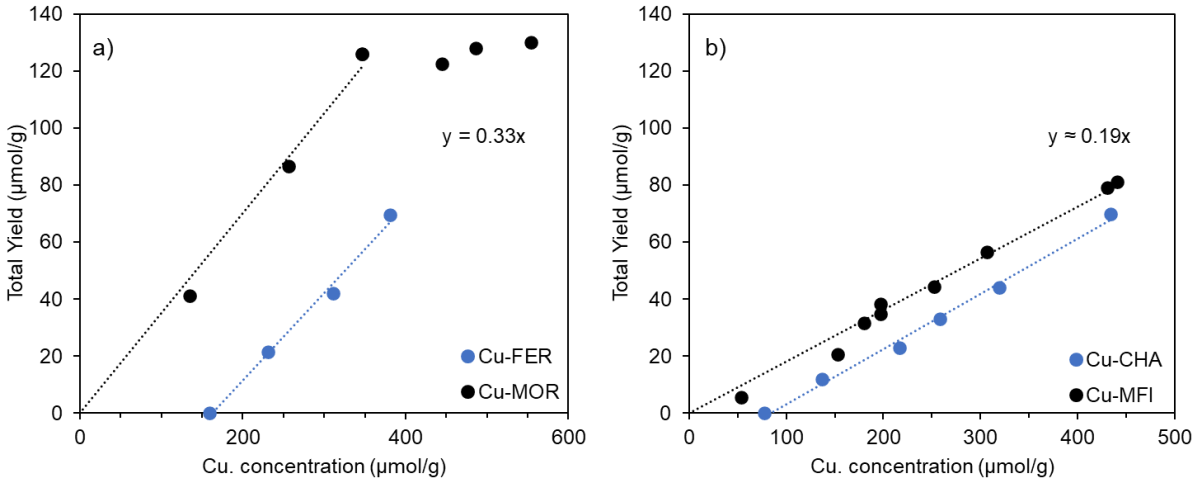


**Figure 1** Yield of $CH_4$ oxidation on the a) Cu-MOR (black) and Cu-FER (blue), and b) Cu-MFI (black) and Cu-CHA (blue) with different Cu-loadings. The numerical values of the $Cu_{eff}$ are given as y = $Cu_{eff}$x

Figure 1 shows the linear dependency of increasing Cu-loading with activity for all Cu-zeolites. As reported previously, the linear correlation, with a $Cu_{eff}$ = 0.33, for Cu-MOR indicated the homotopic formation of $[Cu_3(\mu\text{-}O)_3]^{2+}$ Cu-oxo trimer.[4] The MOR framework consists of 12 MR main channels with intersecting 8 MR side pockets with preferential locations of Cu-oxo clusters in the 8 MR side pockets.[4, 6] Although Cu-FER shares a similar channel structure with 10 MR main channels and intersecting

perpendicular 8 MR side channels,[11] they exhibit a different behavior for the selective oxidation of methane. Cu-FER shows a similar $Cu_{eff}$ = 0.33, however, it has a threshold of Cu-concentration for the formation of active Cu-oxo cluster at 159 µmol/g (Figure 1a). The $Cu_{eff}$ = 0.33 derived from Cu-FER alone would indicate that the active species consists of Cu-oxo trimer $[Cu_3(\mu\text{-}O)_3]^{2+}$. The most significant difference is the possible exchange sites at the Al-substituted T-sites.[4, 22-28] The FER structure contains Al-framework sites in the 6 MR,[29-31] where at low loadings Cu ions prefer the sterically constricted more stable, and less reactive positions.[11] Similar effects of inactive $Cu^{2+}$-species were also reported on other 6 MR containing, small pore zeolites, such as Cu-CHA.[9, 32-34]

As seen in Figure 1b), Cu-CHA has less activity compared to Cu-MOR and the $Cu_{eff}$ = 0.19 indicates the presence of Cu-spectators in the zeolite framework. The activity threshold at ca 77 µmol/g further confirms the high abundancy of inactive Cu-species. The inactive species have been attributed to $[Cu(OH]^+$ monomeric species in the 6 and 8 MR of the CHA framework.[9] Whereas the species active for the selective oxidation of methane was identified in the 8 MR as a mono(µ-oxo)dicopper $[Cu\text{-}(\mu\text{-}O)\text{-}Cu]^{2+}$ and/or $[Cu\text{-}(trans\text{-}\mu\text{-}O)_2\text{-}Cu]^{2+}$.[9, 12] Cu-MFI, with straight and sinusoidal 10 MR channel, shows no activity threshold, but a lower $Cu_{eff}$ = 0.18 that indicates the conversion of 1 methane molecule is converted per 6 Cu. Markovits et al. showed that Cu-MFI consists of active and inactive Cu-oxo trimer $[Cu_3(\mu\text{-}O)_3]^{2+}$. [5] Approximately half of the Cu-oxo clusters reside in less constrained environments, leading to a higher free energy barrier for the selective oxidation of methane.

Figure 2 shows UV-Vis spectra of Cu-MOR, Cu-FER, Cu-CHA, and Cu-MFI recorded during methane reaction at 200°C. The in situ UV-VIS measurement of Cu-MOR shows the gradual depletion of active trimeric Cu-oxo cluster $[Cu_3(\mu\text{-}O)_3]^{2+}$ throughout the methane reaction. The absorption band at approximately 29000 $cm^{-1}$ has been associated with the reaction of $[Cu_3(\mu\text{-}O)_3]^{2+}$ hosted in MOR upon $CH_4$ loading.[4] In general the bands at 20000 – 45000 $cm^{-1}$ are attributed to $Cu^{2+} \leftarrow O^{2-}$ ligand-to-metal charge transfer (LCMT) of Cu-oxo cluster.[1, 2, 12, 25, 35-37] Cu-CHA, Cu-MFI and Cu-FER show a different behavior. The band at ca 29000 $cm^{-1}$ is for the other Cu-zeolites less pronounced. However, increasing Cu-loading in Cu-FER lead to an increase of the band at 29000 $cm^{-1}$, indicating the formation of a Cu-oxo cluster similar to the $[Cu_3(\mu\text{-}O)_3]^{2+}$ cluster. Cu-MFI also shows less intense consumption at ca 29000 $cm^{-1}$. The

study from Markovits et al. showed that monomeric and dimeric Cu-oxo cluster are favored at lower low Cu concentration, whereas the trimeric species is especially formed at higher Cu concentration.[5] Cu-CHA, as we know, from the activity comparison mainly consists of mono(μ-oxo)dicopper and/or *trans*(*μ*-1,2-peroxo)dicopper. Small contributions at 29000 $cm^{-1}$ cannot be completely excluded.

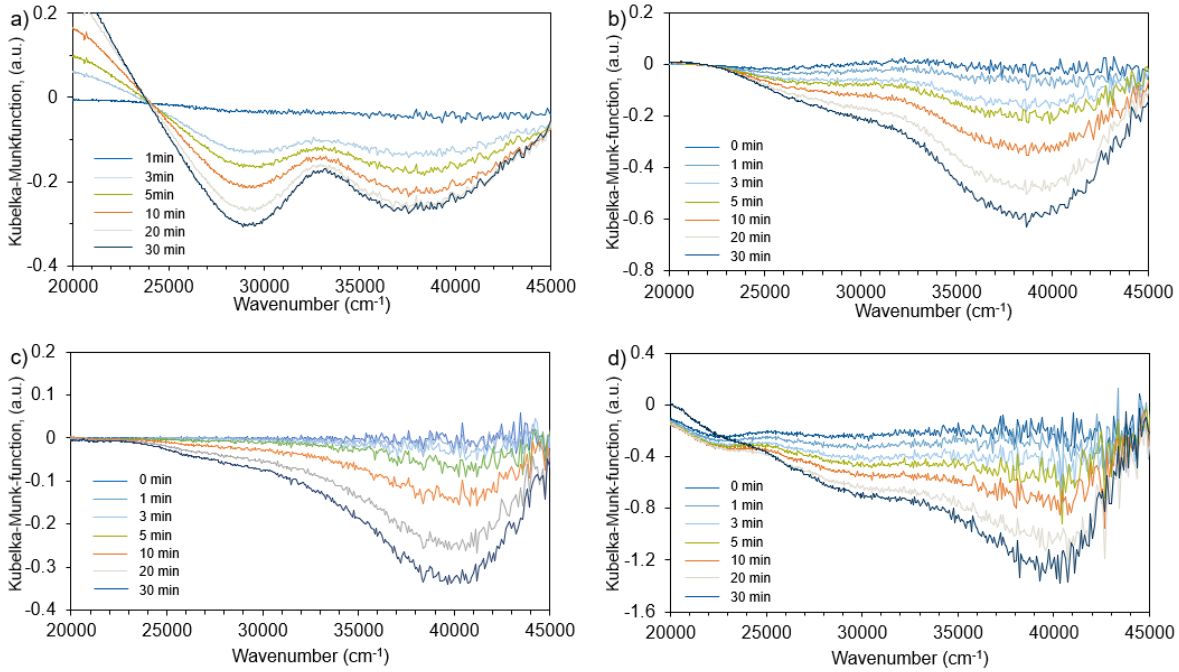


**Figure 2** Difference UV-VIS spectra of a) Cu-MOR, b) Cu-FER c) Cu-CHA and d) Cu-MFI recorded during methane reaction at 200°C after oxygen activation.

### *4.4.2 Investigation of Cu-siting in FER*

In order to shed light on the preferential location of Cu in FER, analysis of free Si-OH-Al (BAS) band at 3600 $cm^{-1}$ was performed (Figure S1). The OH-stretching at 3600 $cm^{-1}$ vibrations of FER can be further deconvoluted into OH bands into 6 MR pore (3563 $cm^{-1}$), 8 MR cage (3600 $cm^{-1}$), 8 MR pore (3587 $cm^{-1}$), and 10 MR pore (3609 $cm^{-1}$) (Figure S1, S2).[29, 30] The decrease of the corresponding OH-bands allows us to track the preferred positions of Cu in FER. For comparison, the inactive Cu-FER with 159 μmol/g and 381 μmol/g were analyzed (Table 1). The Cu-FER, 159 μmol/g, with inactive Cu-species shows indeed a preferred occupation of the BAS located in the 6 MR pore. However, also a significant fraction of Cu is located in the 10 MR, indicating

that inactive Cu species are also present in a lesser constrained environment. The further increase of Cu-loading reveals that all BAS, except BAS in the 8 MR cage, are occupied. 10 MR, 8 MR, and 6 MR OH bands are decreasing with increasing Cu-loading. Initially, inactive Cu species such as monomeric species in the 8 and 10 MR of the FER framework might gradually transform into active Cu-oxo cluster, upon Cu-addition, such as the $[Cu_3(\mu\text{-}O)_3]^{2+}$ cluster.

**Table** 1 Results from the deconvolution of OH-region at 3600 $cm^{-1}$

| Peak Position | **H-FER (norm Area)** | **Cu-FER 159 µmol/g (norm Area)** | **Cu-FER 381 µmol/g (norm Area)** |
|---|---|---|---|
| 10-MR 3609 $cm^{-1}$ | 6.9 | 5.9 | 4.5 |
| 8-MR cage 3600 $cm^{-1}$ | 4.4 | 4.2 | 4.2 |
| 8-MR pore 3587 $cm^{-1}$ | 4.4 | 4.3 | 3.3 |
| 6-MR pore 3563 $cm^{-1}$ | 3.5 | 2.4 | 1.7 |

In contrast to the $Cu_{eff}$ = 0.33, which indicates a homotopic formation of active Cu-oxo cluster, the analysis of IR deconvolution reveals a heterogeneous distribution of Cu-oxo sites in FER.

### *4.4.3 High Pressure Reaction on Cu-CHA*

Cu containing zeolites can convert methane to methanol at ambient pressures in a three-step process. Figure 3 shows the influence of increased methane pressure during the reaction. The $Cu_{eff}$ for the Cu-CHA series is increasing from 0.19 (1 bar) to 0.27 (40 bar). As mentioned in the previous chapters, Cu-CHA contains a high abundancy of Cu-spectators, which are inactive for the selective oxidation of methane.

In the case of Cu-MOR, an increase of methane pressure from 1 to 40 bar during the reaction doubled $Cu_{eff}$ from 0.3 to 0.6.[13] The active site of this Cu-MOR has been attributed as a Cu-oxo trimer $[Cu_3(\mu\text{-}O)_3]^{2+}$, [4] which can activate two methane molecules by the utilization of the second bridging oxygen of the $[Cu_3(\mu\text{-}O)_3]^{2+}$.[13] The

increase in methane chemical potential with increasing methane pressure makes the reaction of the second methane molecule favorable, which was also predicted by DFT-calculations.[13]

Ab intio thermodynamics analysis based on periodic Density Functional Theory (DFT) calculation showed that the stoichiometry of for methane activated by a $[Cu_3O_3]^{2+}$ is limited by two methane per three Cu. Kinetic analysis, assuming a two-step reaction by two bridging µ-O oxygen per $[Cu_3(\mu\text{-}O)_3]^{2+}$, shows that the activation of methane at 40 bar by the first µ-O is very fast and the second µ-O reacts slower. Enhanced $Cu_{eff}$ upon methane pressure increase has been also reported on other zeolites such as BEA, FAU, MAZ, and ERI.[14, 15, 17, 38]

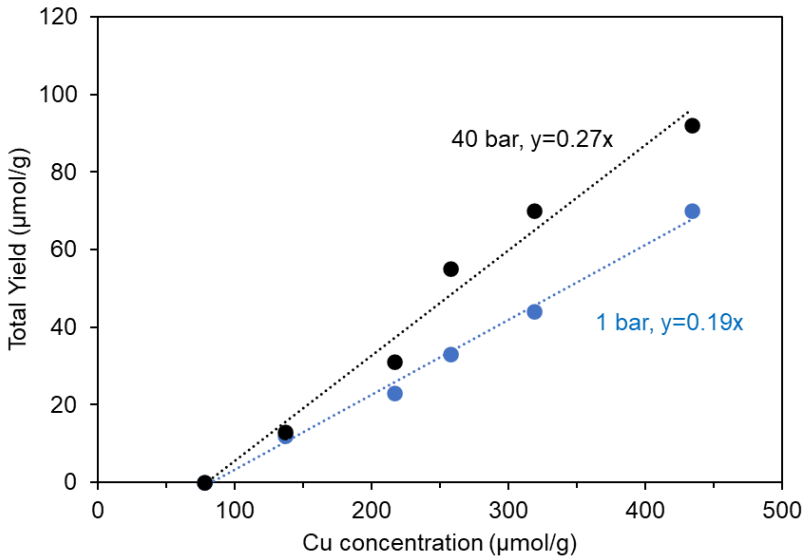


**Figure 3** Total yield of a Cu-CHA series at 1 bar (blue) and 40 bar(black). The numerical values of the $Cu_{eff}$ are given as y = $Cu_{eff}$x.

The remaining activity threshold at high pressure shows that monomeric $Cu^{2+}$ species, in 6 or 8 MR of the CHA, are not able to activate methane at elevated methane pressure. In the case of methane oxidation activity of monomeric $Cu^{2+}$-species, the threshold for elevated pressure is expected to be at a lower Cu concentration, or in other words the activity is expected to be much higher at a methane pressure of 40 bar. The linear increase from the pressure increase of 1 bar to 40 bar reveals that only a fraction of Cu-oxo species is pressure active. Otherwise, a $Cu_{eff}$ of at least 0.38 is to be expected for a homogeneous Cu-speciation. Cu-oxo cluster active for the methane

oxidation in Cu-CHA were proposed to be a mono($\mu$-oxo)dicopper and/or trans($\mu$-1,2-peroxo)dicopper present in the 8 MR,[9, 12] which should not be able to activate a second methane molecule. Therefore, the high-pressure effect indicates a heterogeneous speciation of the active Cu-oxo cluster in CHA.

## 4.5 Conclusions

Cu-MOR, Cu-CHA, Cu-MFI, and Cu-FER can convert methane to methanol. The comparison of the different frameworks showed the complex relationship of formation and activity of Cu-oxo clusters. Cu-MOR exhibits a superior $Cu_{eff}$ of 0.33. MOR with its specific 12 MR main channels and intersecting 8 MR side pockets, can provide a confined environment, where $[Cu_3(\mu\text{-}O)_3]^{2+}$ cluster active for selective methane oxidation are efficiently stabilized. The absence of 8 MR as in the case of MFI indicates that a system with only 10 MR channels is not able to support the uniform formation of active Cu-oxo clusters, hence leading to the formation of inactive Cu-species and resulting in a lower $Cu_{eff}$ = 0.2. However, 8 MR containing system such as the Cu-FER has an activity threshold up to 159 µmol/g, due to the presence of 6 MR. $Cu^{2+}$ species located in the 6 MR is very stable and inactive for the selective of methane. Furthermore, the FT-IR analysis revealed that Cu is gradually occupying BAS at 6, 8, and 10 MR of the FER framework, leading to a heterogeneous formation of active sites at different confined positions. UV-VIS analysis of Cu-FER suggests that $[Cu_3(\mu\text{-}O)_3]^{2+}$ are partially formed at higher Cu-loadings. The disadvantage of 6 MR on the efficient formation of active Cu-oxo-cluster can be further observed on CHA. Similar to FER, Cu-CHA also has an activity threshold due to the presence of Cu-spectators in the 6 MR, which are not able to activate methane at 40 bar. The high methane pressure study on Cu-CHA confirmed the heterogeneity of active Cu-oxo cluster, where $[Cu\text{-}(\mu\text{-}O)_2\text{-}Cu]^{2+}$ and $[Cu\text{-}(trans\text{-}\mu\text{-}O)_2\text{-}Cu]^{2+}$ might coexist together with $[Cu_3(\mu\text{-}O)_3]^{2+}$ cluster.

## 4.6 Acknowledgement

The financial support from the Deutsche Forschungsgemeinschaft (DFG, Project number 326562156) and the TUM International Graduate School of Science and Engineering (IGSSE) is acknowledged. The author thanks Lei Tao, Takaaki Ikuno and Matteo Ranieri for the support in the experiments.

## 4.7 Appendix

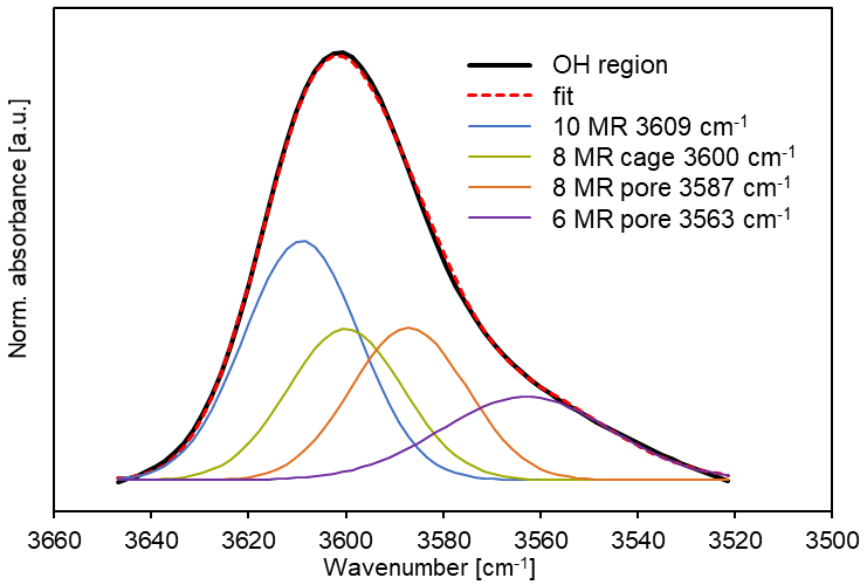


**Figure S1** a) Deconvolution of OH stretching vibration region for H-FER with OH bands at 3609 $cm^{-1}$ (10 MR, blue), 3600 $cm^{-1}$ (8 MR cage, green), 3587 $cm^{-1}$ (8 MR pore, orange), and 3563 $cm^{-1}$ (6 MR, purple). The sample was pretreated in vacuum at 450 °C for 1h.

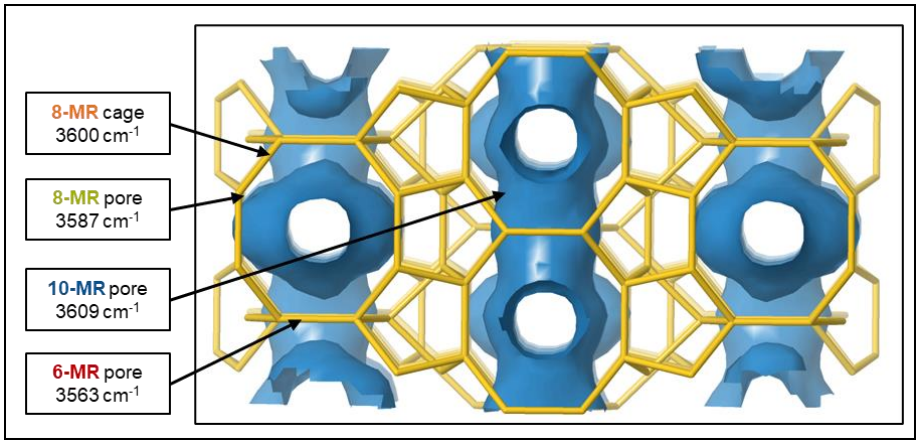


**Figure S2** Location of OH (acid sites) within the FER framework (Drawing taken from Database of Zeolite Structures, Ch. Baerlocher and L.B. McCusker: http://www.iza-structure.org/databases/).

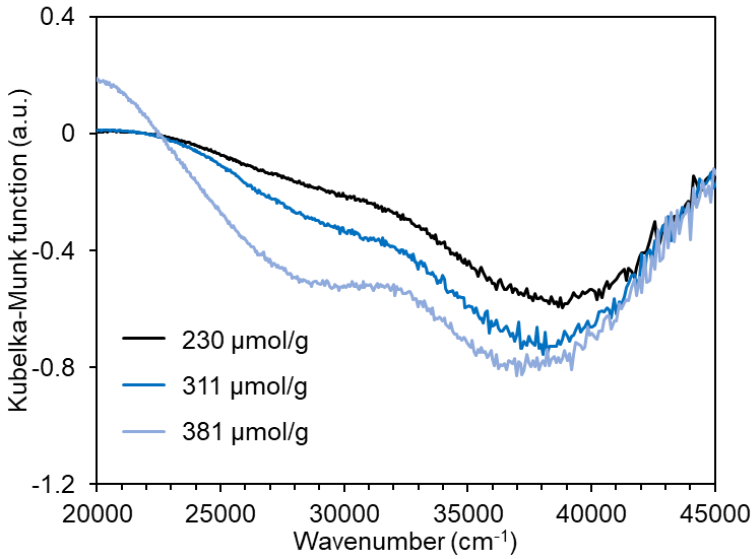


**Figure S3** Difference UV-VIS difference spectra of Cu-FER with 230, 311, and 381 µmol/g. The spectra plotted are from the measurement at 30 min methane reaction at 200°C.

## 4.8 References


1. M. H. Groothaert, J. A. van Bokhoven, A. A. Battiston, B. M. Weckhuysen, R. A. Schoonheydt, Bis(μ-oxo)dicopper in Cu-ZSM-5 and Its Role in the Decomposition of NO: A Combined in Situ XAFS, UV−Vis−Near-IR, and Kinetic Study. *J. Am. Chem. Soc.,* (2003), **125**, 7629-7640.

2. M. H. Groothaert, P. J. Smeets, B. F. Sels, P. A. Jacobs, R. A. Schoonheydt, Selective Oxidation of Methane by the Bis(μ-oxo)dicopper Core Stabilized on ZSM-5 and Mordenite Zeolites. *J. Am. Chem. Soc.,* (2005), **127**, 1394-1395.

3. E. M. Alayon, M. Nachtegaal, M. Ranocchiari, J. A. van Bokhoven, Catalytic conversion of methane to methanol over Cu–mordenite. *ChemComm,* (2012), **48**, 404-406.

4. S. Grundner *et al.*, Single-site trinuclear copper oxygen clusters in mordenite for selective conversion of methane to methanol. *Nat. Comm.,* (2015), **6**, 7546.

5. M. A. C. Markovits, A. Jentys, M. Tromp, M. Sanchez-Sanchez, J. A. Lercher, Effect of Location and Distribution of Al Sites in ZSM-5 on the Formation of Cu-Oxo Clusters Active for Direct Conversion of Methane to Methanol. *Top. Catal.,* (2016), **59**, 1554-1563.

6. I. Lee *et al.*, Activity of Cu–Al–Oxo Extra-Framework Clusters for Selective Methane Oxidation on Cu-Exchanged Zeolites. *JACS Au,* (2021), **1**, 1412-1421.

7. M. B. Park, S. H. Ahn, A. Mansouri, M. Ranocchiari, J. A. van Bokhoven, Comparative Study of Diverse Copper Zeolites for the Conversion of Methane into Methanol. *ChemCatChem,* (2017), **9**, 3705-3713.

8. G. Brezicki, J. D. Kammert, T. B. Gunnoe, C. Paolucci, R. J. Davis, Insights into the Speciation of Cu in the Cu-H-Mordenite Catalyst for the Oxidation of Methane to Methanol. *ACS Catal.,* (2019), **9**, 5308-5319.

9. D. K. Pappas *et al.*, Methane to Methanol: Structure–Activity Relationships for Cu-CHA. *J. Am. Chem. Soc.,* (2017), **139**, 14961-14975.

10. D. K. Pappas *et al.*, The Nuclearity of the Active Site for Methane to Methanol Conversion in Cu-Mordenite: A Quantitative Assessment. *J. Am. Chem. Soc.,* (2018), **140**, 15270-15278.

11. D. K. Pappas *et al.*, Understanding and Optimizing the Performance of Cu-FER for The Direct CH4 to CH3OH Conversion. *ChemCatChem,* (2019), **11**, 621-627.

12. B. Ipek *et al.*, Formation of [Cu2O2]2+ and [Cu2O]2+ toward C–H Bond Activation in Cu-SSZ-13 and Cu-SSZ-39. *ACS Catal.,* (2017), **7**, 4291-4303.

13. J. Zheng *et al.*, Importance of Methane Chemical Potential for Its Conversion to Methanol on Cu-Exchanged Mordenite. *Chem. Eur. J.,* (2020), **26**, 7563-7567.

14. A. J. Knorpp *et al.*, Comparative performance of Cu-zeolites in the isothermal conversion of methane to methanol. *ChemComm,* (2019), **55**, 11794-11797.

15. A. J. Knorpp, A. B. Pinar, M. A. Newton, V. L. Sushkevich, J. A. van Bokhoven, Copper-Exchanged Omega (MAZ) Zeolite: Copper-concentration Dependent Active Sites and its Unprecedented Methane to Methanol Conversion. *ChemCatChem,* (2018), **10**, 5593-5596.

16. A. J. Knorpp *et al.*, Paired Copper Monomers in Zeolite Omega: The Active Site for Methane-to-Methanol Conversion. *Angew. Chem., Int. Ed.,* (2021), **60**, 5854-5858.

17. V. L. Sushkevich, J. A. van Bokhoven, Methane-to-Methanol: Activity Descriptors in Copper-Exchanged Zeolites for the Rational Design of Materials. *ACS Catal.,* (2019), **9**, 6293-6304.

18. M. A. Newton, A. J. Knorpp, V. L. Sushkevich, D. Palagin, J. A. van Bokhoven, Active sites and mechanisms in the direct conversion of methane to methanol using Cu in zeolitic hosts: a critical examination. *Chem. Soc. Rev,* (2020), **49**, 1449-1486.

19. Y. Ma *et al.*, Low-Temperature Solid-State Ion-Exchange Method for Preparing Cu-SSZ-13 Selective Catalytic Reduction Catalyst. *ACS Catal.,* (2019), **9**, 6962-6973.

20. L. Tao, I. Lee, M. Sanchez-Sanchez, Cu oxo nanoclusters for direct oxidation of methane to methanol: formation, structure and catalytic performance. *Catal. Sci. Technol.,* (2020), **10**, 7124-7141.

21. Z.-J. Zhao, A. Kulkarni, L. Vilella, J. K. Nørskov, F. Studt, Theoretical Insights into the Selective Oxidation of Methane to Methanol in Copper-Exchanged Mordenite. *ACS Catal.,* (2016), **6**, 3760-3766.

22. J. Dědeček, B. Wichterlová, Role of Hydrated Cu Ion Complexes and Aluminum Distribution in the Framework on the Cu Ion Siting in ZSM-5. *J. Phys. Chem. B,* (1997), **101**, 10233-10240.

23. J. Dedecek, D. Kaucky, B. Wichterlova, O. Gonsiorova, Co2+ ions as probes of Al distribution in the framework of zeolites. ZSM-5 study. *Phys. Chem. Chem. Phys.,* (2002), **4**, 5406-5413.

24. C. W. Andersen *et al.*, Redox-Driven Migration of Copper Ions in the Cu-CHA Zeolite as Shown by the In Situ PXRD/XANES Technique. *Angew. Chem., Int. Ed.,* (2017), **56**, 10367-10372.

25. T. Ikuno *et al.*, Formation of Active Cu-oxo Clusters for Methane Oxidation in Cu-Exchanged Mordenite. *J. Phys. Chem. C,* (2019), **123**, 8759-8769.

26. S. Grundner, W. Luo, M. Sanchez-Sanchez, J. A. Lercher, Synthesis of single-site copper catalysts for methane partial oxidation. *ChemComm,* (2016), **52**, 2553-2556.

27. J. H. Kwak *et al.*, Following the movement of Cu ions in a SSZ-13 zeolite during dehydration, reduction and adsorption: A combined in situ TP-XRD, XANES/DRIFTS study. *J. Catal.,* (2014), **314**, 83-93.

28. M. P. Attfield, S. J. Weigel, A. K. Cheetham, On the Nature of Nonframework Cations in a Zeolitic deNOxCatalyst. *J. Catal.,* (1997), **172**, 274-280.

29. S. Schallmoser *et al.*, Impact of the local environment of Brønsted acid sites in ZSM-5 on the catalytic activity in n-pentane cracking. *J. Catal.,* (2014), **316**, 93-102.

30. V. L. Zholobenko, D. B. Lukyanov, J. Dwyer, W. J. Smith, Ferrierite and SUZ-4 Zeolite: Characterization of Acid Sites. *J. Phys. Chem. B,* (1998), **102**, 2715-2721.

31. I. R. Subbotina, B. N. Shelimov, V. B. Kazanskii, IR Spectroscopic Study of Alkane Interaction with the Brønsted Acid Sites of Hydrogen-Exchanged Zeolites. *Kinet. Catal.,* (2002), **43**, 412-418.

32. J. Hun Kwak, H. Zhu, J. H. Lee, C. H. F. Peden, J. Szanyi, Two different cationic positions in Cu-SSZ-13? *ChemComm,* (2012), **48**, 4758-4760.

33. E. Borfecchia *et al.*, Evolution of active sites during selective oxidation of methane to methanol over Cu-CHA and Cu-MOR zeolites as monitored by operando XAS. *Catal. Today,* (2019), **333**, 17-27.

34. A. R. Kulkarni, Z.-J. Zhao, S. Siahrostami, J. K. Nørskov, F. Studt, Monocopper Active Site for Partial Methane Oxidation in Cu-Exchanged 8MR Zeolites. *ACS Catal.,* (2016), **6**, 6531-6536.

35. Y. Kim, T. Y. Kim, H. Lee, J. Yi, Distinct activation of Cu-MOR for direct oxidation of methane to methanol. *ChemComm,* (2017), **53**, 4116-4119.

36. P. Vanelderen *et al.*, Spectroscopic Definition of the Copper Active Sites in Mordenite: Selective Methane Oxidation. *J. Am. Chem. Soc.,* (2015), **137**, 6383-6392.

37. F. Giordanino *et al.*, Characterization of Cu-exchanged SSZ-13: a comparative FTIR, UV-Vis, and EPR study with Cu-ZSM-5 and Cu-β with similar Si/Al and Cu/Al ratios. *Dalton Trans.,* (2013), **42**, 12741-12761.

38. J. Zhu *et al.*, Cu-Erionite Zeolite Achieves High Yield in Direct Oxidation of Methane to Methanol by Isothermal Chemical Looping. *Chem. Mater.,* (2020), **32**, 1448-1453.

# 5 Conclusion

Cu-oxo cluster in MOR active for the selective oxidation of methane to methanol was studied in this thesis. The identification of oxidation states of Cu-species in Zeolites plays an important role for the understanding of redox behavior of active species and sheds light on the nuclearity and reactivity of Cu-oxo cluster. Evaluation of oxidation states after autoreduction and oxidative treatment of Cu-MOR were possible by the utilization of IR-spectroscopy in combination with CO and NO probe molecules.

CO molecules selectively interact with $Cu^{+}$ species and do not allow the screening of residual $Cu^{2+}$ species after autoreduction, whereas NO molecules allow the simultaneous identification of $Cu^{+}$ and $Cu^{2+}$ species present in MOR. However, critical comparison to existing literature shows the limitation on the interpretation of this technique. Attribution of $Cu^{2+}$-NO bands are still under debate. Recently reported results on monomeric and “oligomeric” or clusters with Cu nuclearity > 1 are contradicting as most of the investigated Cu-zeolites are not prepared by pH controlled aqueous ion exchange, over-exchanged or partially autoreduced through different activation procedures. This hampers the direct comparison of Cu-zeolites investigated by NO FT-IR and other techniques.

A popular tool for the elucidation of redox behavior Cu-oxo cluster is the utilization of XAS. However, Cu-oxo species or in general $Cu^{2+}$-species are prone to X-ray induced radiation damage. Results show that $Cu^{2+}$ readily reduces under beam exposure and radiation damage governs the regimes of oxygen activation, autoreduction, and $CH_4$ reaction, leading to misinterpretation of kinetic behavior and structure of Cu-oxo cluster. In general, great care must be taken for the investigation of sensitive Cu-species present in zeolites through XAS.

The activity of a highly active Cu-MOR series has been attributed to an interaction of Cu-oxo species with extra lattice Al in the 8-MR side pockets of MOR. It is known, that active Cu-oxo species such as the $[Cu_3(\mu\text{-}O)_3]^{2+}$ are preferentially located in the constrains of the 8 MR side pockets. The location of EFAl species has been achieved using IR spectroscopy with *n*-hexane and pyridine. Actual interaction of EFAl and $Cu^{2+}$-species were finally observed by Al K-edge XAS. Utilization of experimental Cu K and L-edge XAFS spectra in combination with TDDFT and MD-EXAFS calculation

identified the structure as a $[Cu_2AlO_3]^{2+}$ cluster, which can activate two methane molecules under ambient pressure. This novel approach helps to overcome the limitations of conventional XANES and EXAFS analysis, and further enables the identification of the active site of active incorporated in a heterogeneous environment.

Comparison of different Cu-zeolites showed that Cu-oxo species are sensitive to the sterical constraints of zeolites. The observed activity threshold for Cu-FER and Cu-CHA series indicates a relatively high fraction of inactive Cu-species, which are preferentially located in the 6 MR. However, deconvolution of the BAS region of Cu-FER shows a gradual consumption of BAS located in 6, 8, and 10 MR. $Cu_{eff}$ of 0.33 indicates a homotopic formation of active sites at higher loading. It is hypothesized that initially inactive species in the 8 and 10 MR form active Cu-oxo cluster upon the increase of Cu concentration. Cu-CHA and Cu-MFI have a similar $Cu_{eff}$ of 0.2. The reason for the lower activity of Cu-MFI is known to come from inactive $[Cu_3(\mu\text{-}O)_3]^{2+}$ clusters. However, Cu-CHA has a heterogeneous distribution of Cu-spectators and active Cu-oxo sites. The evaluation of different Cu-zeolites reveals that 8 MR and 10 MR are crucial for the efficient formation of active Cu-oxo species. The presence of 6 MR in zeolite results in the formation of inactive Cu-species and lead to activity thresholds, which can be overcome at higher Cu concentrations.

# List of Publications

### Research articles published in peer-reviewed journals as first author

I. Lee, M. Lee, L. Tao, T. Ikuno, R. Khare, A. Jentys T. Huthwelker, C. N. Borca, A. Kalinko, O. Y. Gutierrez, N. Govind, J. L. Fulton, J. Z. Hu, V. Glezakou, R. Rousseau, M. Sanchez-Sanchez, J. A. Lercher, Activity of Cu-Al-oxo extra-framework clusters for selective methane oxidation on Cu exchanged zeolites. *JACS Au* (**2021**), *1*, 9, 1412-1421.

### Research articles published in peer-reviewed journals as co-author

L. Tao, I. Lee, M. Sanchez-Sanchez, Cu oxo nanoclusters for direct oxidation of methane to methanol: formation, structure and catalytic performance, *Catal. Sci. Technol.* (2020), 7124-7141.

J. Zheng, I. Lee, E. Khramenkova, M. Wang, B. Peng. O. Y. Gutierrez, J. L. Fulton, D. M. Camaioni, R. Khare, A. Jentys, G. L. Haller, E. A. Pidko, M. Sanchez-Sanchez, J. A. Lercher, Importance of Methane Chemical Potential for Its Conversion to Methanol on Cu-Exchanged Mordenite, *Chem. Eur. J.* (2020), 7563-7567.

M. Peroni, I. Lee, X. Huang, E. Baráth, O. Y. Gutiérrez, J. A. Lercher, Deoxygenation of Palmitic Acid on Unsupported Transition-Metal Phosphides, *ACS Catal.* (2017), 6331-6341.

**Conference contributions**

I. Lee, L. Tao. T. Ikuno, M. Sanchez-Sanchez, J. A. Lercher, Role of zeolite framework on the efficient formation of Cu-oxo active sites for direct methane oxidation, *14th European Congress on Catalysis - EuropaCat*, (**2019**), Aachen. (Oral presentation)

I. Lee, T. Ikuno, L. Tao, M. Sanchez-Sanchez, J. A. Lercher, Selective and efficient formation of Cu-oxo sites for methane oxidation to methanol in different zeolite frameworks, *Jahrestreffen deutscher Katalytiker* (**2019**), Weimar. (Poster)

M. Peroni, I. Lee, O. Y. Gutiérrez, J. A. Lercher, Hydrocracking of Paraffins on Transition Metal Phosphide Catalysts, *Catalysis – Novel Aspects in Petrochemistry and Refining*, DGMK Conference (**2016**), Berlin. (Poster)

M. Peroni, X. Huang, I. Lee, E. Baráth, O. Y. Gutiérrez, J. A. Lercher, Metal phosphide catalysts for the conversion of microalgae oil to biofuel, *3rd International Symposium on Catalysis for Clean Energy and Sustainable Chemistry* (**2016**), Madrid. (Poster)

M. Peroni, X. Huang, I. Lee, E. Baráth, O. Y. Gutierrez, J. A. Lercher, Towards efficient hydrodexygenation on transition metal phosphides, *Jahrestreffen deutscher Katalytiker* (**2015**), Weimar. (Poster)

M. Peroni, X. Huang, I. Lee, E. Baráth, O. Y. Gutierrez, J. A. Lercher, Towards efficient hydrodeoxygenation on transition metal phosphides, *12th European Congress on Catalysis - EuropaCat* (**2015**), Kazan. (Oral presentation)

M. Peroni, X. Huang, I. Lee, E. Baráth, O. Y. Gutierrez, J. A. Lercher, Hydrodeoxygenation on transition metal phosphides, *24th North American Catalysis Society* (**2015**), Pittsburgh. (Oral presentation)